UNIVERSITÀ DEGLI STUDI DI TRIESTE

Università degli Studi di Trieste
e
The *Abdus Salam* International Centre for Theoretical Physics

Dottorato di Ricerca in
ENVIRONMENTAL AND INDUSTRIAL FLUID MECHANICS

Curriculum: Fluidodinamica (SSD ING-IND/06)

Numerical Simulations of Thermal Convection at High Prandtl Numbers

Gabriella Silano

Supervisore:
Prof. Roberto Verzicco

Relatore:
Prof. Katepalli R. Sreenivasan

Coordinatore:
Prof. Vincenzo Armenio

ANNO ACCADEMICO 2007/2008

Abstract

In this thesis we present the results of an extensive campaign of direct numerical simulations of Rayleigh-Bénard convection at high Prandtl numbers ($10^{-1} \leq Pr \leq 10^4$) and moderate Rayleigh numbers ($10^5 \leq Pr \leq 10^9$). The computational domain is a cylindrical cell of aspect-ratio (diameter over cell height) $\Gamma = 1/2$, with the no-slip condition imposed to the boundaries.

By scaling the results, we find a $1/\sqrt{Pr}$ correction to apply to the free-fall velocity, obtaining a more appropriate representation of the large scale velocity at high Pr. We investigate the Nusselt and the Reynolds number dependence on Ra and Pr, comparing the results to previous numerical and experimental work. At high Pr the scaling behavior of the Nusselt number with respect to Ra is generally consistent with the power-law exponent 0.309. The Nusselt number is independent of Pr, even at the highest Ra simulated. The Reynolds number scales as $Re \sim \sqrt{Ra}/Pr$, neglecting logarithmic corrections. We analyze the global and local features of viscous and thermal boundary layers and their scaling behavior with respect to Rayleigh and Prandtl numbers, and with respect to Reynolds and Peclet numbers. We find that the flow approaches a saturation regime when Reynolds number decreases below the critical value $Re_s \simeq 40$. The thermal boundary layer thickness turns out to increase slightly even when the Peclet number increases. We explain this behavior as a combined effect of the Peclet number and the viscous boundary layer influences.

The range of Ra and Pr simulated contains steady, periodic and turbulent solutions. A rough estimate of the transition from steady to unsteady flow is obtained by monitoring the time-evolution of the system until it reaches stationary solutions ($Ra_U \simeq 7.5 \times 10^6$ at $Pr = 10^3$). We find multiple solutions as long-term phenomena at $Ra = 10^8$ and $Pr = 10^3$ which, however, do not result in significantly different Nusselt number. One of these multiple solutions, even if stable for a long time interval, shows a break in the mid-plane symmetry of the temperature profile. The result is similar to that of some non-Boussinesq effects. We analyze the flow structures through the transitional phases by direct visualizations of the temperature and velocity fields. We also describe how the behavior of the flow structures changes for increasing Pr. A wide variety of large-scale circulations and plumes structures are found. The single-roll circulation is characteristic only of the steady and periodic solutions. For other solutions, at lower Pr, the mean flow generally consists of two opposite toroidal structures; at higher Pr, the flow is organized in multi-cell structures extending mostly in the vertical direction. At high Pr, plumes detach from sheet-like structures. The different large-scale-structure signatures are generally reflected in the data trends with re-

spect to Ra, but not in those with respect to Pr. In particular, the Nusselt number is independent of Pr, even when the flow structures appear strongly different varying Pr.

In order to assess the reliability of the data-set we perform a systematic analysis of the error affecting the data. Refinement grid analysis is extensively applied.

In questa tesi presentiamo i risultati di un'estensiva campagna di simulazioni numeriche dirette della convezione di Rayleigh-Bénard ad alti numeri di Prandtl ($10^{-1} \leq Pr \leq 10^4$) e moderati numeri di Rayleigh ($10^5 \leq Pr \leq 10^9$). Il dominio computazionale è una cella cilindrica di allungamento (diametro su altezza cella) $\Gamma = 1/2$, con condizioni di non-slittamento ai contorni.

Scalando i risultati, troviamo una correzione di $1/\sqrt{Pr}$ da applicare alla velocità di caduta libera, ottenendo una rappresentazione più appropriata della velocità di larga scala ad elevati Pr. Investighiamo la dipendenza del numero di Nusselt e del numero di Reynolds da Ra e Pr, comparando i risultati con precedenti lavori numerici e sperimentali. Ad elevati Pr il comportamento di scala del numero di Nusselt rispetto a Ra è generalmente compatibile con l'esponente di legge di potenza 0.309. Il numero di Nusselt è indipendente da Pr, anche per il più alto Ra simulato. Il numero di Reynolds scala come $Re \sim \sqrt{Ra}/Pr$, a meno di correzioni logaritmiche. Analizziamo le caratteristiche locali e globali degli strati limite viscosi e termici, ed il loro comportamento di scala rispetto ai numeri Rayleigh e Prandtl, e rispetto ai numeri Reynolds e Peclet. Troviamo che il flusso approccia un regime di saturazione quando il numero di Reynolds scende sotto il valore critico $Re_s \simeq 40$. Lo spessore dello strato limite termico comincia a crescere leggermente anche quando in numero di Peclet aumenta. Spieghiamo questo comportamento come un effetto combinato delle influenze del numero di Peclet e dello strato limite viscoso.

L'intervallo di Ra e Pr simulato contiene soluzioni stazionarie, periodiche e turbolente. Una stima approssimata della transizione da flusso stazionario a non stazionario è ottenuta monitorando l'evoluzione temporale del sistema fino al raggiungimento di soluzioni stazionarie o statisticamente stazionarie ($Ra_U \simeq 7.5 \times 10^6$ a $Pr = 10^3$). Troviamo soluzioni multiple come fenomeni di lungo termine a $Ra = 10^8$ e $Pr = 10^3$ che, comunque, non comportano differenze significative nel numero di Nusselt. Una di queste soluzioni multiple, anche se stabile per un lungo intervallo di tempo, mostra una rottura della simmetria del profilo di temperatura rispetto al piano mediano. Il risultato è simile a quello di alcuni effetti di non-Boussinesq. Analizziamo le strutture del flusso nelle fasi di transizione tramite visualizzazioni dirette dei campi di velocità e temperatura. Descriviamo inoltre come il

comportamento delle strutture del flusso cambia al crescere di Pr. Un'ampia varietà di circolazioni di larga scala e strutture a pennacchio vengono trovate. La circolazione a singolo anello è caratteristica solo delle soluzioni stazionarie e periodiche. Per le altre soluzioni, a Pr più bassi, il flusso medio è generalmente composto da due strutture toroidali opposte; a Pr più alti, il flusso è organizzato in strutture multi-cellulari che si estendono maggiormente in direzione verticale. Ad alti Pr, pennacchi si staccano da strutture simili a fogli. Le impronte delle differenti strutture di larga scala si riflettono generalmente nell'andamento dei dati rispetto a Ra, ma non rispetto a Pr. In particolare, il numero di Nusselt è indipendente da Pr, anche quando le strutture del flusso appaiono molto differenti al variare di Pr.

Per stabilire l'affidabilità dell'insieme dei dati, effettuiamo un'analisi sistematica degli errori a cui i dati sono soggetti. L'analisi di raffinamento della griglia è largamente applicata.

Contents

1 Introduction **1**

1.1 Introduction 1

2 Physical and numerical setup **7**

2.1 Introduction 7

2.2 Governing equations 8

2.3 Numerical code 10

2.4 Grid resolution criteria 16

2.4.1 *Apriori* estimate of the grid size 16

2.4.2 Maximum and minimum typical time estimates 20

2.4.3 General information on simulations 22

2.4.4 *Aposteriori* grid sizing checks 25

3 Error analysis **31**

3.1 Introduction 31

3.2 Error checks and error bars 32

3.3 Grid refinement analysis 37

3.4 Long time errors and multiple flow structures 40

4 The non-dimensional form for large Pr **45**

4.1 Introduction 45

4.2 Non-dimensional form of equations 46

4.3 Characteristic velocity 49

4.4 Reynolds and Peclet numbers 55

5 Transitional phases and flow structures **59**

5.1 Introduction 59

5.2 A qualitative picture of transitions 60

5.3 Large scale structures 68

5.3.1 Large scale structures at increasing Pr 69

6 Nusselt number **75**

6.1 Introduction 75

6.2 Nusselt number versus Ra and Pr 77

7 Boundary layers and vertical profiles **81**

7.1 Introduction 81

7.2 Local versus global features of vertical profiles 82

7.3 Vertical profiles and boundary layers as functions of Ra and Pr 89

7.3.1 Global profiles 90

7.3.2 Boundary layer thicknesses 94

8 Conclusions **101**

A Numerical instabilities **105**

Chapter 1

Introduction

1.1 Introduction

The thermal convection is the most efficient mechanism of heat transfer in a fluid material subjected to a temperature difference. It is different from conduction, in which the heat transfer is due to a pure diffusion, and involves (in addition) a fluid motion, which implies macroscopic heat transport. The modalities of this transport are mainly influenced by flow regime (laminar or turbulent) and by flow circulations (if they exist).

Due its high efficiency, the convective heat transfer is a preferred mechanism in practical applications and in natural phenomena. In particular, it occurs in a wide variety of problems in applied physics, ranging from stellar activities in astrophysics to natural convection in atmospheric physics and Earth's mantle convection in geophysics ([16], [31]).

In spite of the great complexity of materials and geometries in practical examples, the essential features of thermal convection problems can be captured by a very idealized model: confined flow between infinitely-conducting parallel plates heated from below and cooled from above. In this fluid layer, thermal expansion produces an unstable density gradient which, if strong enough, generates a flow referred to as thermal convection or Rayleigh-Bénard convection ([8],[57]). As the temperature difference is increased the flow progressively evolves from a steady to an unsteady regime and eventually to turbulence.

The paradigm of thermal convection is generally based on the Boussinesq approximation, in which the fluid properties are assumed to be constant despite the temperature gradient across the fluid depth, and the only effect of the temperature in the momentum equation is to modify the buoyancy term [74].

Even if the Rayleigh-Bénard model is apparently quite simple, it contains complex and poorly understood dynamics. When a heated blob of fluid (being less dense) feels the buoyancy force, it tends to rise. Cooler fluid falls into its place (the vice-versa in case of cold fluid blob). This mechanism of rising-and-falling fluid generate large scale circulations of a typical size comparable to the depth of the fluid layer. In the Earth's mantle for example these circulations cause tectonic motions of the ground [55]. Even when the flow is turbulent, highly structured patterns are generally present.

One coherent structure often found in thermal convection is a plume. The plumes are mushroom-shaped objects detaching from bottom and top plates, which generally tend to cluster, forming uprising hot jets and downward cold jets. In a very viscous fluid they seem to drive a large scale circulation. In a less viscous fluid they seem to be driven by a large circulation. Close to the plates the large scale circulations form thin viscous and thermal boundary layers (the boundary layers may be formed even in the absence of large scale circulation, owing to a long term effect of instantaneous large eddies). The majority of the temperature drop between the top and bottom plates occurs within the thermal boundary layers. In practice, this *"nonequilibrium system can organize itself in an amazing fashion, leading to a sort of machine with many different parts, each serving an apparent function"* [38].

The efficiency of this machine is measured by the ratio between the actual heat transport and the conductive heat transport obtained in absence of motion. This measure is represented by the Nusselt number (Nu). A correct prediction of the strength of Nu as a response to a given forcing (applied temperature difference) is one of the main aims of thermal convection studies. The solution of this problem implies a knowledge of each single part of the system: large scale circulations and plume structures, viscous and thermal boundary layers, and on apparently irregular turbulent motion. These parts interact to each other in a non-linear way and, moreover, they can change their features in the presence of a different forcing or a different working fluid. This makes the problem extremely complex.

In the Rayleigh-Bénard model the forcing and the working fluid are represented by two non-dimensional parameters: the Rayleigh number (Ra), representing a non-dimensional measure of the temperature difference applied to the fluid layer, and the Prandtl number (Pr), the ratio between kinematic viscosity and thermal diffusivity of the fluid. These parameters mainly govern the dynamics of the system. In presence of laterally confined fluid layer, another important parameter can be the aspect ratio (Γ), which represents the ratio between the maximum horizontal extension of the system and its depth. Sometimes,

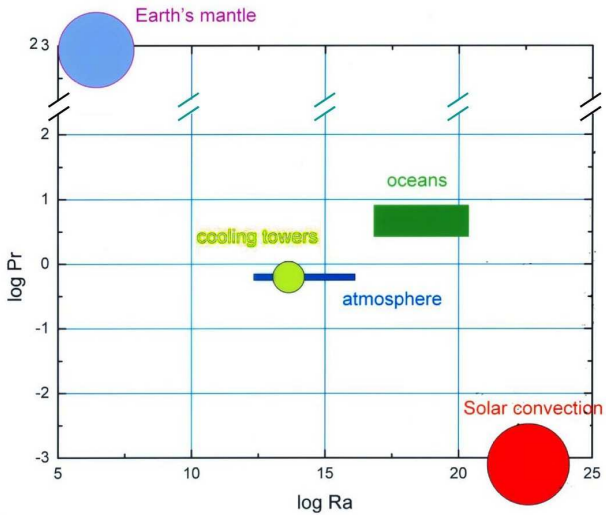

Figure 1.1: Typical Ra and Pr ranges characterizing real problems.

especially for low values of Ra, details such as the geometry of the flow apparatus also seem to matter.

The Rayleigh number characterizes the strength of the thermal destabilizing forcing with respect to a viscous stabilizing effect. It is worth mentioning that the Rayleigh number is proportional to the third power of the fluid layer thickness across which the temperature difference is established. Therefore the real problems are generally characterized by very high values of Ra (see fig. 1.1). Accordingly, experiments and numerical simulations are aimed at reaching the highest Ra values. This has been achieved at Prandtl numbers in the range $0.7 \leq Pr \leq 8$, typical of gaseous fluids or the most common liquids. In particular, using a very effective experimental technique to obtain an extensive range of Ra, the highest value reached in controlled environment was $Ra = 10^{17}$ [50]. This technique exploits the properties of cryogenic helium gas close to the critical point [73]. Instead, the highest value obtained through direct numerical simulations is $Ra = 10^{14}$ [4].

There are, however, other kinds of fluids characterized by very different values of Pr; for example, Earth's interior can have a Pr number varying from 10^{-2} up to 10^{23}. In particular, the Earth's mantle is characterized by high Pr ($Pr > 10^{20}$) and moderate Ra numbers ($10^5 \lesssim Ra \lesssim 10^9$) [55].

The influence of the Prandtl number on thermal convection dynamics is difficult to investigate experimentally, as Pr can be substantially changed only by changing the fluid. Examples of studies following this approach can be found in [81] and [2]. A different strategy for varying Pr was adopted in [59] and [5]. It consists of working close to the critical point

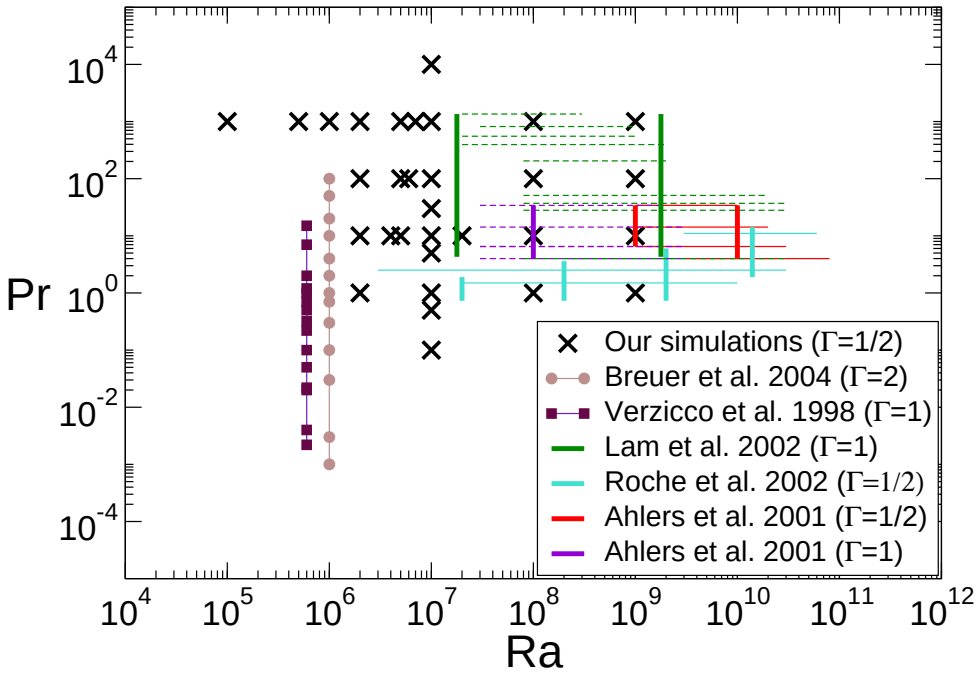

Figure 1.2: Map of performed simulations compared to the map of some recent numerical and experimental work at high Pr numbers.

of compressed gas. This technique, still using cryogenic helium [73], enables the exploration of the influence of Pr variations at quite high Ra numbers. However, in both strategies, complications arise from the great difficulty of maintaining the properties constant across the fluid depth, with consequent violation of the Boussinesq approximation, especially at high Pr numbers.

Numerical simulations can overcome these issues, even if they face other kinds of difficulties such as adequate spatial resolution and the integration over sufficiently long times. Some numerical studies deal with varying Pr numbers ([17], [12], [65], [41], [77]). Only a few of them ([12], [77]) mimic a set-up similar to experiments, thus allowing a proper comparison of the results. A smaller number of studies concerns very high-Pr regimes. On the other hand, in [77] the discussion is mainly focused on lower Pr regimes ($2.2 \times 10^{-3} \leq Pr \leq 15$). In [12] a wider range of Pr numbers is explored ($10^{-3} \leq Pr \leq 10^2$), but only at fixed $Ra = 10^6$.

In the present study we perform a numerical study of thermal convection at high-Pr regimes and moderate Ra numbers for a wide range of Pr and Ra. The aspect ratio of the

system is $\Gamma = 1/2$, comparable to this of previous experiments and numerical simulations (see fig. 1.2). The aim of this study is to provide additional data in a range of Ra and Pr not yet adequately explored, and to contribute to the comprehension of such a complex dynamical system.

From the theoretical point of view, great efforts have been devoted to capture the mechanisms of the convective system since 1916, when Lord Rayleigh derived the theoretical requirement for the development of convective motion [57]. The early works were mainly focused on the onset of motion and pattern formations [64]. The stability regimes of these patterns were mainly understood owing to the work of Busse and coworkers ([16], [15]). One of the last reviews on this respect is due to Bodenschatz *et al.* [9].

The successive theories were mainly focused on Ra beyond the onset of motion, where turbulent convection appears and power-law scaling may apply. In this contest, the principal aim was to predict a correct power-law dependence of the Nu number on Ra and Pr numbers. Some notable contributions were due to Kraichnan [44], Castaing [18] and Shraiman and Siggia [67]. A review on this part is due to Siggia [68].

Recently, in order to rearrange the main results of experiments and theoretical models, Grossmann and Lohse [32] proposed a theory based on the presence of a large scale circulation structured in a vertical roll filling a whole container of small aspect ratio ($\Gamma = O(1)$). Dividing the domain into the bulk and boundary layers, they identified several regimes in the $Ra - Pr$ phase space, defined by whether the boundary layer or the bulk dominates the global viscous and thermal dissipation, and by whether the thermal or viscous boundary layer is thicker. This model presents six free parameters that have to be set on the basis of empirical data.

None of these theories fully match every numerical and experimental results. They generally hold only on some subrange of Ra and Pr, or present inconsistencies when checked in detail. On the other hand, empirical results also disagree with each other, indicating a strong dependence on the physical set-up. The ranges of Ra and Pr where the data trends are largely accepted are limited [1].

At high Pr generally a small dependence of the Nu number on Pr is theoretically predicted ([67], [33]) and empirically found ([77], [81]), even if there are some discrepancies in the absolute strength of the Pr effect. In order to correctly catch this small dependence, in our simulations a particular care has been devoted in the choice of the grid size (chapter 2, section 2.4) and to the evaluation of the errors affecting the data (chapter 3). Long-term phenomena found in the simulations are included in the chapter on error analysis (section

3.4).

The physical set-up, the governing equations and the numerical code are described in the first part of chapter 2. In large parts of Ra and Pr ranges simulated, the available code was found to be strongly affected by numerical instabilities. A dedicated study has been performed to limit this phenomenon and to increase the code efficiency. This detailed part of the work is presented in appendix A, in order to allow an easier reading of the rest of the thesis.

The non-dimensional form of the equations based on the free-fall velocity (and used in the numerical code) was found not suitable for a correct description of high-Pr flows. A new dimensional form is proposed in chapter 4. This chapter includes the Reynolds (Re) and the Peclet (Pe) number behaviors with respect to Ra and Pr.

A qualitative picture of the transitions through several regimes characterizing the simulations performed and the typical flow structures associated with them are presented in chapter 5. Chapter 6 shows the Nusselt number behavior in the range of Ra and Pr explored. A comparison with previous results is included.

Finally, in chapter 7 we analyze local and global features of the vertical profiles and boundary layers. The comparison of trends in the behavior of boundary layers with respect to Pr, and the corresponding Re and Pe trends, allowed to find an explanation to the Nu independence of Pr.

The main results of this work are summarized in the concluding chapter 8.

Chapter 2

Physical and numerical setup

2.1 Introduction

Most of the high-Pr numerical studies are carried out in the infinite Prandtl number limit, in which all the inertial terms of the momentum equation are neglected ([39], [47]). Works studying the full problem (in which no terms are neglected) are mainly based on two-dimensional simulations ([71], [34]). Three-dimensional direct simulations of high-Pr flows still face considerable problems. To our knowledge, the full three-dimensional problem in a cell confined by solid walls has been solved for $Pr > 10$ only by Hansen [12].

In the present thesis, we perform a numerical study of thermal convection at high-Pr regimes for a moderate wide range of Ra. The flow is solved through three-dimensional time-dependent direct simulations of the full equations. The problem set-up is briefly described in section 2.2. The code used is based on a second-order accurate finite-difference scheme developed on a staggered mesh in cylindrical coordinates. Its description is given in section 2.3.

High Pr simulations are challenging owing to the computational difficulties in simulating flows which are "quasi-Stokes" and then characterized by very slow dynamics and generally strongly affected by numerical instabilities, and, at the same time, using highly refined grids that are necessary to solve the smallest scales of the temperature field. One generally deals with only one of these issues at a time, but in our study both of them are present simultaneously.

The code, used in [78], has been found numerically unstable when used to simulate high-Pr flows. The numerical instabilities appear even when the choice of the time step is small

enough to satisfy the stability limit of the time scheme. For this reason an analysis has been necessary to identify the origins of these instabilities and to limit their negative effect on the code performance (the details are given in appendix A).

Another difficulty concerns the choice of the grid size. The mesh size should be set of the same order of the smallest scale of the problem, these being the dissipative scales. At high Pr the convective dynamics are not well understood at dissipative scales. High-Pr flows are characterized by high Peclet numbers (Pe) and small Reynolds numbers (Re), and so the temperature scales are expected to be much smaller than the viscous scales. Moreover, in convective problems the temperature is an active scalar, and at high Pr it is not clear if it behaves as a passive scalar even at smallest scales, as seems to be the case at low Pr numbers. For these conditions no dissipative-scale theory is available [49]. However, we have derived the grid sizing criteria combining the classical Kolmogorov-Batchelor theory, valid for turbulent flows and passive scalars, also for the dissipative properties of the convective problem (sec. 2.4.1). These criteria have been *aposteriori* checked (sec. 2.4.4). However, the only reliable tool to assess the grid independence of the solutions and to verify their actual correctness is the refinement grid analysis (see the next chapter for details).

The problems concerning the unknown convective dynamics at high-Pr are also present on integral scales. Therefore an evaluation of the typical time scales of the problem has been carried out, in order to estimate the duration of the simulations and to verify their feasibility (sec. 2.4.2). Finally in section 2.4.3 some general information on the performed simulations is provided.

2.2 Governing equations

The problem we wish to investigate concerns the flow that develops in a cylindrical cell of aspect ratio (diameter to the cell height) $\Gamma = 1/2$. A cold and a hot temperature are imposed, respectively, on the top and the bottom plates. The sidewall is adiabatic and all the cell surfaces satisfy the no-slip condition. This set up is found in several experimental ([18], [50], [81]) and numerical works ([4], [78]).

Rayleigh and Prandtl numbers are the main dimensionless parameters governing thermal convection of a layer of fluid and are defined, respectively, as $Ra = g\alpha\Delta T H^3/(\nu\kappa)$ and $Pr = \nu/\kappa$, where g is the acceleration of gravity, H is the fluid layer depth, ΔT is the temperature difference and α, ν and κ are the fluid properties, respectively, the thermal expansion coefficient, kinematic viscosity and thermal diffusivity.

The flow is solved by the numerical integration of the three-dimensional unsteady Navier-Stokes equations with the Boussinesq approximation in the following non-dimensional form:

$$\begin{aligned} \frac{D\boldsymbol{u}}{Dt} &= -\nabla p + \Theta\hat{\boldsymbol{k}} + \left(\frac{Pr}{Ra}\right)^{\frac{1}{2}} \nabla^2\boldsymbol{u}, \qquad \nabla\cdot\boldsymbol{u} = 0, \\ \frac{D\Theta}{Dt} &= \frac{1}{(PrRa)^{\frac{1}{2}}}\nabla^2\Theta, \end{aligned} \tag{2.1}$$

with $\hat{\boldsymbol{k}}$ being the unity vector pointing in the opposite direction with respect to gravity, $\boldsymbol{u}$ the velocity vector, p the pressure separated from its hydrostatic contribution, and Θ the non-dimensional temperature. The equations have been made non-dimensional using the free-fall velocity $U = \sqrt{g\alpha\Delta TH}$, the distance between hot and cold plates H and their temperature difference $\Delta T = T_h - T_c$, respectively the temperatures of the lower (hot) and upper (cold) plates. The non-dimensional temperature Θ is defined $\Theta = (T - T_c)/\Delta T$ and its range is $0 \leq \Theta \leq 1$.

Looking at equations (2.1) it is straightforward to identify the Reynolds number

$$Re = UH/\nu \tag{2.2}$$

and the Peclet number

$$Pe = UH/\kappa \tag{2.3}$$

respectively as $Re = (Ra/Pr)^{\frac{1}{2}}$ and $Pe = (PrRa)^{\frac{1}{2}}$. Their role, however, is different from that of forced flows, since they involve the velocity scale U which is a dependent scale here. As a consequence, their relationship with Ra and Pr coming from the equations (2.1) is only formal. Indeed their definitions above involve the particular velocity scale U used to make the equations non-dimensional, instead of depending on the actual characteristic velocity of the flow, which is an unknown at this point. A deeper discussion on this respect will be given in chapter 4, while the definitions (2.2) and (2.2) of Re and Pe numbers will be used in the next sections of this chapter without a specific physical meaning, considering U as the velocity for making the equations non-dimensional, unless otherwise specified.

Another important dependent parameter is the Nusselt number (Nu), representing the ratio between the actual heat flux across the cell and the conductive heat flux that should be obtained in the absence of fluid motion. The Nu number can be calculated averaging on space and time the non-dimensional heat flux in the vertical direction $Q_z = Q_z(\theta, r, z, t)$,

defined in terms of non-dimensional quantities as follows:

$$Q_z = -\frac{\partial \Theta}{\partial z} + Pe \cdot \Theta u_z \tag{2.4}$$

The Nusselt number is often identified with a partial average of the vertical non-dimensional heat flux Q_z and considered as a function of a space direction or of time. This notation will be sometimes used also in the present work.

2.3 Numerical code

To solve the three-dimensional incompressible time-dependent equations (2.1), a second order finite-difference scheme in cylindrical coordinates is used, based on fractional-step method and staggered grid [79]. To simplify the treatment of the singularity of the Navier-Stokes equations at $r = 0$, the quantity $q_r = r \cdot v_r$ is introduced. Then, putting $q_\theta = v_\theta$ and $q_z = v_z$, the continuity equation becomes:

$$\frac{\partial q_r}{\partial r} + \frac{\partial q_\theta}{\partial \theta} + r\frac{\partial q_z}{\partial z} = 0 \tag{2.5}$$

In terms of q_i the momentum equation in conserved form becomes:

$$\begin{aligned}
\frac{Dq_\theta}{Dt} &= -\frac{1}{r}\frac{\partial p}{\partial \theta} + \frac{1}{Re}\left[\frac{1}{r}\left(\frac{\partial}{\partial r} r \frac{\partial q_\theta}{\partial r}\right) - \frac{q_\theta}{r^2} + \frac{1}{r^2}\frac{\partial^2 q_\theta}{\partial \theta^2} + \frac{\partial^2 q_\theta}{\partial z^2} + \frac{2}{r^3}\frac{\partial q_r}{\partial \theta}\right], \\
\frac{Dq_r}{Dt} &= -r\frac{\partial p}{\partial r} + \frac{1}{Re}\left[r\frac{\partial}{\partial r}\left(\frac{1}{r}\frac{\partial q_r}{\partial r}\right) + \frac{1}{r^2}\frac{\partial^2 q_r}{\partial \theta^2} + \frac{\partial^2 q_r}{\partial z^2} - \frac{2}{r}\frac{\partial q_\theta}{\partial \theta}\right], \\
\frac{Dq_z}{Dt} &= -\frac{\partial p}{\partial z} + \Theta + \frac{1}{Re}\left[\frac{1}{r}\frac{\partial}{\partial r}\left(r\frac{\partial q_z}{\partial r}\right) + \frac{1}{r^2}\frac{\partial^2 q_z}{\partial \theta^2} + \frac{\partial^2 q_z}{\partial z^2}\right],
\end{aligned} \tag{2.6}$$

with

$$\begin{aligned}
\frac{Dq_\theta}{Dt} &\equiv \frac{\partial q_\theta}{\partial t} + \frac{1}{r^2}\frac{\partial r q_\theta q_r}{\partial r} + \frac{1}{r}\frac{\partial q_\theta^2}{\partial \theta} + \frac{\partial q_\theta q_z}{\partial z}, \\
\frac{Dq_r}{Dt} &\equiv \frac{\partial q_r}{\partial t} + \frac{\partial}{\partial r}\left(\frac{q_r^2}{r}\right) + \frac{\partial}{\partial \theta}\left(\frac{q_r q_\theta}{r}\right) + \frac{\partial q_r q_z}{\partial z} - q_\theta^2, \\
\frac{Dq_z}{Dt} &\equiv \frac{\partial q_z}{\partial t} + \frac{1}{r}\frac{\partial q_z q_r}{\partial r} + \frac{1}{r}\frac{\partial q_z q_\theta}{\partial \theta} + \frac{\partial q_z^2}{\partial z},
\end{aligned} \tag{2.7}$$

where, in the q_θ equation, the following identities have been used:

$$\begin{aligned} &\frac{1}{r}\left(\frac{\partial}{\partial r} r \frac{\partial q_\theta}{\partial r}\right) - \frac{q_\theta}{r^2} = \frac{\partial}{\partial r}\left(\frac{1}{r}\frac{\partial r q_\theta}{\partial r}\right), \\ &\frac{1}{r^2}\frac{\partial r q_\theta q_r}{\partial r} = \frac{1}{r}\frac{\partial q_\theta q_r}{\partial r} + \frac{q_\theta q_r}{r^2}. \end{aligned} \tag{2.8}$$

In a similar way, the thermal equation assumes the form:

$$\frac{D\Theta}{Dt} = \frac{1}{Pe}\left[\frac{1}{r}\frac{\partial}{\partial r}\left(r\frac{\partial \Theta}{\partial r}\right) + \frac{1}{r^2}\frac{\partial^2 \Theta}{\partial \theta^2} + \frac{\partial^2 \Theta}{\partial z^2}\right], \tag{2.9}$$

with

$$\frac{D\Theta}{Dt} \equiv \frac{\partial \Theta}{\partial t} + \frac{1}{r}\frac{\partial q_r \Theta}{\partial r} + \frac{1}{r}\frac{\partial q_\theta \Theta}{\partial \theta} + \frac{\partial q_z \Theta}{\partial z}. \tag{2.10}$$

It might seem that the above equations contain many singularities. In fact, most of them are only artificial. Indeed, the advantage of using a staggered grid is that only the q_r component is evaluated at the grid point $j = 1$ ($r = 0$), and, at that point, $q_r = 0$ by definition. The only difficulties arise from the viscous derivatives with respect to r of q_θ and q_z. Their treatment is given in detail in [79].

The time discretization of the governing equations is based on a fractional step method [22] which consists for the Navier-Stokes equations to solve an intermediate velocity field $\hat{\boldsymbol{q}}$ by the diffusion-transport equation and then to correct it in the second step. The problem is then split in two parts. The predictor evaluates the intermediate non-solenoidal velocity field:

$$\begin{cases} \dfrac{\hat{\boldsymbol{q}} - \boldsymbol{q}^n}{\Delta t_n} = -(\alpha_l + \beta_l)\mathcal{G}p^n + \gamma_l H^n + \rho_l H^{n-1} + \ldots \\ \qquad\qquad \ldots + \left[\left(\mathcal{C} + \dfrac{\mathcal{L}}{Re}\right)\dfrac{(\alpha_l \boldsymbol{q}^n + \beta_l \hat{\boldsymbol{q}})}{2}\right] \quad \text{in } \Omega \\ \hat{\boldsymbol{q}} = \boldsymbol{q}^{n+1} = 0 \quad \text{on } \partial\Omega, \end{cases} \tag{2.11}$$

where Ω is the computational domain. The coefficients α_l, β_l, γ_l and ρ_l arise from the time scheme, which is described later. H here represents: the convective terms without the azimuthal derivatives, the viscous terms with a single velocity derivative, and the temperature term. $\mathcal{G}$ and $\mathcal{L}$ are differential operators, respectively, of the gradient and the Laplacian in cylindrical coordinates; $\mathcal{C}$ contains the convective terms with the azimuthal derivatives and the viscous terms which are not included in the Laplacian operator $\mathcal{L}$ and in H. The terms in the square brackets are computed implicitly whereas the other terms are computed explicitly. This means that the non-linear terms in the azimuthal direction are treated im-

plicitly [76] and are linearized only for the azimuthal velocity, avoiding to solve a non-linear coupled system [3]. Ultimately, $\mathcal{C}$ results a linear operator as $\mathcal{L}$.

Using the delta-form $\Delta\boldsymbol{q} = (\hat{\boldsymbol{q}} - \boldsymbol{q}^n)$ it turns out that

$$\begin{aligned}\left[1 - \beta_l \Delta t_n \left(\mathcal{C} + \frac{\mathcal{L}}{Re}\right)\right](\hat{\boldsymbol{q}} - \boldsymbol{q}^n) = \Delta t_n \Big[&- (\alpha_l + \beta_l)\mathcal{G}p^n + \dots \\ &\dots + \gamma_l H^n + \rho_l H^{n-1} + (\alpha_l + \beta_l)\left(\mathcal{C} + \frac{\mathcal{L}}{Re}\right)\boldsymbol{q}^n\Big].\end{aligned} \tag{2.12}$$

Defining $\mathcal{A} = \mathcal{A}_\theta + \mathcal{A}_r + \mathcal{A}_z = (\mathcal{C} + \mathcal{L}/Re)$ and $\sigma_l = \beta_l \Delta t_n$ it is possible to factor the left side of (2.12) in the following manner [42]:

$$\begin{aligned}&(1 - \sigma_l \mathcal{A}_\theta)(1 - \sigma_l \mathcal{A}_r)(1 - \sigma_l \mathcal{A}_z)(\hat{\boldsymbol{q}} - \boldsymbol{q}^n) = \dots \\ &\qquad \dots = \Delta t_n \left[-(\alpha_l + \beta_l)\mathcal{G}p^n + \gamma_l H^n + \rho_l H^{n-1} + (\alpha_l + \beta_l)\mathcal{A}\boldsymbol{q}^n\right].\end{aligned} \tag{2.13}$$

The equation (2.13) is an $O(\Delta t^3)$ approximation to eq. (2.12). However, it requires inversions of tridiagonal matrices rather than inversion of a large sparse matrix, as in the case of (2.12). This results in a significant reduction of computational cost and memory.

Hence, the intermediate velocity $\hat{\boldsymbol{q}}$ is corrected at the second step solving the coupled problem:

$$\begin{cases} \dfrac{\boldsymbol{q}^{n+1} - \hat{\boldsymbol{q}}}{\Delta t_n} = -(\alpha_l + \beta_l)\mathcal{G}\Phi^{n+1} \quad \text{in } \Omega \\ \mathcal{D}\boldsymbol{q}^{n+1} = 0 \quad \text{in } \Omega \\ \boldsymbol{q}^{n+1} = 0 \quad \text{on } \partial\Omega, \end{cases} \tag{2.14}$$

where $\mathcal{D}$ is the divergence operator and Φ is a scalar quantity that can be derived by coupling the first equation of (2.14) with the first equation of (2.11). The Φ results then related to the pressure by

$$p^{n+1} = \Phi^{n+1} + p^n - \frac{\beta_l \Delta t_n}{Re}\mathcal{L}\Phi^{n+1}. \tag{2.15}$$

From the application of divergence operator to the first equation of (2.14) follows the Poisson equation

$$\mathcal{L}\Phi^{n+1} = \frac{1}{(\alpha_l + \beta_l)\Delta t_n}\mathcal{D}\hat{\boldsymbol{q}}, \tag{2.16}$$

which allows the calculation of Φ^{n+1}. The equation (2.16) is solved using a trigonometric expansion in the azimuthal direction and a direct approach in the other two directions. It is interesting that this equation does not need boundary conditions because, in the staggered mesh, Φ^{n+1} is defined at the center of each cell, therefore there is sufficient number of

equations for $\boldsymbol{q}^{n+1}$ and Φ^{n+1}, without the need of additional conditions for Φ^{n+1}. Instead, the appropriate boundary conditions for the intermediate field $\hat{\boldsymbol{q}}$ are derived consistently with the governing equations [79] and are already included in the eqs. (2.11).

The logical sequence for solving the problem is then to calculate the intermediate velocity $\hat{\boldsymbol{q}}$ by eq. (2.13), subsequently to obtain the scalar Φ^{n+1} through the Poisson equation (2.16) and after that to update the velocity field $\boldsymbol{q}^{n+1}$ by the first of the equations (2.14) and, at the end, to update the pressure p^{n+1} by eq. (2.15).

The same strategy is applied to the thermal equation, except that the scalar field does not need any correction:

$$\frac{\Theta^{n+1}-\Theta^{n}}{\Delta t_n} = \gamma_l H^n + \rho_l H^{n-1} + \left[\left(\mathcal{C}+\frac{\mathcal{L}}{Pe}\right)\frac{\alpha_l\Theta^n+\beta_l\Theta^{n+1}}{2}\right]. \tag{2.17}$$

This numerical scheme globally satisfies the conservation of mass at every time step. Moreover it preserves the global conservation of momentum, kinetic energy and circulation in the absence of time-differencing error and viscosity[1] [42]. It is known that failure to preserve these conservation properties can lead to numerical instabilities [56] and that to stabilize the calculations, artificial viscosity is often introduced, either explicitly or implicitly, by using dissipative finite-difference schemes, especially for high Reynolds number flows. In the present case this approach is not required[2].

The time integration of the previous equations is computed by a low-storage third order Runge-Kutta method for the explicit terms which are summarized in N and by the Crank-Nicolson scheme for the implicit terms summarized in L. The scheme to advance from $\boldsymbol{q}^n$ at time t to $\boldsymbol{q}^{n+1}$ at time $t+\Delta t_n$ has three substeps:

$$\begin{aligned}
\boldsymbol{q}' &= \boldsymbol{q}^n + \Delta t_n\left[L(\alpha_1\boldsymbol{q}^n+\beta_1\boldsymbol{q}')+\gamma_1 N(\boldsymbol{q}^n)\right]\\
\boldsymbol{q}'' &= \boldsymbol{q}' + \Delta t_n\left[L(\alpha_2\boldsymbol{q}'+\beta_2\boldsymbol{q}'')+\gamma_2 N(\boldsymbol{q}')+\rho_2 N(\boldsymbol{q}^n)\right]\\
\boldsymbol{q}^{n+1} &= \boldsymbol{q}'' + \Delta t_n\left[L(\alpha_3\boldsymbol{q}''+\beta_3\boldsymbol{q}^{n+1})+\gamma_3 N(\boldsymbol{q}'')+\rho_3 N(\boldsymbol{q}')\right],
\end{aligned} \tag{2.18}$$

where, at each substep, the whole fractional step procedure is implied. For N this is a Wray's scheme which is, for each substep, like a Euler explicit or a second-order Adams-

[1] The energy conservation properties of a code can be investigated checking the time-reversibility of the corresponding Euler equations. This kind of analysis has been recently carried out in [27], showing in this respect that a low order finite difference solver can reproduce results better than a higher order or a pseudo-spectral solver. This is due to the fact that, *"although the flow statistics are significantly affected by the accuracy of the space discretization, the time-reversibility is not because most of the space discretizations are time-reversible for an exact time-stepping"* [27].

[2] These numerical instabilities are different from those affecting the code and discussed in appendix A. Indeed, in that case, the viscous terms originate the instabilities, while in the present case the viscosity has a stabilizing effect.

Bashfort, but with different coefficients γ and ρ. For L this is like Crank-Nicolson scheme on each substep but again with different coefficients. The advantage of this scheme is that it needs minimum storage, actually not much more than the Euler explicit scheme for the present methods. A disadvantage in comparison with Adams-Bashforth is that there are three different implicit operators $(1 - \Delta t_n \beta L)$ in (2.18), so it is costlier to pre-compute, pre-invert and store them. In our scheme, those operators are not pre-computed because the time step is kept variable.

The general scheme (2.18) has 11 unknown coefficients and must satisfy 17 equations for an overall third-order accuracy. These equations arise from the match of (2.18) with the third-order Taylor expansion of the general equation

$$\frac{\partial \boldsymbol{q}}{\partial t} = N(\boldsymbol{q}) + L(\boldsymbol{q}). \tag{2.19}$$

However, if the length of the substeps in the scheme for L and the scheme for N is kept to be the same, then the following relations have to be satisfied:

$$\alpha_l + \beta_l = \gamma_l + \rho_l \qquad \text{for} \quad l = 1, 2, 3\ , \tag{2.20}$$

where $\rho_1 = 0$. This reduces the system to eight equations in eight unknowns. These equations were derived by [42] and, accounting for (2.20), they are, for the first order,

$$\gamma_1 + \gamma_2 + \gamma_3 + \rho_2 + \rho_3 = 1; \tag{2.21}$$

for the second order,

$$\gamma_3 \left(\gamma_1 + \gamma_2 + \rho_2\right) + \gamma_1 \left(\rho_3 + \gamma_2\right) = \frac{1}{2} \tag{2.22}$$

$$\begin{aligned} \gamma_1\beta_1 + \gamma_1(\gamma_2 + \rho_2) + (\gamma_2 + \rho_2)\beta_2 + \dots \\ \dots + (\gamma_3 + \rho_3)(\gamma_1 + \gamma_2 + \rho_2) + \beta_3(\gamma_3 + \rho_3) = \frac{1}{2}; \end{aligned} \tag{2.23}$$

for the third order,

$$\gamma_1\gamma_2\gamma_3 = \frac{1}{6} \tag{2.24}$$

$$\gamma_1^2(\gamma_2 + \rho_3) + \gamma_3(\gamma_1 + \rho_2 + \gamma_2)^2 = \frac{1}{3} \tag{2.25}$$

$$\beta_3 \left[\gamma_3(\gamma_1 + \gamma_2 + \rho_2) + \gamma_1\rho_3\right] + \gamma_1\gamma_2(\gamma_3 + \rho_3) + \gamma_1\gamma_2\beta_2 = \frac{1}{6} \tag{2.26}$$

$$\gamma_3 \left[\gamma_1\beta_1 + (\gamma_2 + \rho_2)(\gamma_1 + \beta_2)\right] + \gamma_1\beta_1(\gamma_2 + \rho_3) = \frac{1}{6} \tag{2.27}$$

$$\begin{aligned}
&\left[(\gamma_1+\beta_2+\beta_3)(\rho_2+\gamma_2)+(\beta_3+\beta_1)\gamma_1+\beta_3^2\right]\rho_3+\dots\\
&\qquad\dots+\left[(\gamma_1+\beta_2+\beta_3)\gamma_3+(\beta_2+\beta_1)\gamma_1+\beta_2^2\right]\rho_2+\dots\\
&\qquad\dots+\left[(\gamma_1+\beta_2+\beta_3)\gamma_2+(\beta_3+\beta_1)\gamma_1+\beta_3^2\right]\gamma_3+\dots\\
&\qquad\dots+\left[(\beta_2+\beta_1)\gamma_1+\beta_2^2\right]\gamma_2+\beta_1^2\gamma_1=\tfrac{1}{6}.
\end{aligned} \tag{2.28}$$

Unfortunately such a non-linear system of equations (2.21)-(2.28) does not have any known solutions. However a smaller system can be solved obtaining infinite possible solutions at the price of lower accuracy. In the code implemented by [79] the following coefficients were adopted:

$$\beta_l=\alpha_l \qquad \text{for} \quad l=1,2,3 \tag{2.29}$$

$$\gamma_1=\frac{8}{15}, \qquad \gamma_2=\frac{5}{12}, \qquad \gamma_3=\frac{3}{4}, \tag{2.30}$$

$$\rho_1=0, \qquad \rho_2=-\frac{17}{60}, \qquad \rho_3=-\frac{5}{12}. \tag{2.31}$$

Combining relations (2.20) and (2.29), it is possible to obtain explicitly the α and β coefficients:

$$\alpha_1=\beta_1=\frac{4}{15}, \qquad \alpha_2=\beta_2=\frac{1}{15}, \qquad \alpha_3=\beta_3=\frac{1}{6}. \tag{2.32}$$

The relations (2.29) mean that the scheme for L is Crank-Nicolson, and the coefficients (2.30) and (2.31) represent a solution of the Wray's Runge-Kutta scheme for N. Consequently, the time scheme for the explicit terms is of the third-order, while that for the implicit terms is of the second-order.

The code described above is characterized by the following Courant-Friedrichs-Lewy (CFL) stability condition:

$$CFL=\Delta t\left(\frac{|u_z|}{\Delta z}+\frac{|u_r|}{\Delta r}\right)\leq\sqrt{3}. \tag{2.33}$$

This constraining condition for the time step size derives from the explicit non-linear terms of the momentum equation. In order to maximize the time step size, it can be set dynamically by evaluating the CFL condition (2.33) at each time step.

Unfortunately, the simulations characterized by low Reynolds numbers and performed using the criterion (2.33) become unstable. Almost all the simulations with Ra and Pr in the range of our interest have small Re numbers, and the results are affected by such instability problem.

The issues generated by the failure of condition (2.33) are mainly two. One is that to obtain stable solutions the time step must be set one or two orders of magnitude smaller than

that required by the stability limit (2.33), with consequent reduction of computing efficiency. The other one is the impossibility to evaluate *apriori* the time step size due to absence of a clear stability criterion, with further waste of resources in the attempts of discovering the stable time step size of each simulation.

In order to overcome these issues, an analysis of the numerical instabilities has been carried out and the details are reported in appendix A. Using simulations data, a new stability criterion has been empirically determined (see eq. (A.11) of appendix A). Besides, to minimize the effect of these instabilities, new coefficients for the time scheme (2.18) were implemented instead of the coefficients (2.30) and (2.31). As a consequence, a 40% increase of the code performance was obtained. The combination of this code performance improvement together with the correct criterion to set the time step size allowed an overall efficiency increase of even 100%. In spite of this gain, the simulations of high Pr still remain challenging, as shown later in figure 2.4.

2.4 Grid resolution criteria

2.4.1 *Apriori* estimate of the grid size

The criterion that must be respected in direct numerical simulations is that the grid size must be of the same order as the smallest scales of the flow. For turbulent flows the smaller scales correspond to the Kolmogorov scale η [43]. Moreover the viscous boundary layer δ_u must be adequately resolved near the solid surface. This means that, within the boundary layer thickness, an adequate number of grid points must be inserted and this condition is usually more restrictive than the previous one. The temperature field has similar resolution requirements given by the Batchelor scale $\eta_B = \eta Pr^{-1/2}$ for $Pr \geq 1$ or the Obukhoff-Corrsin scale $\eta_C = \eta Pr^{-3/4}$ for $Pr < 1$ in the bulk flow [6]. In addition the thermal boundary layer δ_T has to be considered. The above constraints must be satisfied simultaneously, therefore the most restrictive condition must be used.

At high Prandtl numbers the conductive effects become important at scales which are smaller than the viscous scales ($Pe > Re$), therefore the Batchelor scale is smaller than the Kolmogorov scale ($\eta_B < \eta$) and the thermal boundary layer is smaller than the viscous one ($\delta_T < \delta_u$). Then the grid size must depend on temperature scales. On contrast, at low Pr numbers the viscous scales are more constraining and they must be considered for grid-sizing. Given that only one simulation was performed at $Pr < 1$, we will focus our attention mainly on $Pr \geq 1$.

Considering the non-dimensional form of the Kolmogorov scale[3] : $\eta/h = [1/(Re^3\epsilon)]^{1/4}$ and using the relationship between the non-dimensional total dissipation rate ϵ and the Nusselt number (eq. (3.3)), a reasonable estimate for Batchelor scale is given by:

$$\eta_B/h \simeq (1/Ra(Nu-1))^{1/4} \tag{2.34}$$

On the other hand, an estimate of the thermal boundary layer thickness can be the following:

$$\delta_T/h \simeq 1/(2Nu) \tag{2.35}$$

Relation (2.35) means that the total temperature difference ΔT is experienced totally inside the two boundary layers while the temperature in the bulk flow is approximately uniform and equal to the mean temperature $(T_h + T_c)/2$.

At this point, knowing the Nusselt number, estimates of η_B and δ_T are easily obtained. Unfortunately, the dependence of Nu on Ra and Pr is unknown, and has to be calculated through the simulations. However, this dependence can be found in the existing literature. In particular, given that for $Pr \geq 1$ the Nu number results to be a weak function of Pr [77], it is possible to use the values of Nu calculated in analogue numerical works where Pr is of order one ([53], [78]). It is worth noting that if Nu is independent of Pr, even the Batchelor scale estimated by (2.34) and the thermal boundary layer thickness estimated by (2.35) result to be independent of Pr. This means that the same grid used for simulations at $Pr \sim O(1)$ can be theoretically used also at much higher Pr.

Usually at $Pr \sim O(1)$ the number of grid points within the thermal boundary layer to be used for accurate results vary from 6 to 14 ([78], [28]) and this condition is more restrictive than that imposed by Batchelor scale. Therefore a non-uniform distribution of grid points is generally used, with more points clustered close to the boundaries [78]. However, it has to be considered that at high Pr numbers, very thin structures are expected to detach from the boundary layers and to reach the opposite plates [38]. Thus the resolution requirements imposed inside the boundary layer should be extended to the whole flow. This would mean

[3]Following the theory for fully developed turbulent flows, and considering that the temperature field behaves as a passive scalar at dissipative scales (i.e. Bolgiano scale [10] is much higher than dissipative scales), the non-dimensional dissipation rate ϵ should be a constant of order one [49]. Then, the estimate of the Batchelor scale should be given by $\eta_B/h \sim Re^{-3/4}Pr^{-1/2}$. The point is that in thermal convection Re is an unknown function of Ra and Pr. The scaling behavior of Re with respect to Ra and Pr changes with varying Ra and Pr [32], and is not clear *apriori* what are the correct dependencies for our simulations. Further uncertainty derives from the fact that our simulations are characterized by low Re numbers and the above hypotheses are far from being satisfied. As a consequence considering ϵ as a constant could be not reasonable. The Batchelor scale estimate (2.34) is instead based on an analytical relationship between ϵ and Nu valid for any stationary solution. The only *apriori* evaluation concerns the Nu values (see table 2.1).

Ra	Nu	δ_T/h	η_B/h	n_θ	n_r	n_z	Δ_{min}	Δ_{mean}	Δ_{max}	N_{δ_T}
10^5	3,5	0,1429	0,0447	109	18	70	0,0047	0,0111	0,0138	11
				161	26	101	0,0028	0,0075	0,0094	15
10^6	8	0,0625	0,0194	101	25	101	0,0028	0,0089	0,0122	10
				121	45	201	0,0017	0,0054	0,0068	14
10^7	18	0,0278	0,0088	129	31	136	0,0020	0,0069	0,0094	7
				217	55	217	0,0012	0,0041	0,0051	7
10^8	35	0,0143	0,0041	217	75	301	0,0008	0,0033	0,0043	6
				385	813	321	0,0005	0,0026	0,0037	11

Table 2.1: *Apriori* estimate of the most important pairs of grids. The values of the thermal boundary layer thickness δ_T and of the Batchelor scale η_B were estimated using respectively the relationships (2.35) and (2.34). The Nu numbers were extrapolated from [78]. The first row of each pairs represents a coarse grid, while the second row represents the corresponding refined grid. Δ_{min}, Δ_{mean} and Δ_{max} are the respectively the minimum, mean and maximum value of the non-dimensional grid size: $\Delta = (2\pi r \Delta\theta \Delta r \Delta z)^{1/3}$. N_{δ_T} is the number of points inside δ_T.

that at high Pr an uniform grid is more suitable. On the other hand, the Re decreases with Pr ([52], [46]). Then at high Pr and moderate Ra the flow is expected not to be really turbulent, and a laminar flow usually needs less resolution to be correctly solved.

Practically two types of grids were chosen at some reference values of Ra. The first one was set smaller on average than the Batchelor scale evaluated by (2.34), and $6 - 11$ points were placed inside the thermal boundary layer evaluated by (2.35). The second type of grids was chosen to have a more uniform distribution of points in the bulk and generally more points in the thermal boundary layer (see table 2.1).

The coarser grids were used to perform almost all the simulations, adopting a grid set at a given Ra also for simulations at lower Ra[4]. The refined grids were generally used to verify the results in several Pr and Ra numbers conditions. At $Ra = 10^8$, instead, the refined grid was used to perform simulations at varied Pr numbers and the coarser grid was used for checking the results. A refined grid for some simulations can represent a coarse grid for other more constraining simulations. In particular, due to computational limitations, at $Ra = 10^9$, the refined grid set for simulations at $Ra = 10^8$ was used for $Pr \geq 100$, while for $Pr \leq 10$ the coarse grid set at $Ra = 10^8$ was considered[5]. However, having the flow at higher Ra thinner boundary layers, more points were clustered close to the walls in both cases. Figure 2.1 shows a map of the simulations with the corresponding grids.

[4]Grids set at a given Ra were also used sometimes at higher Ra, obtaining positive response from *aposteriori* tests.

[5]Those defined as coarse grids are generally more refined than the grids previously used to solve the same problem at $Pr = 0,7$ ([78], [28]). Then, having verified the small influence of Pr number, we expected to obtain satisfactory results at $Ra = 10^9$ using not only the refined grid but also the coarse grid sized for $Ra = 10^8$. However, at higher Pr the most refined grid was preferred.

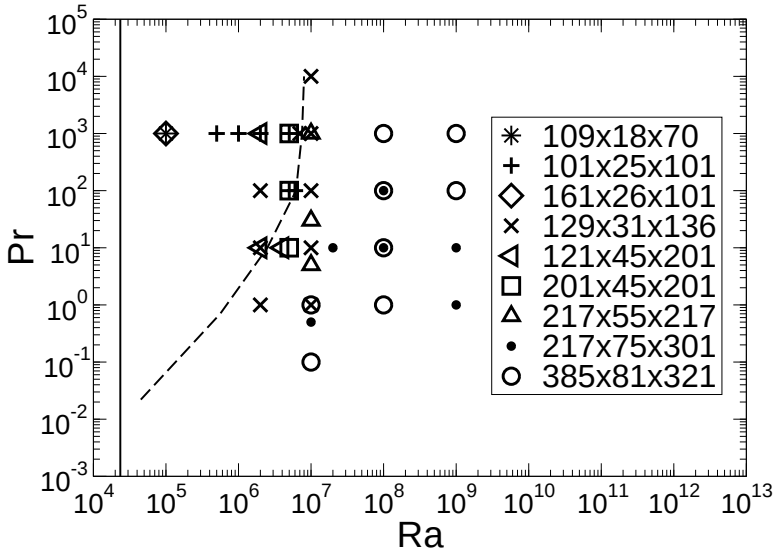

Figure 2.1: Map of simulations performed in a cylindrical cell of aspect ratio $\Gamma = 1/2$. Legend shows the corresponding number of grid points in the azimuthal, radial and vertical directions. The vertical solid line represents the critical Ra for the onset of convection [53]. The dashed line represents the empirically determined threshold Ra to pass from steady to unsteady flow.

2.4.2 Maximum and minimum typical time estimates

In order to estimate the maximum time step size for an adequate time resolution and the minimum time interval for a good description of all physical phenomena, it is useful to introduce some typical time scales of the problem. The commonly used characteristic time scale in this kind of flow is the convective time τ_c, defined as the time that a particle of fluid needs to cross the cell depth h with a typical velocity U_c of the large scale structures[6]: $\tau_c = h/U_c$. It is important to note that in thermal convection problem U_c is an unknown that has to be calculated (for more details see chapter 4). Therefore, the convective time τ_c is unknown *apriori*.

At $Pr \sim O(1)$ the convective velocity U_c is usually considered of the same order of the free-fall velocity $U = \sqrt{\alpha g \Delta T h}$ [78]. This velocity comes from the balance between the buoyancy term and the inertial term of the momentum equation [74]. Then τ_c can be estimated as the free-fall time $\tau = h/U$. On the contrary, at high Pr, since the first simulations, it was clear that U_c could be an order of magnitude smaller than U (depending on Pr). As a consequence at high Pr the convective time τ_c was expected to be much higher than τ.

Other two important typical times are the diffusion time of momentum $\tau_\nu = h^2/\nu$ and heat $\tau_\kappa = h^2/\kappa$, with h equal to the maximum cell size [31]. Their ratio with respect to the convective time is, respectively, equal to the Reynolds number and the Peclet number based on the convective velocity: $\tau_\nu/\tau_c = Re_c = U_c h/\nu$ and $\tau_\kappa/\tau_c = Pe_c = U_c h/\kappa$.

Theoretically, a simulation should last longer than the longest typical time of the problem. At $Pr \geq 1$ and at moderate Ra the longest time was estimated by τ_κ, expecting[7] $Pe_c \geq Re_c$. Considering $Pr \simeq 1$ and consequently[8] $Pe_c \sim \sqrt{RaPr}$, it is very challenging to satisfy this condition at moderate-high Ra numbers. Typically at $Pr \sim O(1)$ the numerical simulations are few hundreds of convective time long ([58],[78]), that are much shorter than the diffusion time τ_κ. However, if the flow is turbulent enough and Pr is of order one, the convective dynamics are driven by the advective ones[9], strongly prevailing on the diffusive phenomena.

[6] In several papers the characteristic time scale is actually considered the large-eddy turn over time τ_L. It can be defined as the time that a fluid particle spends to revolve around the largest eddy that can be accommodated in the cell [76]. This choice is due to the fact that most of the convective flows, simulated in small aspect ratio cells, are characterized by a single large-scale circulation-roll filling the whole cell. In a cell of aspect ratio 1/2 however different kinds of circulation structures are expected [78], and the large-eddy turn over time could lose its precise meaning. For this reason a more general definition of the convective time has been preferred. However, in case of single roll structures, for cell of aspect ratio 1/2, one can consider $\tau_L \approx 2\tau_c$ [78].

[7] At $Pr \leq 1$ the longest scale is instead τ_ν. However for $Pr \simeq 1$ it is $\tau_\nu \simeq \tau_\kappa$.

[8] Since $U_c \simeq U$ at $Pr \simeq 1$, Pe_c can be estimate by Peclet based on the free fall velocity U.

[9] The term *convection* is referred to the dynamics deriving from the interaction of the temperature field (active scalar) and of the velocity field though the buoyancy term (see eqs. (2.1)). Then a distinction has to be made between *convection* and *advection*. In fact, the convection phenomenon can have advective or

The diffusive dynamics remain confined in small regions of the flow, such as the boundary layers, where the typical length scales are very small and, as a consequence, the typical diffusive times are locally very small too. Besides, very slow and smooth dynamics linked to the integral diffusive time scales are expected to be quite separated from the faster and irregular advective dynamics in such a way as not to interact with each other, allowing us to study the second one while neglecting the first.

On the contrary, still considering $Pr \sim O(1)$, if the Re is small, the diffusive dynamics are not negligible with respect to the advective ones and the convection phenomena are also influenced by diffusion at integral scales. As a consequence, performing simulations longer than τ_κ is mandatory. However, small Re correspond to small Ra numbers and then also to not extremely[10] high τ_κ.

The issue becomes more complex at high Pr, because Pe is expected to be much higher than Re, with Re decreasing as Pr increases. This means that the velocity field and the temperature field are not expected to be driven by the same dynamics. The temperature field mainly is dominated by advection and the velocity field by diffusion. The resulting convection dynamics are unclear, so it was not possible to estimate *apriori* if the main dynamics could be captured by simulations run for a time much shorter than τ_κ or if simulations longer than τ_κ would be necessary. In the last case, to obtain significant results from numerical simulations at high Pr and moderate Ra should be fairly impossible, due to computational constrains. Presumably however the momentum diffusion time $\tau_\nu \, (\ll \tau_\kappa)$ should play a prevailing role with respect to τ_κ.

The maximum time step suitable for an adequate time resolution can be estimated with the same approach used to obtain the grid size. It is possible to calculate the Kolmogrov time scale $t_\eta = (\nu/\epsilon)^{1/2}$ in the non-dimensional form as $t_\eta/\tau = (Pr/(Nu-1))^{1/2}$ using the relationship between ϵ and Nu. In a similar manner, for the temperature field, the Batchelor time scale $t_{\eta_B} = t_\eta Pr^{-1/6}$ is given by $t_{\eta_B}/\tau = (Pr^{2/3}/(Nu-1))^{1/2}$. Increasing these time scales with Pr, the worse conditions[11] are at $Pr \simeq 1$. However, also in this last case, the time step size associated to the dissipation rate is not really constraining, at least for moderate Ra numbers[12].

diffusive features, or a combination of them.

[10] Oresta *et. al.* [53] estimated, in a cylindrical cell with $\Gamma = 1/2$, the transition to turbulent flow corresponding to $Ra \approx 10^6$ ($Pr = 0.7$). Therefore, τ_κ/τ ($\simeq \sqrt{Ra}$) resulted of the order of 10^3, which is large from the numerical point of view. However, all the simulations at lower Ra were performed for a longer time [53]. This was possible because at smaller Re coarser grids are sufficient to correctly resolve the flow.

[11] At $Pr < 1$ the Obukhoff-Corrsin time scale $t_{\eta_C} = t_\eta Pr^{-1/2}$ has to be considered instead of the Batchelor time scale. However, resulting t_{η_C} increasing as Pr decreases, the Kolmogorov time scale t_η represents in this case a most constraining condition.

[12] For $Ra = 10^9$ and $Pr = 1$, $t_{\eta_B}/\tau \simeq 0,12$.

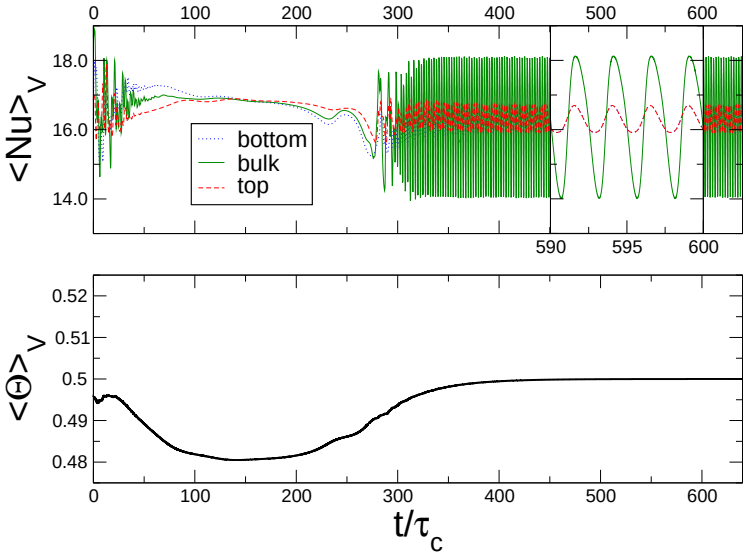

Figure 2.2: Simulation at $Ra = 10^7$ and $Pr = 10^3$. The top graph shows the Nusselt number and the bottom one the volume averaged temperature. Both the signals are a function of convective time units t/τ_c, where $\tau_c = \tau\sqrt{Pr}$ and τ the free-fall time.

Given that it is not clear what the smallest time scales inside the boundary layers should be, in agreement with [53], a rough estimate is done considering a time step at least 50 time smaller than the free-fall time τ ($\Delta t/\tau \leq 0.02$). Given that τ_c is expected much higher than τ at high Pr, this condition becomes more restrictive as Pr increases.

The maximum time step is set smaller than the most constraining of the above conditions. However these conditions are generally much less constraining than those due to the numerical stability conditions, described in appendix A.

2.4.3 General information on simulations

First simulations at $Pr = 1$ and $Pr = 10$ were started introducing a small harmonic disturbance in the temperature field. They are executed until stationary solutions have been reached. At that point the results were used to a start higher Pr simulations with the same grid. This procedure, costly in terms of time, was necessary to overcome numerical instabilities in the initial transient. In some cases, simulations at lower Ra were used to start simulations at higher Ra. Each simulation is, however, characterized by an initial numerical transient during which almost all the quantities lose their physical meaning. Only after that a physical transient is established. Thus, the start phase of the simulations was not

well controlled, being affected by unavoidable numerical transient that is usually large in strength although quite short in time.

During the simulations the bulk Nusselt number, defined as the volume average of eq. (2.4), was monitored, representing the typical quantity mainly influenced by the convective phenomena and then providing an indication of the convective time scale τ_c. The heat flux averaged on the top plate and that averaged on the bottom plate have been monitored as well; they should converge on average to the bulk Nusselt value (see sec. 3.2 for more details). The comparison of these signals gives an indication of when the transient phases are finished. Another quantity that is monitored in time is the temperature averaged on the whole volume. This signal, which for Boussinesq approximation and in non-dimensional form, should converge to 1/2, was found sensitive to the slowest dynamics of the flow. Velocities, temperature and pressure signals in several points of the domain were also monitored.

The steady and periodic solutions have been run until stable values of all the monitored quantities were reached. In particular, the simulations were continued until the volume averaged temperature, after reaching a constant value, maintained its first six digits unchanged for at least 100 convective times. The convective time is here taken as $\tau_c = \tau\sqrt{Pr}$ (see chapter 4 for details). Figure 2.2 shows an example of periodic solution. It is characterized by long transient phases ($t_{trans} \gg 100\,\tau_\nu$). This behavior is found to be typical of simulations having Ra close to threshold value Ra_U for transition from steady to periodic flow.

The unsteady simulations have been run for sufficiently long time windows to obtain statistically convergent quantities. In particular, after the initial transient, each simulation continued for at least $500\,\tau_c$. This, however, represented a minimum requirement, because an anomalous behavior was encountered in the volume averaged temperature signal. Then longer simulations, typically of the order of $1000 - 2000\,\tau_c$, were performed trying to explore this anomaly. In particular, at $Ra = 10^8$ long period oscillations were found to arise in the volume averaged temperature signal as Pr increases, while the convective time scale oscillations were found to smooth out (see fig. 2.3). These long period phenomena could be driven by diffusion dynamics such as hypothesized in the previous section, and the thermal diffusion time could play a role. Indeed, those slow oscillations at fixed Ra seem to have a similar period for different Pr if that period is evaluated in terms of convective time τ_c, but also if it is evaluated in terms of diffusion time τ_κ, being $\tau_k/\tau_c = Pe_c \simeq \sqrt{Ra}$ independent[13] of Pr. Simulations much longer than τ_κ would be necessary to verify the

[13]The momentum diffusion time τ_ν was excluded from considerations about the frequency of very slow phenomena because it is strongly dependent on Pr ($\tau_\nu/\tau_c = Re_c \simeq \sqrt{Ra}/Pr$). However, the momentum diffusion dynamics play an increasingly important role as Pr increases, and slow dynamics, together with the typical convective dynamics, can derive from a combination of the advection of the temperature field and

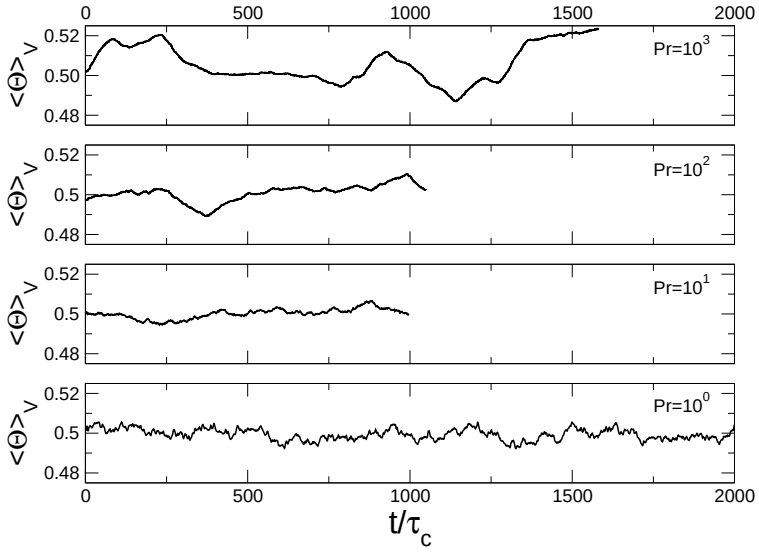

Figure 2.3: Signal of volume averaged temperature at $Ra = 10^8$ for varied Pr. The signal shows an anomalous behavior for large Pr.

presence of thermal diffusion dynamics at integral scales. Unfortunately it was not possible to perform simulations at $Ra = 10^8$ longer than $0.1-0.2\,\tau_\kappa$ due to computational limitations. In any case, a deeper analysis of the data showed some interesting partial results that are presented in section 3.4. At $Ra = 10^9$ the simulations are too short in terms of thermal diffusion time to exhibit possible long period dynamics.

The computational limitations in this work were mainly due to the duration of simulations at high Pr rather than to the grid size, which was kept almost the same for $Pr \geq 1$ (see section 2.4.1). Indeed, once the grid was fixed, obtaining a comparable amount of data for simulations at high Pr with respect to those at $Pr \simeq 1$ required a longer computational time. This was due to the decrease of time step with increasing Pr. In particular, for high Pr (and low Re), the maximum allowable time step Δt_{max} was found to be a function of Re, because of numerical instabilities affecting the code (see appendix A). Considering $Re_c = \sqrt{Ra}/Pr$, the minimum number of time steps needed to simulate a convective time unit resulted in the linear function of Pr ($\tau_c/\Delta t_{max} \sim Pr$). Figure 2.4 shows some examples of the actual number of time steps used to simulate a single convective time unit as a function of Pr. Simulations at $Pr = 10^3$ resulted almost 30 times costlier in terms of time with respect to

the diffusion of momentum. This could be confirmed by the increasing strength of the anomalous oscillations as Pr increases.

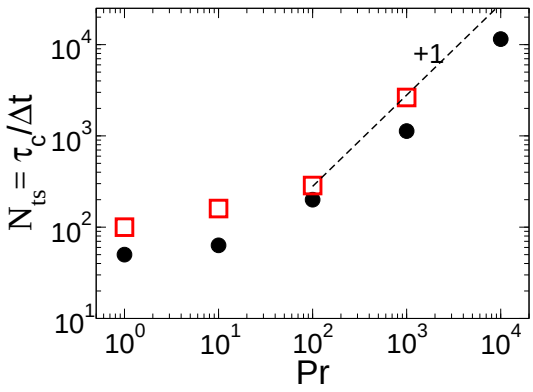

Figure 2.4: Actual number of time step needed to simulate a convective time unit $\tau_c = \tau\sqrt{Pr}$, where τ is the free-fall time. Circle: $Ra = 10^7$ and grid=$129 \times 31 \times 136$; square: $Ra = 10^8$ and grid=$385 \times 81 \times 321$.

those at $Pr = 1$.

The code, parallelized in the openMP paradigm, was run on multi-processor shared-memory computers. In particular the 8 simulations with grid $385\times81\times321$ (10 million points) were run on a NEC SF-6 machine in the CASPUR[14] centre for a total of 10^5 equivalent cpu hours (corresponding to 1360 days of wall-clock time). The others simulations were run on IBM-SP5 and IBM-CLX machines in the CINECA[15] centre. Around 5 terabytes of data have been produced and stored.

2.4.4 *Aposteriori* grid sizing checks

We show here how the data actually meet the grid sizing criteria introduced in section 2.4.1, which basically consist in setting the grid size of the same order of the Batchelor scale. The typical grid size is defined as

$$\Delta = (2\pi r \Delta\theta \Delta r \Delta z)^{1/3}, \tag{2.36}$$

where the lengths are considered non-dimensional with respect to the cell depth.

Table 2.2 shows the actual values of the thermal boundary layer thickness and of the Batchelor scale in comparison to the grid size for different Ra numbers and at $Pr = 10^3$. Figure 2.5 shows the Batchelor scale as a function of Pr for the higher Ra. For all the simulations, the Batchelor scale based on the total dissipation rate $\epsilon = \langle\varepsilon\rangle_{V,t}$ (viscous dissipation

[14]"Consorzio interuniversitario per le Applicazioni di Supercalcolo Per Università e Ricerca" located in Roma - www.caspur.it.
[15]High performance computing centre in Bologna - www.cineca.it.

Ra	Nu	$\delta_{T_{rms}}/h$	η_B/h	n_θ	n_r	n_z	Δ_{min}	Δ_{mean}	Δ_{max}	$N_{\delta_{T_{rms}}}$
10^5	3,47	0,1768	0,0450	109	18	70	0,0047	0,0111	0,0138	13
10^6	8,02	0,0617	0,0195	101	25	101	0,0028	0,0089	0,0122	10
$5\cdot10^6$	13,13	0,0410	0,0114	101	25	101	0,0028	0,0089	0,0122	7
10^7	16,23	0,0335	0,0090	129	31	136	0,0020	0,0069	0,0094	8
10^8	33,68	0,0164	0,0042	385	81	321	0,0005	0,0026	0,0037	12
10^9	66,58	0,0082	0,0020	385	81	321	0,0004	0,0025	0,0040	12

Table 2.2: *Aposteriori* check of the coarser grids used at $Pr = 10^3$. The thermal boundary layer thickness $\delta_{T_{rms}}$ is derived from the root mean square (rms) of the temperature profile. The Batchelor scale η_B is calculated using the total dissipation rate ϵ.

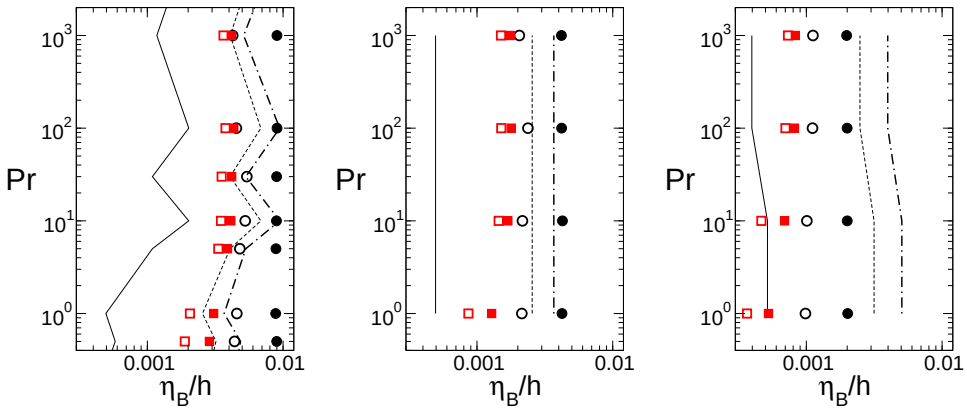

Figure 2.5: Batchelor scale as a function of Pr at (a) $Ra = 10^7$, (b) $Ra = 10^8$ and (c) $Ra = 10^9$. The Batchelor scale is calculated for different dissipation rate. Black filled circles: total dissipation rate ϵ; black unfilled circles: maximum value of the mean dissipation rate field $max\left[\langle\varepsilon\rangle_t\right]$; red filled squares: time averaged peak value of the dissipation rate $\langle max\left[\varepsilon\right]\rangle$; red unfilled squares:peak value of the dissipation rate $max\left[\varepsilon\right]$. The solid line represents Δ_{min}, the dashed line Δ_{mean} and the dot-dashed line Δ_{max}, where $\Delta = (2\pi r\Delta\theta\Delta r\Delta z)^{1/3}$ is the typical grid size.

rate field $\varepsilon = \varepsilon(\boldsymbol{x}, t)$ averaged on space and time) results to be equal or greater than the maximum grid size, except for simulations at $Ra = 10^9$. In this last case grids coarser than usual were used due to computational limitation; for them the Batchelor scale was nearly half of the maximum grid size (see table 2.2).

The Batchelor scale comes out to be independent with respect to Pr (see fig. 2.5), as foreseen for $Pr \geq 1$ in section 2.4.1. It is worth noting that the independence on Pr is basically still valid for other ways of defining the dissipation rate used to calculate the Batchelor scale. Even in the worst case of considering peak dissipation values, the same saturation is reached for Pr high enough. Moreover, the local minimum Batchelor scale increases with increasing Pr, suggesting more constraining conditions in terms of grid resolution at

$Pr \simeq 1$ instead of at higher Pr. This is in contradiction with the common expectation to have smaller and smaller temperature scales for increasing Pr, because the Peclet number is usually expected to increase with Pr ($Pe \sim \sqrt{RaPr}$), at least for $Pr \sim O(1)$. It has to be taken into account, however, that the Batchelor scale is based on the viscous dissipation rate $\varepsilon = 1/Re\,(\nabla \boldsymbol{u} : \nabla \boldsymbol{u})$, while the dissipation of the temperature field is, in fact, measured by the thermal dissipation rate $\varepsilon_T = 1/Pe\,(\nabla\Theta \cdot \nabla\Theta)$. In spite of the strong relationship between the mean values[16], the two dissipation fields do not seem to be locally connected. Indeed analyzing the three-dimensional time-dependent dissipation fields $\varepsilon(\boldsymbol{x}, t)$ and $\varepsilon_T(\boldsymbol{x}, t)$, it has been found that large value of ε are not necessarily connected to large value of ε_T. In particular, peaks of ε_T are localized close to the top and bottom plates, while peaks of ε are mainly sited close to the sidewall, where on the contrary ε_T results to be quite small[17]. An indication of the small local correspondence between ε and ε_T is given by the different shapes of their probability density functions (see fig. 2.6). This means that a local definition of the Batchelor scale is not useful for comparison with the local grid size. For this reason the data check is limited to global values, and typical grid sizes shown in figure 2.5 (continuous lines) are significant only with respect to the global Batchelor scale (filled circles). Nevertheless the data trends can give a qualitative indication on the correctness of the grid sizes adopted. Indeed if the dissipation scale linked to ϵ_T is really represented by the Batchelor scale and the results are independent of Pr, the smallest scales due to peaks of thermal dissipation increase their size with Pr until they reach a saturation. This behavior, qualitatively in agreement with that of the local Batchelor scales of figure 2.5, is shown in figure 2.6 through the probability density functions (pdf) of the thermal dissipation field at different Pr. The pdf, calculated on the whole volume and averaged on time, are performed with respect to normalized values $\xi = \varepsilon/\epsilon$ and $\xi_T = \varepsilon_T/\epsilon_T$. Figure 2.6 shows that the tail of $\langle p(\xi_T)\rangle_t$ is less pronounced as Pr increases, following a similar relative behavior of the tail of $\langle p(\xi)\rangle_t$ and indicating that actually high Pr simulations could have less constraining requirements of grid resolutions.

In summary, the data confirm that the Batchelor scale is independent of Pr, justifying the choice of using the same grid for increasing Pr. Besides, the thermal dissipation peaks become relatively less extreme as Pr increases and finally saturate. This behavior can allow

[16] In case of stationary solutions, the total dissipation rates ϵ and ϵ_T are analytically related to each other by

$$\epsilon = \frac{Ra}{RePe^2}\left[Pe \cdot \epsilon_T - 1\right]. \tag{2.37}$$

This relationship can be easily derived by combining eqs. (3.3) and (3.4).

[17] The local disconnectedness betweeen thermal and viscous dissipation rates could be not simply due to the strong anisotropy and to the presence of walls. Indeed similar findings have been made for passive scalar mixing in homogeneous and isotropic turbulent flows [66].

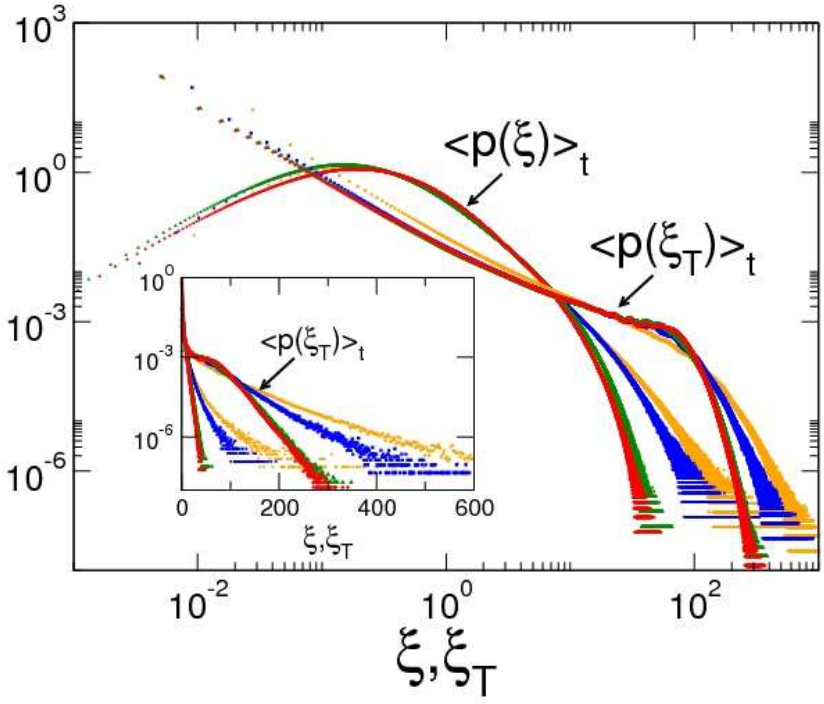

Figure 2.6: Probability density function (pdf) averaged on time and calculated on the whole volume of the dissipation rates normalized by the mean values. The pdf of viscous dissipation $\xi = \varepsilon/\epsilon$ and that of thermal dissipation $\xi = \varepsilon_T/\epsilon_T$ are calculated at $Ra = 10^9$ and varied Pr. Red $Pr = 10^3$; green $Pr = 10^2$; blue $Pr = 10^1$; orange $Pr = 10^0$. The inset shows the same with respect to a linear scale in the abscissa.

us to adopt less refined grids at higher Pr or to obtain better-resolved flow as Pr increases if the grid is kept constant with Pr.

These *aposteriori* checks have been necessary to verify the consistency of the data with the choices made *apriori* but are not sufficient to test the correctness of the results. Indeed if the simulations are not correctly resolved, the results can be wrong and therefore also the checks can be misleading. Moreover the grid sizing criteria are based on hypotheses of fully turbulent flow and a scalar-like behavior of the temperature field at least at dissipative scales. Both of these conditions are not matched in large part of the simulations. In addition, the size of the smaller scales is estimated using dimensional analysis, which might be numerical pre-factors changing their effective value. In this context the only reliable check is a grid refinement analysis that has been performed for several grid levels and at more than one Rayleigh number, with satisfactory results of convergence. For the simulations not directly involved in the grid refinement analysis, further indirect checks of the results have been done. The next chapter is dedicated to this additional step of data validation.

Chapter 3

Error analysis

3.1 Introduction

The errors estimation is a central issue of any experimental and numerical study. Indeed only the correct estimation of the errors allows a proper interpretation of results. The exact errors calculation is not easy with many sources of errors interacting each other in a non-trivial way. Our aim is, however, to obtain a reasonable estimation of them.

In a numerical experiment it is possible to identify three main sources of errors: the errors due to grid resolution in space and time; for fixed grid, the errors that are due to the precision of the numerical schemes used to simulate and to post-process the data; and the errors that directly influence the statistics of the problem, linked to the correct sampling of the data and to the duration and number of simulations.

If we compare the precision of numerical schemes with the sensitivity of laboratory instruments, the last two types of errors are in common with laboratory experiments. On the contrary, grid resolution errors are particular of numerical simulations. In the case of laboratory experiments, the flow under study is real. Instead, in numerical simulations, the flow is the result of discretized equations. To limit the resulting error, we deal with direct numerical simulations and highly refined grids. The only available way to investigate it is to refine the grids and compare the results with those from coarser grids.

All the errors considered are influenced by each other, and it is not easy then to exactly distinguish them. However, by a suitable averaging of the Boussinesq equations it is possible to derive some exact analytical relationships. Using them we check the results and estimate the error bars of some quantities. Then, we perform the grid refinement analysis verifying

that the results obtained with coarser grids are within the error bars of those of more refined grids. Where it is not possible to evaluate an error bar, we require (somewhat arbitrarily but reasonably) the difference between the coarse and the refined grids results to be less than 5%.

A distinction between statistical errors concerning short and long time series has to be done. The convective cell usually develops persistent characteristic large scale circulations of the flow depending on the cell size and shape, and on the values of Ra and Pr numbers. After quite a long time, these large scale circulations can change or reorient themselves ([51], [70]). Generally numerical simulations are not long enough to experience these kinds of changes. As a consequence, the statistics are calculated over a single circulation mode and not over all the possible modes, as should be done theoretically [49]. This can lead to discrepancies between experimental results and theoretical expectations. In our simulations we found some examples of multiple-circulation modes and estimated the differences of averaging on one or more modes.

3.2 Error checks and error bars

The numerical code, described in section 2.3, directly calculates the three-dimensional time-dependent fields of temperature (Θ), pressure (p) and velocity ($\boldsymbol{u}$). These fields are mainly affected by two kinds of errors. The first is due to the grid resolution in space and time. The sensitivity of the results to this kind of error is estimated through a grid refinement analysis (see section 3.3). The other kind of error is due to the precision of the particular code solving the problem with a fixed grid.

Unless different codes are available for comparing the results, the only way to verify the precision of a given code is indirect. The exact value of some quantities can be analytically derived. Comparing the quantities calculated from simulation data to the exact values, it is possible to check the errors affecting the data. For example, the velocity should be a divergence-free field ($\nabla \cdot \boldsymbol{u} = 0$). Then the divergence value can be monitored to indirectly verify the correctness of the velocity and pressure fields. (For all our simulations the divergence as a function of time is smaller than 10^{-8}.) From the divergence-free condition together with the no-slip condition on the walls, it is easy to derive that the volume average of each component of the velocity field must be zero at each time: $\langle u_j \rangle_V (t) = 0$ ($j = \theta, r, z$). More generally, the horizontal surface average of the vertical velocity must be zero ($\langle u_z \rangle_A (z,t) = 0$) and the vertical surface average of the radial velocity must be

zero ($\langle u_r \rangle_{\theta,z}(r,t) = 0$). The maximum values characterizing the vertical profiles of u_z and the horizontal profiles u_r for all the simulations are smaller than 10^{-5} if compared to the corresponding root-mean-square (rms) values.

The non-dimensional values of temperature field Θ must be within the interval $[0,1]$ and, in the presence of steady solutions, its volume average must be $1/2$ ($\langle \Theta \rangle_V = 1/2$). Further, the volume average of the vertical gradient of the non-dimensional pressure p must be $1/2$, while the volume average of the horizontal gradients of p must be zero: $\langle -\partial p/\partial z \rangle_V = 1/2$, $\langle -\partial p/(r\partial\theta) \rangle_V = \langle -\partial p/\partial r \rangle_V = 0$. These and many other simple analytical relationships can be directly derived from boundary conditions and Boussinesq equations.

Actually this kind of indirect controls mainly concerns averaged and filtered quantities of the original three-dimensional fields. The filtering operations introduce other errors and modify the previous ones. However, after the cross-checking of many of these results, we are confident that the errors due to the precision of the main code are negligible with respect to the grid resolutions errors.

The errors can grow in the post-process phase. The post-process operations include all kinds of manipulations applied to the temperature, pressure and velocity fields both to derive other three-dimensional fields (dissipation, heat flux, vorticity) and to filter the data (averages, rms, power spectra). The errors due to the numerical schemes used to post-process the data have been checked by implementing different numerical methods and comparing the results with each other.

The derivative operations generally decrease the precision of the data. As a consequence, the errors affecting derived fields increase. These fields have been found quite sensitive to the kind of derivative scheme used close to the boundaries. Special care has been used in the treatment of boundary conditions. Even for these fields, indirect checks have been done. For example, by definition, the non-dimensional diffusive heat flux in the vertical direction should be equal to one at each time if averaged on the vertical direction: $\langle -\partial\Theta/\partial z \rangle_z(\theta,r,t) = 1$. (The worst case with respect to all the simulations shows a typical discrepancy of the order of 10^{-4}).

To proceed, another type of error has to be considered, this being most relevant to the quantities of interest averaged on time. The relationships used above for steady solutions are still valid for statistically steady solutions obtained by adding a time average process to the space averaging. In this case, however, the scenario becomes more complex because we add statistical errors to precision errors. Unsteady solutions indeed can be affected also by errors which derive from the sampling of the data and from the duration of the simulations. To

limit this kind of errors it is essential to record statistically-significant samples. In particular, to calculate correct mean and high-order moment values[1], it is necessary to reach stationary conditions and perform simulations for a time much longer than the typical integral time scale in order to obtain a great number of statistically independent samples, since the relative error affecting the probability density function of time signals is inversely proportional to the number of statistically independent samples [72]. To obtain all statistically independent samples the data should be recorded approximately once every two integral scales [72].

Most of the quantities taken into account in the present work are mainly driven by convective dynamics characterized by the typical time scale τ_c introduced in section 2.4.3. As a consequence the integral scale was estimated to be of the order of τ_c and the unsteady simulations were run to obtain at least 100 independent samples. The results of the simulations have been extensively checked by comparing them to those obtained with a much higher number of independent samples.

The relative influence of statistical errors for all the quantities shown in this work have been found to be generally negligible with respect to the relative influence of the grid resolution errors (much less than 1% with respect to relative grid resolution errors, which are generally of the order of $1\% - 5\%$). There is, however, a warning situation relative to quantities driven by dynamics much slower than the convective ones, for which the integral time scale is much higher than τ_c. An example is the volume averaged temperature signal shown in figure 2.3. In these cases the collected samples could not be statistically representative. The details of this respect are discussed in section 3.4. In this context the analysis is limited to the faster dynamics with respect to which a high degree of convergence is reached for the most important quantities of all the simulations.

It is important to note that there is not possible to separate the errors based on the different sources The only possibility is to assess their relative influence on the results, as done for statistical errors and as will be done for grid resolution errors in section 3.3. Besides, it is not possible to calculate an absolute value of the global error affecting the data, unless we know the exact solution. This happens only for very few quantities, most of them already described above and used to check the results. The subsequent checks do not involve exact solutions but analytically exact relationships between some quantities that will allow a relative estimation of the global error.

The most important relationships obtained by averaging the Boussinesq equations are those involving the Nusselt number. It follows from the energy equation that the time-

[1]Note that in this discussion concerns errors measured for fixed grid (in space and time). The influence of the grid resolution, generally very high on the high-order moments, is discussed in section 3.3.

averaged heat flux in the vertical direction must be constant across each horizontal section A (i.e. the heat flux profile in the vertical direction must be constant). This constant value in the non-dimensional form is the Nusselt number

$$Nu_A = \left\langle -\frac{\partial \Theta}{\partial z} + Pe \cdot \Theta u_z \right\rangle_{A,t} = -\frac{\partial \langle \Theta \rangle_{A,t}}{\partial z} + Pe \langle \Theta u_z \rangle_{A,t} . \tag{3.1}$$

Integrating Nu_A in the vertical direction it is possible to derive a slightly different definition of the Nusselt number, which we call "bulk Nusselt number":

$$Nu_V = \langle Nu_A \rangle_z = 1 + Pe \langle \Theta u_z \rangle_{V,t} \tag{3.2}$$

Given that Nu_A is a constant, the bulk Nu_V is equal to Nu_A and we refer to them indifferently as Nu.

The Nusselt number is also related to the total viscous dissipation rate $\epsilon = 1/Re \langle \nabla \boldsymbol{u} : \nabla \boldsymbol{u} \rangle$ and to the total thermal dissipation rate $\epsilon_T = 1/Pe \langle \nabla \Theta : \nabla \Theta \rangle$ as follows[2]:

$$Nu = \frac{RePe^2}{Ra} \cdot \epsilon + 1 \tag{3.3}$$

$$Nu = Pe \cdot \epsilon_T \tag{3.4}$$

The Nu numbers calculated using these different expressions should have the same value, then it is possible to have an estimation of the error that, fixed the grid size, affects the Nu number. In particular, we calculate the Nu number as the mean value obtained averaging the results of 3.1 on each horizontal section, of 3.2 and of 3.3. The error bar is taken as the difference between the maximum and the minimum value[3] of those results. This way of estimating the error bar is quite stringent, not only because the maximum error[4] is considered, but even because derivative fields are involved in the evaluation. In particular,

[2]The relationships (3.3) and (3.4) can be easily derived by averaging over the volume the stationary version of the kinetic energy equation and of the kinetic-energy-like temperature equation. The last equation is the temperature equation multiplied by temperature itself. The result has to be combined to the Nu number definition (3.2) in the case of viscous dissipation and to the Nu definition (3.1) for the thermal dissipation.

[3]Usually in numerical works the Nu error bar is considered equal to the standard deviation of the Nu number profile in the vertical direction (average over time and horizontal planes) [28] or to the root-mean-square of the Nu number signal in time (average over the whole volume) [78]. In the first case the error is basically due to the primitive fields of temperature and vertical velocity and to the derivative of the temperature close to the horizontal walls, since the conductive term is negligible in the bulk. According to this criterion, the typical Nu error bar of our simulations results less than 1%. The second case is not applicable to steady solutions, showing that it does not really represent an error, but physical oscillations around a mean value with its strength depending on the characteristics of the flow. It can be used to show the typical variability of Nu, but not as a check of the results. Obviously this variability should be larger than the error to have a physical meaning.

[4]The error bar estimation proposed in this work is taken as the maximum difference instead of the standard deviation of the entries, because the sample is not composed by statistical occurrences.

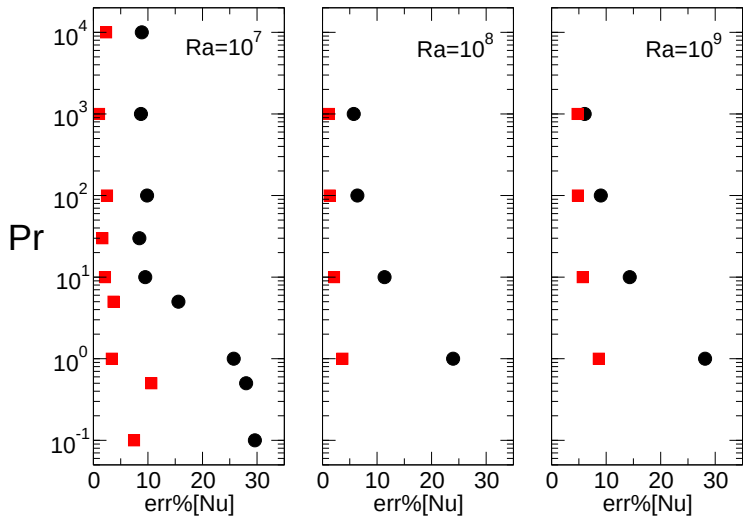

Figure 3.1: Errors in the Nusselt number in percentage (red squares) with respect to the Nu mean value compared to the bulk Nusselt rms (black circles) for different values of Pr and Ra.

through the relationships (3.3), the viscous and thermal dissipation fields play a fundamental role in the determination of the Nu error bar as it is defined. Therefore, smaller values of these error bars correspond to a higher precision in the calculation of dissipation fields[5].

Figure 3.1 shows the error bar on Nu for the main series of data compared to corresponding rms of the bulk Nu signal. The most critical simulations are at $Ra = 10^7$ and $Pr < 1$ and at $Ra = 10^9$. The error bar in those cases exceed 3% of Nu mean values. However, at $Ra = 10^9$, the error bar is less than or equal to 5% except at $Pr = 1$. The simulations not shown in figure 3.1 have a relative error of smaller than 3%; in particular, for steady simulations the error percentage goes below 1%.

Other quantities that can be checked are boundary layers. Under Boussinesq approximation and in stationary conditions, the top and bottom boundary layer thicknesses should converge to the same value. All the viscous and thermal boundary layer definitions used in this work have been checked with respect to this requirement, and a relative discrepancy of smaller than 1% has been found; for a few critical simulations a difference between top and bottom values smaller than 3%.

A further check is possible for the thermal boundary layer thickness δ_T defined as the

[5]This way of checking the results was already used in [78] and [17].

depth where the tangent to the temperature profile at the top or bottom plate crosses the mean temperature $\langle\Theta\rangle_{V,t} = 1/2$:

$$\delta_T \triangleq \frac{1}{2\frac{d\langle\Theta\rangle_{A,t}}{dz}|_{z=0,1}}. \tag{3.5}$$

Considering the definition (3.1) for the Nusselt number, the thermal boundary layer δ_T is strictly related to the Nu number as

$$\delta_T = \frac{1}{2Nu}. \tag{3.6}$$

Comparing the δ_T values for all the simulations, calculated by (3.2) and (3.2), discrepancies smaller than 1% have been found.

It was not possible to check all the quantities involved in this study, especially the local quantities. The only way would be to apply a grid refinement analysis to all the simulations. Due to practical limitations, a grid refinement study was possible only for a smaller number of simulations, involving, however, a large range of Ra and Pr numbers. The details are given in the next section.

3.3 Grid refinement analysis

In order to assess the grid independence of the solutions, a grid refinement analysis has been extensively applied (see fig. 2.1). In particular the results obtained with the coarser grids have been compared to those obtained with the corresponding refined grids. Mean, rms and maximum values of velocities, temperature, heat fluxes and dissipation rates computed with respect to volume and or time have been analyzed.

For the reference simulations at $Ra < 10^7$, it has been found that all the quantities considered differ by less than 3%, between coarse and refined grids.

The most critical simulations are however at higher Ra, where four reference simulations have been performed: at $Ra = 10^7$ and $Pr = 10^0, 10^3$ and at $Ra = 10^8$ and $Pr = 10^1, 10^2$. In these cases differences smaller than 3% have been found for all the mean values, the time-averaged peaks of the velocity components, and almost all the rms values. Larger discrepancies concern the mean values of the fluctuating thermal and viscous dissipation rates at $Ra = 10^7$ and, for $Pr = 10^3$, the rms value of the Nu signal. For these cases the relative error is of order of 5%. Differences higher than 10% occur in simulations at $Ra = 10^7$ for time-averaged peak values of the dissipation rates. The simulations at $Ra = 10^8$ show

Ra	Pr	n_θ	n_r	n_z	Nu_V	$rms\,[Nu_V]$
10^7	10^0	129	31	136	17,620	4,593
		385	81	321	17,639	4,531
10^7	10^3	129	31	136	16,264	1,461
		217	55	217	16,227	1,415
10^8	10^1	217	75	301	31,594	3,561
		385	81	321	31,507	3,584
10^8	10^2	217	75	301	33,408	2,164
		385	81	321	33,240	2,127

Table 3.1: Grid sensitivity of the bulk Nusselt number defined by (3.2). The rms value is calculated with respect to the time signal.

satisfactory results of convergence even for these quantities (errors smaller than 5%). Table 3.1 summarizes the grids involved in this analysis and shows the values of the Nusselt number calculated through definition (3.2) and the rms values corresponding to its signal as a function of time. A further test has been performed comparing the probability density function (pdf) of the viscous and thermal dissipation rates calculated on the whole volume and averaged on time. Indeed, since the dissipation rates are directly related to the smaller scales of the problem, a grid can be regarded as well sized if it correctly resolves these quantities. Figure 3.2 shows that for different values of Ra and Pr there is a satisfactory agreement of results obtained from the grid pairs. For $Ra = 10^7$ and $Pr = 10^1$ (see fig. 3.2(a)) the smaller grid slightly under-resolves the flow, as seen in the small discrepancy of the curves. This result is unexpected taking into account that the refined grid has a number of points more than 18 times larger than the coarse grid. Note that at higher Pr the same coarse grid gives good results compared to a grid with a number of point almost 5 times larger. This is an indication that the smaller scales, including temperature scales, can be solved at higher Pr by the grid sized for $Pr = 1$. At $Ra = 10^8$ (plots 3.2(c) and 3.2(d)) bigger discrepancies occur relative to the kink of the thermal dissipation pdf. In these cases, however, the causes are not only the grid resolution but also a statistical deficiency, since the simulations performed with the coarser grid much are shorter that those using the more refined grid. It has been checked that the oscillations near the kink increase their strength when the time average is performed on a smaller set of data.

In conclusion, a grid refinement analysis has been applied to several simulations, checking all the quantities involved in this work and also the pdf of dissipation rates. Satisfactory results have been generally found. In particular, first and second order moments of the primitive fields and first-order moments of the derivative fields have been solved with good

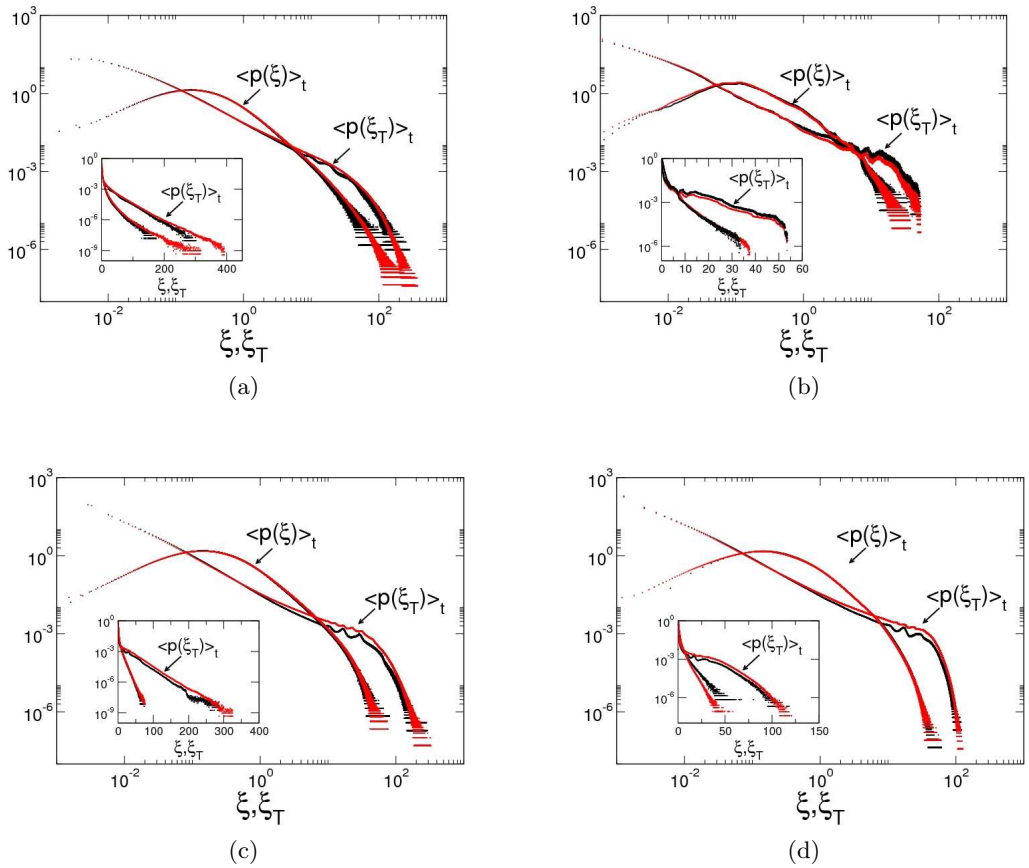

Figure 3.2: Examples of probability density functions (pdf) of the energy dissipation rate and of the temperature dissipation rate computed with respect to the whole volume and averaged over time, for coarse and refined grids (see table 3.1). The viscous and the thermal dissipation rates are normalized with respect to the mean values: $\xi = \varepsilon/\epsilon$ and $\xi = \varepsilon_T/\epsilon_T$. The black lines represent the coarser grids and the red lines the more refined ones. The inset shows the same quantities with respect to a linear scale in the abscissa. (a) $Ra = 10^7$ and $Pr = 10^0$; (b) $Ra = 10^7$ and $Pr = 10^3$; (c) $Ra = 10^8$ and $Pr = 10^1$; (d) $Ra = 10^8$ and $Pr = 10^2$.

accuracy (less than 3% of sensitivity to the grid). Second-order moments of the derivative fields have been found in some cases to be slightly less precise, but with a sensitivity to the grid of less than 5%. Where available, the simulations with the most refined grids will be used in the analysis of results.

3.4 Long time errors and multiple flow structures

The main dynamics of the problem develop on the convective time scale, which is the typical scale of large flow circulation and plume detachment. Long-time phenomena, however, appear in some simulations, as already mentioned in section 2.4.3. In particular, the volume-averaged temperature signal shows anomalous variations on a time scale much longer than the convective time scale at $Ra = 10^8$ and increasing Pr (see fig. 2.3).

At $Pr = 10^3$ and $Ra = 10^8$ the long-time variations in the volume-averaged temperature signal are more pronounced, while the oscillations at the convective time scale are negligible. In this case, analyzing the time evolution of flow, we found more than one large scale circulation structure[6] which remains almost unchanged for long time windows.

Figure 3.3 shows, for $Pr = 10^3$ and $Ra = 10^8$, the volume-averaged temperature and the bulk Nu number signals roughly divided into four time-windows, and the corresponding typical temperature maps. Neglecting the first interval that can be considered a transient, the volume-averaged temperature is almost constant in the second time interval. During this interval the flow is stably self-organized in a two-cell structure (fig. 3.3(a)). In the next interval the flow shows a more unstable behavior, during which a three-cell structure prevails (fig. 3.3(b)). In the last interval the flow evolves in a four-cell structure[7] (fig. 3.3(c)) which is quite stable in time.

The transition from one structure to another seems to have a correspondence with the slope of the volume-averaged temperature signal, since the large-scale circulation structures are quite stable when the signal is flat and unstable when it is steep. However, this does not mean that the transition from one structure to another necessarily implies a variation in the volume-averaged temperature. The unstable behavior of large-scale circulations is also visible in the Nu number signal (see fig. 3.3).

Variations of the volume-averaged temperature signal with respect to the mean value of 1/2 are due to a breaking of symmetry in the temperature profile (obtained by averaging

[6] More details on the flow structures can be found in chapter 5.

[7] The four-cell structure is more complex than as it appears in fig. 3.3(c), since a four-cell structure actually is visible only close to the bottom plate. At the top plate the structure is uni-cell. See figs. 5.3(c) and 5.3(f) in sec. 5.2.

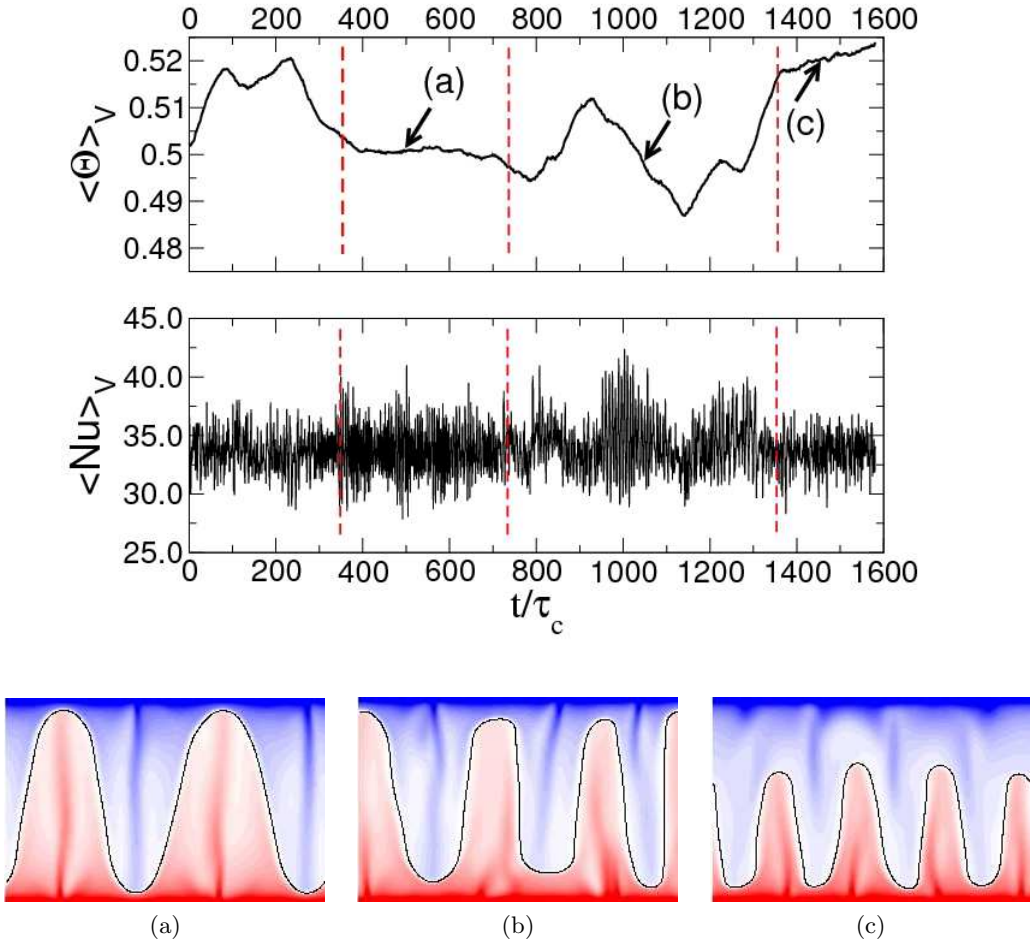

Figure 3.3: Volume-averaged temperature and Nu signals at $Ra = 10^8$ and $Pr = 10^3$ and corresponding multiple flow structures. The time is made non-dimensional using the convective time scale $\tau_c = U\sqrt{Pr}$ introduced in section 2.4.2 (U is the free-fall velocity; see also chapter 4). The plots at the bottom show the temperature map at the sidewall of snapshots in instants corresponding to the arrows of the top plot. The cylindrical sidewall is unrolled with respect to the azimuthal direction obtaining two-dimensional plots. Black solid lines represent mean temperature iso-lines ($\Theta(\boldsymbol{x}; t_s) = 1/2$).

the temperature field over horizontal planes).

In spite of the symmetry properties of the domain, large-scale flow structures strongly break these symmetries. In order to restore them, different large scale flow structures are expected if a simulation is performed for a sufficiently long time. Indeed, if the system is ergodic[8], a single simulation in theory should be able to cover all of its possible states within a finite time [49]. In practice, to witness a transition to different large scale structures during a single run is uncommon, because the characteristic times involved in this phenomenon are very challenging to simulate. The few examples come mainly from experiments ([51], [70]).

However, even if the large scale circulations strongly break 3D symmetries, their profiles, averaged over horizontal area, generally show a faster resurgence of the middle-plane symmetry, when averaged over a "short-time" window[9] (typically the same necessary to well define a stationary large-scale circulation structure). This means that stationary large-scale circulation structures (mean flow structures) usually have symmetric area-averaged profiles.

The reason of this "fast" convergence to symmetric profiles, apart from a dimensional reduction (3D to 1D), can be ascribed to the degree of turbulence characterizing the flow structures. At lower Pr (higher Re) the flow fluctuations are comparable to the typical mean flow values. The resulting vertical profiles instantaneously break the vertical symmetry, but show a good convergence on the average.

At higher Pr (lower Re) the flow fluctuations become negligible with respect to the mean values. The large structures are quite fixed in time, and the corresponding vertical profiles, when symmetric, remain so as well. If these structures destabilize, the recovery of the symmetry can be a long process according to the high "inertia" shown by the flow, which is due to the prevailing diffusive dynamics of momentum with respect to advection. The unexpected result is that, at $Ra = 10^8$ and $Pr = 10^3$, at least one stable well-defined large-scale structure (four-cell structure) seems to be allowed with non-symmetric profiles (see fig. 3.4). We have found no explanation to this observation[10]. However, longer simulations would be necessary to correctly investigate these long-term phenomena.

We furthermore point out the higher propensity of high Pr flows to show multiple large-scale structures with respect to flows at $Pr \sim 1$. We found this behavior also in other simulations close to the transition from steady to unsteady flows (see sec. 5.2).

In these cases, we have verified the influence of these multiple structures on the main

[8] The ergodicity is a common assumption in turbulence and in general in fluid dynamics [49]. Its relevance has, however, not been established.

[9] "Short" with respect to corresponding long-term phenomena.

[10] Presumably this phenomenon is due to the unbalancing between the momentum dynamics (low Re) and the temperature dynamics (high Pe) characterizing high-Pr flows.

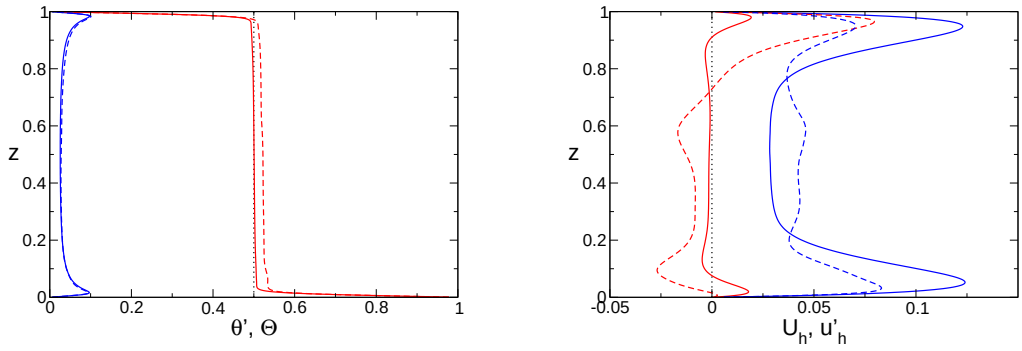

(a) (b)

Figure 3.4: Area-averaged vertical profiles of two-cell structure (solid lines) and four-cell structure (dashed lines) at $Ra = 10^8$ and $Pr = 10^3$. (a) Temperature profiles (red lines), and temperature rms profiles (blue lines). (b) Horizontal velocity profiles (red lines), and horizontal velocity rms profiles (blue lines).

quantities of interest, and in particular on the global Nu. This represent an important issue, because the presence of different structures is often assumed to justify some scatter behavior in data trends [59].

At $Ra = 10^8$ and $Pr = 10^3$ we have not found appreciable differences in the thermal boundary layer thicknesses and in the global Nusselt numbers, when calculated by averaging on the sub-time-windows shown in fig. 3.3 with respect to a time-average over all the simulated time interval. The discrepancies are less than 2% (inside the error-bars).

This result is visible in fig. 3.4(a), where the temperature profiles of the two-cell structure (solid lines) and of the four-cell structure (dashed lines) are compared. Even if the four-cell temperature profile is shifted with respect to that of the two-cell structure by around[11] 5%, its slope approaching the top and bottom plates are basically the same as those of the two-cell structure temperature profiles. This implies that the Nusselt number has to be the same. Note that the temperature rms profiles of the two different structures are almost the same.

Instead, in the case of horizontal velocity and viscous boundary layer, the results show much higher discrepancies, since the velocity profiles of the four-cell structure highly break the middle-plane symmetry (fig. 3.4(b)). In this structure the viscous boundary layer thicknesses differ between the top and bottom plates and with respect to the two-cell structure by more than 20%.

[11] A shift with respect to the central value of 1/2 by 5% is high if compared to the usual error of convergence concerning the total mean temperature. In our simulations this error is less than 0.2%. A discrepancy of 5% is comparable to that of some non-Boussinesq effects ([48],[13], [61], [62]).

In the other simulations showing multiple solutions, the highest errors concerning the Nusselt number and the other main quantities are less than 5%.

As a conclusion, in the presence of multiple structures no appreciable difference, able to significantly affect the Nu trends, has been found.

In the next chapters, for the simulation at $Ra = 10^8$ and $Pr = 10^3$, we will generally use the two-cell structure results.

Chapter 4

The non-dimensional form for large Pr

4.1 Introduction

In contrast to the pressure-driven flows, the Reynolds number in thermal convection is an output of the problem reflecting the strength of the flow. For Pr of the order of unity, the typical large-scale velocities of the flow are scaled well by the free fall velocity $U = \sqrt{g\alpha\Delta T h}$ [51] which results from the balance between the inertial and buoyancy terms of the momentum equation. For high Prandtl numbers, however, the momentum tends to be very diffusive and inertial forces become small; accordingly, the present simulations at high Pr showed that U does not represent the typical velocity of the large scale structure. By scaling the results of some simulations we have found that the large-scale characteristic velocity is $V = U/\sqrt{Pr}$, which yields a new non-dimensional form of the Boussinesq equations. The corresponding estimate of the Reynolds number is $Re = Vh/\nu = \sqrt{Ra}/Pr$. As a consequence, the Peclet number becomes $Pe = Vh/\kappa = \sqrt{Ra}$ independent of Pr. To verify the reliability of these estimates the results of all the performed simulations have been analyzed. In particular, the data trends of several velocities that can be assumed as typical of large structures have been considered.

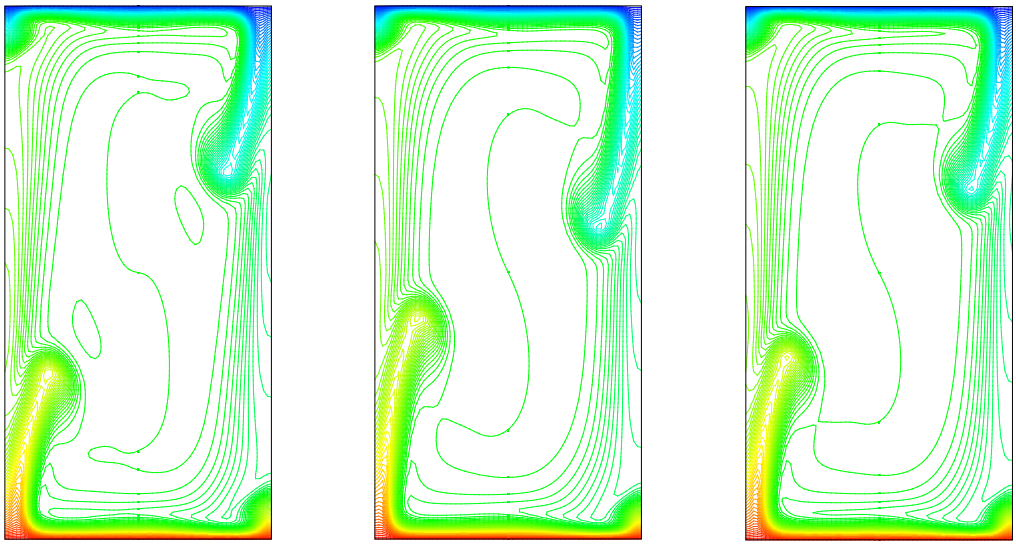

(a) (b) (c)

Figure 4.1: Isothermal lines of instantaneous temperature fields at $Ra = 10^7$ and (a) $Pr = 10^2$, (b) $Pr = 10^3$, (c) $Pr = 10^4$

4.2 Non-dimensional form of equations

Considerations started from the analysis of simulations at fixed $Ra = 10^7$ and varying Pr from 1 to 10^4. Plotting the instantaneous three-dimensional temperature and velocity fields, we found that the various simulations at $Pr \geq 10^2$ have a very similar profiles of temperature (see fig. 4.1) and velocity fields. In particular, the temperature and pressure[1] (fig. 4.2) fields result to be quite constant with increasing Pr, while the velocity field may vary of several orders of magnitude in strength but maintaining the same shape. It is worth noting that this similarity is at each time step, not only on average.

Practically, if temperature Θ_1, velocity $\mathbf{u}_1$ and pressure p_1 are the fields solved at $Pr = Pr_1 \geq 100$, and Θ_2, $\mathbf{u}_2$, p_2 those at $Pr = Pr_2 \geq 100 \neq Pr_1$, the simulations show that $\Theta_2 \backsimeq \Theta_1$, $p_2 \backsimeq p_1$ and $\mathbf{u}_2 \backsimeq a \cdot \mathbf{u}_1$, where a is a constant to be determined. All these quantities are solutions of the non-dimensional Boussinesq equations (2.1) introduced in section 2.2. We remember that eqs. (2.1) have been made non-dimensional using the free-fall velocity $U = \sqrt{g\alpha\Delta T h}$, the distance between hot and cold plates h and their temperature difference $\Delta T = T_h - T_c$.

Thus, if Θ_1, $\mathbf{u}_1$, p_1 are solution of (2.1), then $\Theta_2 = \Theta_1$, $\mathbf{u}_2 = a \cdot \mathbf{u}_1$ and $p_2 = p_1$ are

[1] Actually the pressure gradient should be considered instead of pressure, because the pressure is defined unless a "constant" (a function of time). Thus, the pressure value can generally change from one solution to another. Since in the present case the pressure "accidentally" shows a similar behavior in different simulations, for simplicity we consider the pressure instead of the pressure gradient.

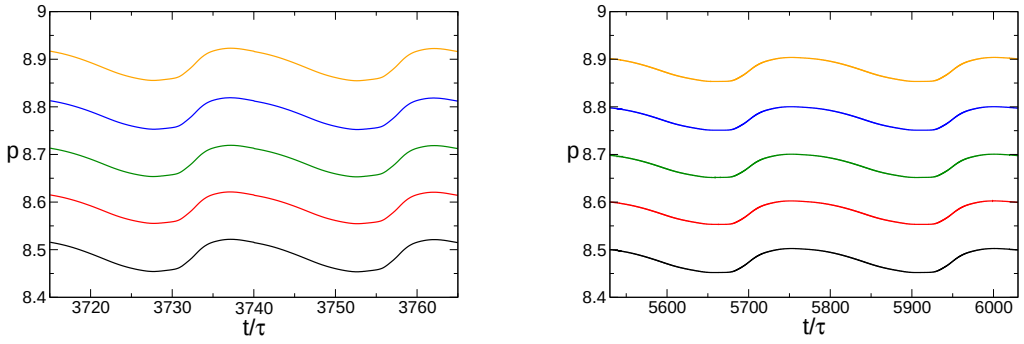

(a) (b)

Figure 4.2: Pressure signals at different points along the axis the cell for (a) $Pr = 10^2$ and (b) $Pr = 10^4$. From below to above: $z = 0.1$, $z = 0.3$, $z = 0.5$, $z = 0.7$, $z = 0.9$. The typical time τ is equal to the free-fall time. (Simulations at $Ra = 10^7$).

also solution of (2.1) only if $t_2 = t_1/a$, $Ra_2 = Ra_1$, $a = \sqrt{Pr_1/Pr_2}$ and the advective term $D\boldsymbol{u}/Dt$ of the momentum equation is equal to zero. These conditions are easy to derive putting Θ_1, $\mathbf{u}_1$, p_1 and Θ_2, $\mathbf{u}_2$, p_2 in (2.1) and comparing the equations.

This result shows some interesting features: at $Ra = 10^7$ and $Pr \geq 100$ the advective term $D\boldsymbol{u}/Dt$ is quite negligible and the solutions are close to infinite Pr solution. This means that the infinite Pr limit start to hold at relatively "small" Pr with respect to that expected[2].

The condition $t_2 = t_1/a$ tells that the time scale τ is related to the velocity through $\tau = h/U$ and is not independent of the velocity as it sometimes happens in Stokes wavy flows. The condition $Ra_2 = Ra_1$ indicates that this kind of similarity is possible only at fixed Rayleigh numbers. The condition $a = \sqrt{Pr_1/Pr_2}$ suggests the proper way to make the equations non-dimensional.

In fact, it is possible to define a new non-dimensional velocity as $\boldsymbol{v} = \sqrt{Pr}\,\boldsymbol{u}$ such that $\boldsymbol{v}_1 = \sqrt{Pr_1}\boldsymbol{u}_1 = \sqrt{Pr_2}\boldsymbol{u}_2 = \boldsymbol{v}_2$. As a consequence, the characteristic velocity will be $V = U/\sqrt{Pr}$, where U is the free-fall velocity. Using V instead of U to make the equations non-dimensional, equations (2.1) are changed to:

$$\begin{aligned} &\frac{1}{Pr}\frac{D\boldsymbol{v}}{D\mathfrak{t}} = -\nabla p + \Theta\hat{\boldsymbol{k}} + \frac{1}{\sqrt{Ra}}\nabla^2\boldsymbol{v}, \qquad \nabla\cdot\boldsymbol{v} = 0, \\ &\frac{D\Theta}{D\mathfrak{t}} = \frac{1}{\sqrt{Ra}}\nabla^2\Theta. \end{aligned} \tag{4.1}$$

[2]In analytical studies on the heat transport bounds, solutions at large Pr have be found in agreement with those of the infinite Pr number model under the condition $Pr > cRa$, where c is a constant of order unity ([80]).

Non-dimensional temperature and pressure in (4.1) are the same as in (2.1), while non-dimensional velocity $\boldsymbol{v}$ and time $\mathfrak{t}$ differ respectively from $\boldsymbol{u}$ and t. Note that for $Pr = 1$ the equations (2.1) and (4.1) are the same.

With respect to this non-dimensional form (4.1), we obtain that all the non-dimensional fields are very similar to each other for simulations at large enough Pr. They tend to a common configuration as the advective term $\frac{1}{Pr}\frac{D\boldsymbol{v}}{D\mathfrak{t}}$ becomes smaller. In practice, this happens for $Pr \geq 100$.

Given that the characteristic velocity of the form (4.1) is differently defined from that of form (2.1), the Reynolds number is different. Indeed for (4.1) it is $Re = \sqrt{Ra}/Pr$, which means a stronger inverse dependence of Re on Pr when compared to the previous form (2.1). The stronger dependence can better explain the fast convergence to infinite Pr solution. Peclet number also changes to $Pe = \sqrt{Ra}$, independent of Pr.

Note that any different way of making the equations non-dimensional leads to a different dependence of Re and Pe from Ra and Pr. In particular, there are two more common non-dimensional forms with respect to (4.1) that can also be used instead of form (2.1) and that, at fixed $Ra = 10^7$, are consistent with the similarity of solutions at $Pr \geq 100$.

One non-dimensional form, largely used in theoretical work, is that in which the characteristic velocity $\hat{U}$ is obtained by comparing the advective and the diffusive term of temperature equation ($\hat{U} = \kappa/h$):

$$\begin{aligned} &\frac{1}{RaPr}\frac{D\hat{\boldsymbol{u}}}{D\hat{t}} = -\nabla p + \Theta\hat{\boldsymbol{k}} + \frac{1}{Ra}\nabla^2\hat{\boldsymbol{u}}, \qquad \nabla\cdot\hat{\boldsymbol{u}} = 0, \\ &\frac{D\Theta}{D\hat{t}} = \nabla^2\Theta, \end{aligned} \tag{4.2}$$

For this form, one obtains $Re = 1/Pr$ and $Pe = 1$, both independent[3] of Ra.

Another common way to make the equations non-dimensional at high-Pr regimes is to use the characteristic velocity $\tilde{U} = \alpha g \Delta T h^2/\nu = Ra(\kappa/h)$, which appears by comparing the buoyancy term to the diffusive term of momentum equation:

$$\begin{aligned} &\frac{Ra}{Pr}\frac{D\tilde{\boldsymbol{u}}}{D\tilde{t}} = -\nabla p + \Theta\hat{\boldsymbol{k}} + \nabla^2\tilde{\boldsymbol{u}}, \qquad \nabla\cdot\tilde{\boldsymbol{u}} = 0, \\ &\frac{D\Theta}{D\tilde{t}} = \frac{1}{Ra}\nabla^2\Theta, \end{aligned} \tag{4.3}$$

In this case we have $Re = Ra/Pr$ and $Pe = Ra$.

[3]In fact this non-dimensional form is slightly different from the pure "classical" one just because the temperature scale is kept equal to the temperature difference ΔT across the layer of fluid and not equal to $\nu\kappa/\alpha g h^3$ as in the "original" version [9]. However no difference on Re and Pe number dependencies exists between the two versions.

All four non-dimensional forms (2.1), (4.1), (4.2) and (4.3) are based on the same length scale h, the same temperature scale ΔT and the same pressure scale $\Pi = \rho\alpha g\Delta T h$. The only differences are on the velocity scales and, as a consequence, on the time scales. This means that non-dimensional length $\mathbf{x}$, temperature Θ, pressure p are the same for all the forms. Non-dimensional velocity $\mathbf{v}$ of form (4.1) is linked to that of form (2.1) through $\mathbf{v} = \sqrt{Pr}\,\mathbf{u}$. For form (4.2) with respect to form (2.1), we have $\hat{\mathbf{u}} = \sqrt{RaPr}\,\mathbf{u}$. And $\tilde{\mathbf{u}} = \sqrt{Pr/Ra}\,\mathbf{u}$ for form (4.3) with respect to form (2.1). Note that all the last three non-dimensional forms include the dependence on $\sqrt{Pr}$ inside their non-dimensional velocity.

At this point the question is: what is the correct non-dimensional form of the equations?

If we assume that the global quantities of our problem can be correctly described by a single length scale and given that the forcing quantity in the problem is the temperature difference imposed to the layer of fluid, it is quite reasonable to consider the height of cell h as the characteristic length and the temperature ΔT as the characteristic temperature. Moreover, since the buoyancy force is the cause of the motion and the pressure simply adapts itself to globally balance the buoyancy effect, it is also reasonable to take the pressure term of the same order of the buoyancy term. If this setting is correct, the only open issue is the choice of the characteristic velocity.

4.3 Characteristic velocity

In the incompressible non-convective flows, the characteristic velocity U is generally an imposed quantity (such as the temperature difference ΔT in our problem of thermal convection). Calling $\mathbf{u}^*$ the dimensional velocity, the relative non-dimensional velocity $\mathbf{u} = \mathbf{u}^*/U$ is usually quite constant and of order one in its typical values. Following the same idea, a way to choose the characteristic velocity in thermal convection case is to set U such that the corresponding non-dimensional velocity is quite constant and typical of order one. In other words, U should be set in such a way that typical values of the non-dimensional velocity $\mathbf{u}$ are independent of Ra and Pr.

Applying this criterion to the simulations data, it is possible to decide the best non-dimensional form of Boussinesq equations among those previously proposed. Considering, for example, the time-averaged peak vertical velocity as typical, fig. 4.3 shows the four non-dimensional versions of this velocity as a function of Pr and for various Ra numbers. This figure shows that in (2.1) the non-dimensional peak vertical velocity strongly depends on Pr (fig. 4.3(a)). Instead, for the other three non-dimensional forms the dependence on Pr is

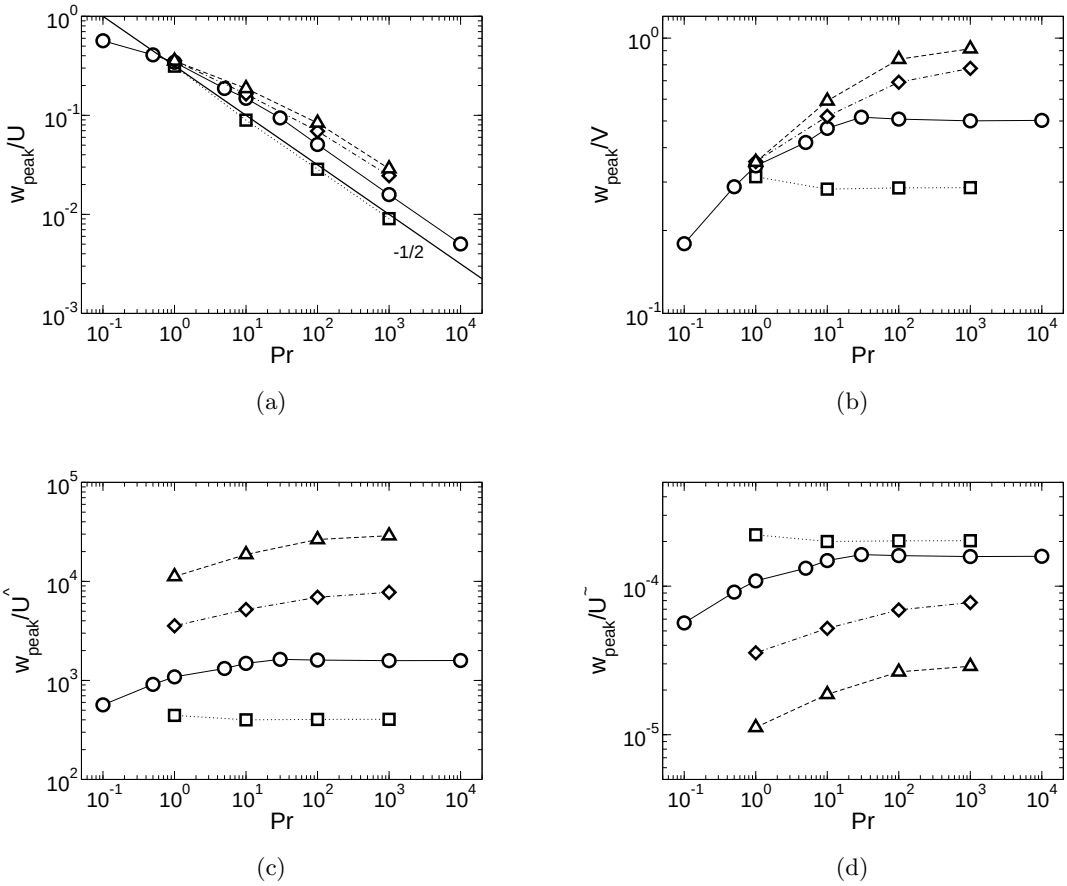

Figure 4.3: Non-dimensional time-average peak vertical velocity as function of Pr. It is $w_{peak} = \langle max\,[u_z] \rangle_t$ and: (a) $U = \sqrt{\alpha g \Delta T h}$ (form (2.1)), (b) $V = \sqrt{\alpha g \Delta T h / Pr}$ (form (4.1)), (c) $\hat{U} = \kappa / h$ (form (4.2)) and (d) $\tilde{U} = \alpha g \Delta T h^2 / \nu$ (form (4.3)). Squares: $Ra = 2 \cdot 10^6$; circles: $Ra = 10^7$; diamonds: $Ra = 10^8$ and upright triangles: $Ra = 10^9$.

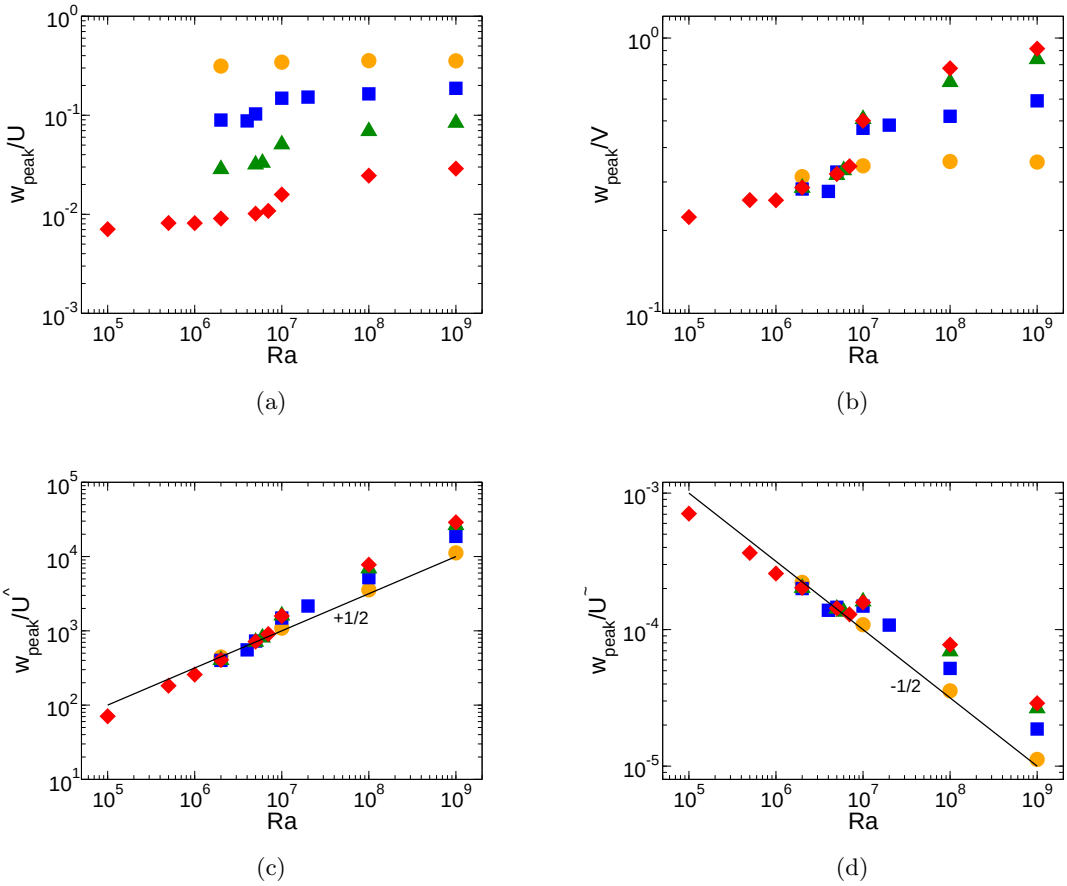

Figure 4.4: Non-dimensional time-average peak vertical velocity as function of Ra. (a) Form (2.1), (b) form (4.1), (c) form (4.2) and (d) form (4.3). Orange circles: $Pr = 10^0$; blue squares: $Pr = 10^1$; green upright triangles: $Pr = 10^2$; red diamonds: $Pr = 10^3$. See caption of figure 4.3 for further details.

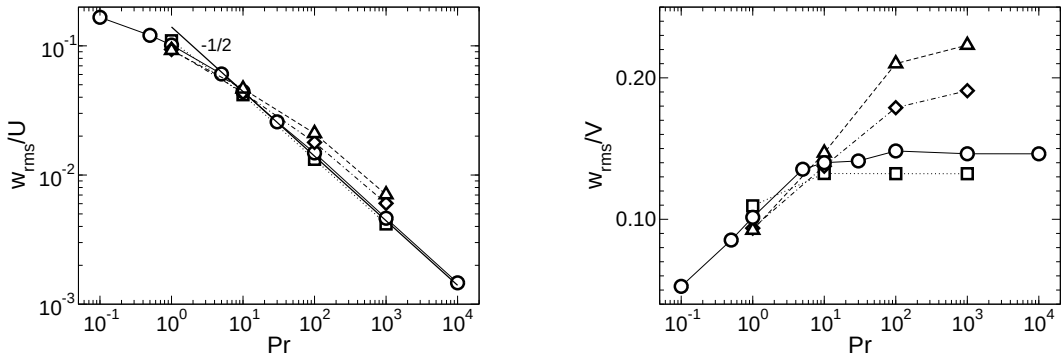

(a) (b)

Figure 4.5: Non-dimensional global rms of vertical velocity as function of Pr. It is $w_{rms} = \sqrt{\langle u_z^2 \rangle_{V,t}}$. (a) Form (2.1) and (b) form (4.1).

weaker and tends to disappear as Pr increases. Plotting the same values as a function of Ra (fig. 4.4), it is possible to see that the non-dimensional peak vertical velocity of the last two non-dimensional forms (figs. 4.4(c) and 4.4(d)) strongly depends on Ra. This dependence is smoothed out in the first two non-dimensional forms (figs. 4.4(a) and 4.4(b)).

It follows from these plots that the non-dimensional form (4.1) leads to a weak dependence of the non-dimensional time-averaged peak vertical velocity on both Pr and Ra numbers at the same time. Note that the non-dimensional peak vertical velocity is of order slightly less than one in the non-dimensional form (4.1), while in all the other non-dimensional forms the values are quite far from unity and span several orders of magnitude with varying Pr or Ra number.

This weak dependence of the typical velocities in the non-dimensional form (4.1) on Pr and Ra numbers is confirmed if other velocities are considered. For example, figure 4.5 shows the global (i.e. averaged over time and volume) rms of vertical velocity. Similar trends are obtained by analyzing other large scale vertical velocities. Instead, typical horizontal velocities have been found significantly depending on the large scale structures characterizing the flow at varying Ra and Pr. As a consequence, the data trends are not monotonic, as shown in fig. 4.6, where the maximum of rms horizontal velocity profile is calculated in non-dimensional forms (2.1) and (4.1). This quantity represents a characteristic velocity of the horizontal viscous boundary layer. In this case, the tendency to reach a saturation value as Pr increases is unclear at higher Ra.

In spite of these uncertainties, non-dimensional form (4.1) is the most suited to describe

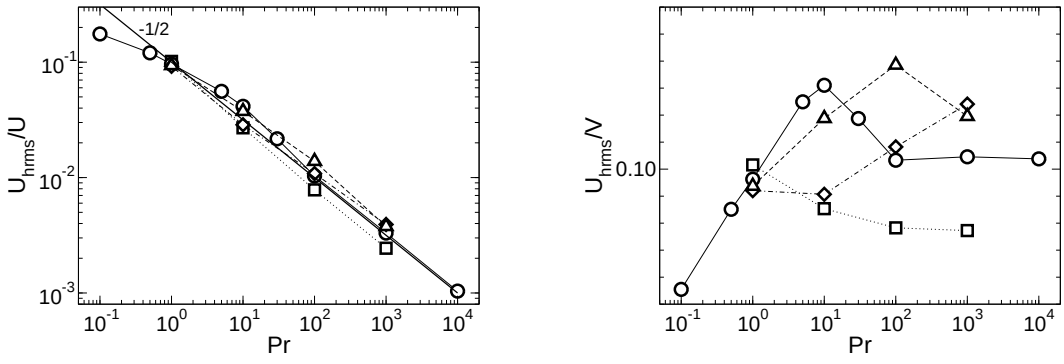

(a) (b)

Figure 4.6: Non-dimensional maximum value of rms horizontal velocity profile as function of Pr. It is $U_{hrms} = max\sqrt{\langle u_h^2 - U_h^2 \rangle_{A,t}}$, where $U_h = \langle u_h \rangle_{A,t}$ and $u_h = \sqrt{u_\theta^2 + u_r^2}$. (a) Form (2.1) and (b) form (4.1).

the dependence on Ra and Pr at $Pr \gtrsim 1$ regimes. Indeed, the diffusive characteristic velocities $\hat{U} = \kappa/h$ and $\tilde{U} = \alpha g \Delta T h^2/\nu$ strongly over- or under-estimate the typical velocities dependence of the flow on Ra (figs. 4.4(c) and 4.4(d)), even if they satisfactorily reflect the dependence on Pr. The free-fall velocity $U = \sqrt{\alpha g \Delta T h}$ represents the typical large scale velocities very well at $Pr = 1$: its ratio with respect to the main velocities results of order one and independent of Ra (see fig. 4.4(a)). The free-fall velocity also captures satisfactorily the dependence of the typical velocities on Ra at higher Pr numbers[4] (fig. 4.4(a)), but strongly under-estimates the typical velocities dependence on Pr (fig. 4.3(a)). Newly proposed characteristic velocity $V = U/\sqrt{Pr}$ represents a synthesis between the diffusive characteristic velocities and the free-fall velocity, maintaining the dependence of the diffusive characteristic velocities on Pr and the dependence of the free-fall velocity on Ra. Besides it is important to note that V is equal to U if $Pr = 1$, preserving a continuity with respect to the free-fall velocity.

It is evident from figs. 4.3(b) and 4.4(b) that corrections to V are necessary to obtain a precise collapse of the curves onto a straight line. The corrections, however, strongly depend on the kind of velocity considered as typical of the flow. Indeed several choices are possible, and even fixing a velocity, corrections depend also on the particular values of Ra and Pr if $Pr \neq 1$.

In comparison to other velocities, the time-averaged peak vertical velocity shows the

[4]The discontinuity in the data trends of fig. 4.4 at around $Ra = 10^7$ is due to the transition from steady to unsteady flows (see chapter 5).

maximum deviations with respect to V. In this case, the best fit of the data is of the type $w_{peak}/V \sim logRa^{\alpha} logPr^{\beta}$ with α and β functions of Ra and Pr. In the range $Ra \leq 10^9$ and $Pr \geq 1$ it results $\alpha, \beta \leq 0.25$, with α almost independent of Pr for $Ra < 10^7$, increasing with Pr for $Ra \gtrsim 10^7$, and β increasing with Ra for $Pr \lesssim 100$, tending to become almost independent of Ra for $Pr > 100$ (see fig. 4.6).

In the range of Ra and Pr explored here, the corrections are smaller than 50%, depending on the values of Ra and Pr considered. However, worse conditions could be found at higher Ra and Pr. The question is how much α and β increase if Ra and Pr increase further, and if there are upper bounds. The available data are not sufficient to show clear trends at higher Rayleigh numbers. Nevertheless some speculations are possible. Indeed, if for Pr higher than Pr_s (a threshold depending on Ra) the ratio of the actual typical velocity and V saturate to a constant value, then β at those Pr results to be zero: $\beta \simeq 0$ for $Pr > Pr_s$ (see fig. 4.7(b)).

A saturation of the velocities ratio with respect to Pr means that α for $Ra > Ra_U$ is expected[5] to saturate to a constant value $\alpha_s > 0$. This value α_s should represent an upper limit if the α dependence on Pr is monotonically growing. Then at $Pr > Pr_s$ and $Ra > Ra_U$ the corrected characteristic velocity should be $V \cdot logRa^{\alpha_s}$ with α_s expected not much higher than 0.25. At $Pr < Pr_s$ it would result $\alpha < \alpha_s$, then a smaller correction of V with respect to Ra should be necessary. On the contrary β at $Pr < Pr_s$ could be consistently increasing with Ra, without a recognizable upper bound in the available data.

In summary, for high Pr numbers the characteristic velocity V could need a bounded logarithmic correction involving the Ra number to well represent a typical velocity having a behavior similar to that shown by the time-averaged peak vertical velocity. At lower Pr instead, a Pr correction could be necessary as Ra increases, while a Ra correction becomes less necessary as Pr decreases. It is worth remembering that the measure of the corrections depends on the particular velocity considered as typical of the flow and on the specific values of Ra and Pr. Moreover, for most of the velocities the behavior is not monotonic with respect to Ra and Pr, implying that the corrections can also qualitatively change.

As a conclusion, the velocity $V = U/\sqrt{Pr}$ is confirmed, through simulations, as being suitable to represent, at least in the first approximation, the characteristic velocity of the convective flows at high Pr numbers. Consequently, the non-dimensional form (4.1) results the most satisfactory to describe the convective dynamics at high Pr. The velocity V, relating the momentum dynamics to those of the temperature, represents an estimate of

[5] Ra_U represents the threshold Ra for transition from steady to unsteady flow (see chapter 5).

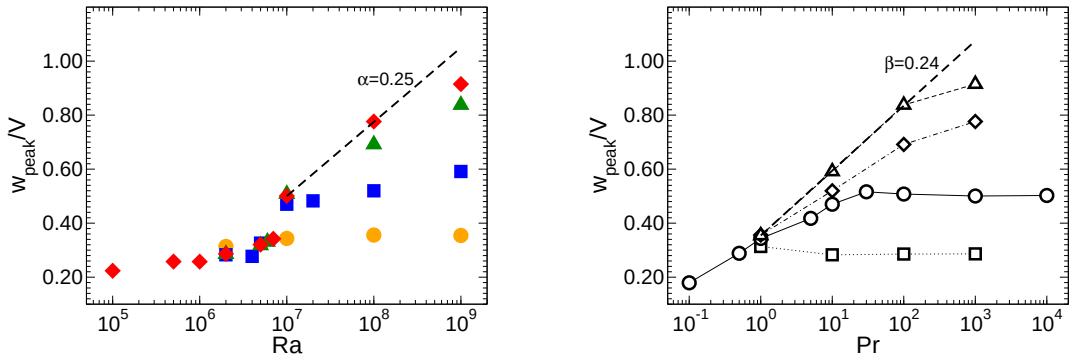

(a) (b)

Figure 4.7: Non-dimensional time-average peak vertical velocity as a function of Ra (a) and of Pr (b) in a log-linear plane. The new characteristic $V = U/\sqrt{Pr}$ is used to non-dimensionalize the peak vertical velocity.

the convective velocity U_c introduced in the previous chapters, and the corresponding time $\tau_V = h/V$ represents an estimate of the convective time τ_c.

4.4 Reynolds and Peclet numbers

Strictly linked to the characteristic velocity are Re and Pe. As already explained in section 4.2, different non-dimensional forms imply different Re and Pe dependences on Ra and Pr. These dependences, however, are only formal, unless we consider a non-dimensional form which really describes the convective dynamics. The correct evaluation of Re and Pe is an important issue because most of the theories about bulk and boundary layer behaviors of a convective cell are derived from the classical theories of incompressible pressure-driven flows, in which Ra and Pe play a fundamental role.

Using the characteristic velocity $V = U/\sqrt{Pr}$, where U is the free-fall velocity, a rough estimate of the actual Re number is $Re \sim \sqrt{Ra}/Pr$ and consequently $Pe \sim \sqrt{Ra}$, independent of Pr. More precise estimates need the corrections of the type discussed for the characteristic velocity and imply identical uncertainties (see the previous section), because the actual Reynolds number is given by $Re \cdot (u_a/V)$, where Re is based on V and u_a is an actual typical velocity of the flow.

Figure 4.8 shows the actual values of Re compensated by Pr^{-1}, this being equal to Pe, as a function of Ra and Pr. In figs. 4.8(a) and 4.8(b) the Re number is based on time-averaged peak vertical velocity, in figs. 4.8c and 4.8d, instead, the maximum value of the

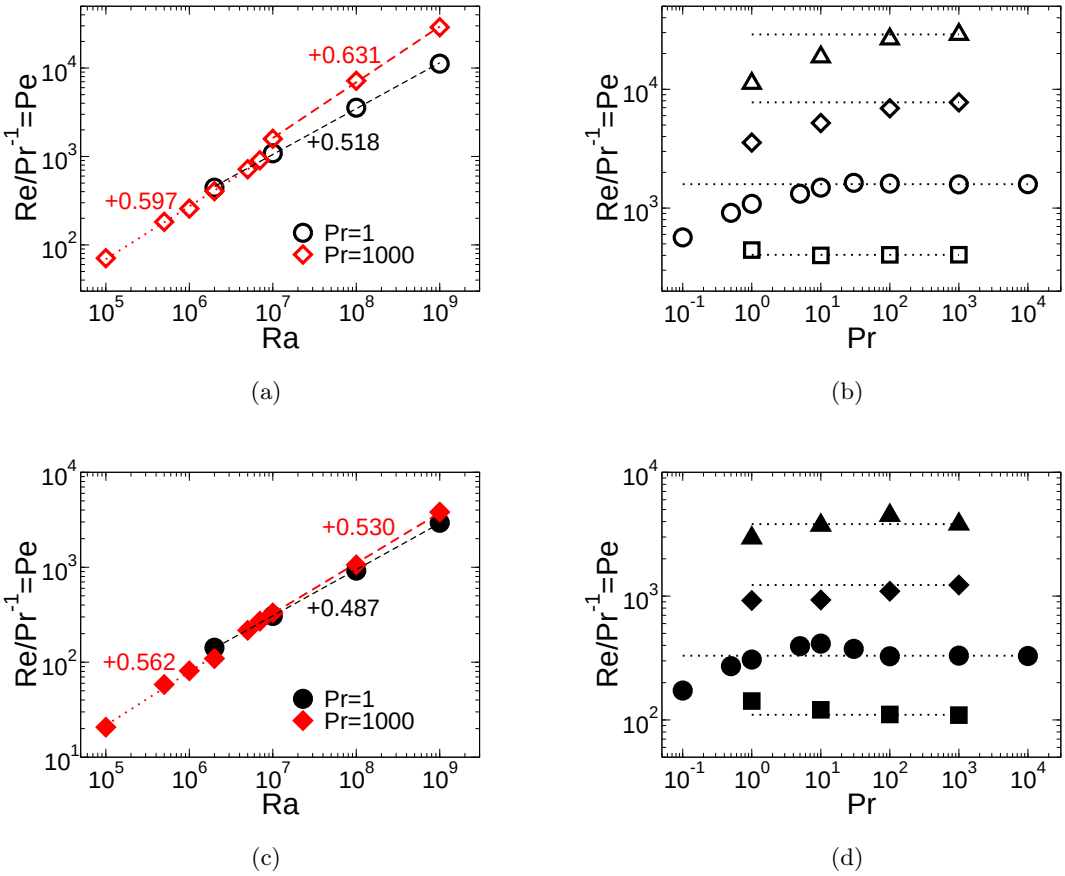

Figure 4.8: Re number divided by Pr^{-1} calculated using the time-average peak vertical velocity (open symbols) and the maximum value of the rms horizontal velocity profile (filled symbols). In (b) and (d): squares: $Ra = 2 \cdot 10^6$, circles: $Ra = 10^7$; diamonds: $Ra = 10^8$; upright triangles: $Ra = 10^9$.

rms horizontal velocity profile is considered. In figs. 4.8(a) and 4.8(c) the best exponents of a power-law fit are shown, considering steady and unsteady solutions separately.

At high Pr, the Reynolds number has a power law dependence on Ra with exponent higher than 1/2. In the case of the peak vertical velocity (4.8a) at $Pr = 10^3$ and $Ra \geq 10^7$ the relative discrepancy of the actual exponent with respect to the exponent 1/2 is more than 25%. The growth of the Ra power law exponent with increasing Pr is qualitatively in agreement with previous experimental results [46].

Instead of considering a power-law fit, a logarithmic fit can be considered for corrections of the 1/2 power law[6] (see previous section). At high Pr it implies: $Re/Pr^{-1} \simeq \sqrt{Ra} \cdot logRa^{\alpha_s}$. In that case relative corrections with respect to the 1/2 power-law in the range of Ra considered were less than 50%, with an error growth with Ra much smaller than the resulting power law correction mentioned above. However, at $Ra > 10^9$ a transition is expected, after which experimental results show $Re \sim \sqrt{Ra}$ (and a function of Pr) ([14], [46]), then at high enough Rayleigh numbers no Ra corrections should be necessary. This transition in [46] was found at $Ra \simeq 3 \cdot 10^7$, but in our simulations such kind of transition is not visible.

Figures 4.8(b) and 4.8(d) show the behavior of Re with respect to Pr at different values of Ra. The Reynolds number is divided by Pr^{-1} to better show the trends. For all Rayleigh numbers and for both choices of typical velocities, the data tend to approach constant values as Pr increases. At $Pr \geq 100$ the deviation from a constant value is less than 3.6%. At lower Pr the deviations can exceed 50%, strongly depending on Ra and on the kind of velocity considered. In particular, considering the case of Re based on the peak vertical velocity (fig. 4.8(b)), the deviation from the scaling Pr^{-1} increases with increasing Ra.

For $Ra = 10^7$ and $Pr \leq 1$, the power-law dependence of Re on Pr is approximatively $Re \sim Pr^{-0.71}$. This seems to be consistent with the results of Verzicco and Camussi [77]. At $Ra = 6 \cdot 10^5$ and in a cell of aspect ratio $\Gamma = 1$, they found that the Pr exponent of Re crosses over from -0.73 to -0.94 when Pr increases. The exponent -0.7 was also found in [52], where the trend of Re versus Pr is plotted for a wide interval of Pr ($0.02 \lesssim Pr \lesssim 200$). The data come from experiments of different authors; the aspect ratio varies between 1/2 and 1; some data were extrapolated for holding Ra fixed at 10^{10}. Instead, the data of experiments by [81] show an exponent of -0.95 for high-Pr regimes ($10 \lesssim Pr \lesssim 10^3$), in a

[6]The few available points for each data series doe not allow to recognize a precise trend. With few points several kinds of fit are plausible. However, subtracting what is considered the main trend, the remaining corrections are more visible. The compensated Re with respect to Pr number of figs. 4.8(b) and 4.8(d) is an example. Considering Re based on the peak vertical velocity (fig. 4.8(b)), a power law is clearly not the best fit of the data. Changing the vertical scale from logarithmic to linear, nearly straight lines appear instead of curves. The same happens in the previous section while comparing, for example, figs. 4.3(b) and 4.7(b), or 4.3(a) and 4.7(a). For this reason logarithmic corrections were proposed. However, even in this case, no single set of coefficients fits satisfactorily all the data trends.

cell with $\Gamma = 1$, and Ra between 10^8 and 10^{10}.

These results seem to confirm the presence of a low-Pr regime, where approximately $Re \sim Pr^{-0.7}$, and a saturation regime at very high-Pr ($Pr \gtrsim 100$), where $Re \sim Pr^{-1}$. The transition from one regime to another seems to depend, apart from the Rayleigh number, on the aspect ratio of the cell. A smooth approach to the saturation regime, as that shown by our data, could justify the discrepancy in the scaling exponents found by the different authors.

Chapter 5

Transitional phases and flow structures

5.1 Introduction

In the range of Ra and Pr explored in this work we found steady, periodic and chaotic solutions. The transition from one convective state to another represents an open and fascinating problem, especially in small aspect-ratio cell ($\Gamma \lesssim 1$), where the flow structure strongly depends on system geometry. Almost all the pattern-development studies concern convective systems with large aspect ratio ($\Gamma \gg 1$) [9]. For cells of moderate aspect ratio ($1 \lesssim \Gamma \lesssim 10$) a short review can been found in [11] concerning the work on the first convective states. Through experiments, numerical simulations and theoretical calculations the work just cited mainly provides a stability analysis of convective states. In particular, they show that the critical Ra for the onset of motion steeply increases above the theoretical value ($\Gamma \to \infty$) when Γ decreases below two [20]. This means that, for fixed geometry and fluid, a higher temperature difference has to be applied in order to obtain convective motion in cells of small aspect ratio. Other results are that non-axisymmetric motions appear in the earlier convective state when Γ is sufficiently small ($\Gamma \lesssim 1$) ([35], [53]); the possibility of several different stable patterns for the same final Ra and Pr [37]; periodic behavior through a secondary bifurcation ([24], [25], [60]). Our simulations reflect these findings.

In section 5.2 we propose a qualitative description of convective states and of flow patterns found in our simulations at high Prandtl number. A rough estimate of the transition from steady to unsteady flow has been found in simulations close to this transitional regime

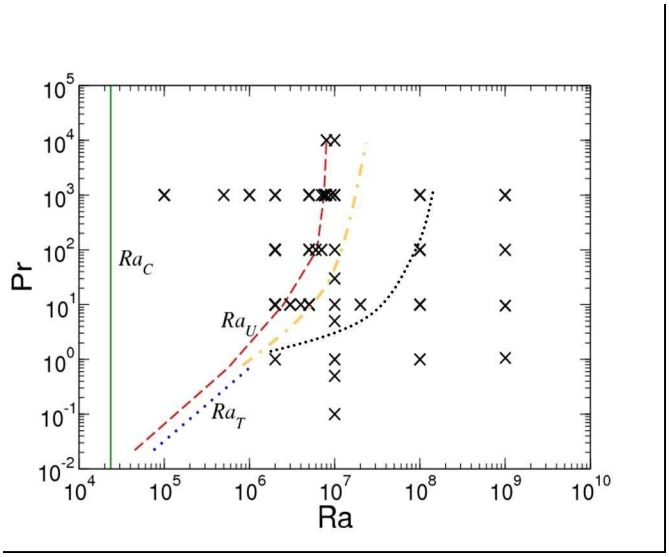

Figure 5.1: A picture of transition phases. Crosses: our simulations; green solid line: Ra_c for the onset of motion; red dashed line: Ra_U of transition from steady to unsteady flow; yellow dot-dashed line: qualitative indication of transition from periodic to chaotic flow; blue dotted line: qualitative indication of transition from chaotic to turbulent-like flow.

and the time evolution of the system up to stationary solutions has been monitored. The main features of the convective structures of unsteady solutions are presented in section 5.3, where we report an analysis of the flow structures performed by temperature and velocity field visualizations.

5.2 A qualitative picture of transitions

A layer of fluid heated from below and cooled from above starts to move only when the applied temperature difference across the layer is sufficiently high, so that the destabilizing forces exceed the opposition of viscous effects. A measure of these opposite effects is represented by the Rayleigh number. Thus, the motionless state is stable up a critical Rayleigh number Ra_C, whose value depends on the aspect ratio $\Gamma = D/h$ (diameter over depth), and on the geometry of the domain. The Ra_C is independent of Pr [19]. For a cylindrical cell with $\Gamma = 1/2$, the critical Rayleigh number is[1] $Ra_C = 2.35 \cdot 10^4$ [53] (solid green line in fig. 5.1).

Above Ra_C, steady convective motions appear [53]. In agreement with results concerning cells of high aspect ratio [45], we found that the steady state persists for a longer Ra interval

[1]This value is much higher than the theoretical Ra_C relative to an infinitely extended layer of fluid ($Ra_C = 1708$ for $\Gamma \to \infty$ [19]). As a consequence the other transitional phases will also be shifted towards higher Ra.

as Pr increases.

During the steady phase the flow can be characterized by different flow structures. In figure 5.2 the top row shows the typical patterns of the steady solutions at $Pr = 10^3$ and increasing Ra. After the onset of motion, the flow pattern is the same as for lower Pr [76]: a single smooth roll filling the whole cell (fig. 5.2(a)). This pattern reveals a well-known but still surprising propensity of the convective flow to form a two-dimensional-like[2] structure, even when the container in strongly three-dimensional. The temperature iso-lines tend be bent.

With increasing Ra we found that the flow becomes strongly three-dimensional. In addition to the single roll, smaller vortices appear at the edges of the top and bottom plates, and the big central roll twists in the azimuthal direction[3]. Hot and cold parts of fluid start to penetrate each other (fig. 5.2(b)).

After this phase and before the onset of unsteady motion ($Ra \gtrsim 5 \cdot 10^6$ at $Pr = 10^3$), the flow is again similar to a two-dimensional set-up, mainly consisting of the single roll. The fluid temperature appears almost uniform in the bulk, while hotter fluid rises along one side of the lateral wall and colder fluid falls along the other (fig. 5.2(c)). When hotter and colder fluids meet at the edges of the plates, they form small eddies.

Increasing further Ra there is a transition from steady to unsteady flow. The unsteadiness at $Pr = 10^3$ appears in the flow as a couple of small hot and cold waves (hills) along the top and bottom plates. Traveling around the single-roll structure, they tend to detach along the sidewall forming hot and cold blobs, which force the formation of the subsequent couple of waves when they reach the corresponding opposite plate, and so on (fig. 5.2(d)). With slight increase in Ra, the blobs becomes more bulging. This traveling-wave phenomenon corresponds to a local periodic solutions (i.e. the velocity and temperature signals in each point of the domain are periodic).

The transitions through a possible chaotic regime and to turbulence could not be investigated, because of the great difficulty on performing high-Pr simulations (see sec. 2.4.3). After single-roll periodic solutions, we found at higher Ra strongly thee-dimensional structures

[2]In cells of high aspect ratio the most common convective structure is an array of rolls. These rolls (as pipes) have a diameter of the same size of the cell height, and, generally, develop parallel to each other, forming, far from the boundaries, a typical two-dimensional structure [74]. In cell of small aspect ratio the sidewalls are too close to each other for allowing the formation of rolls really two-dimensional. Nevertheless, the three-dimensional structures of small aspect-ratio cells present often features similar to the two-dimensional roll structure.

[3]A single-roll structure with an azimuthal torsion appears as one of many possible multiple steady solutions having a lower or higher degree of torsion. Indeed, we found at $Ra = 2 \cdot 10^6$ and $Pr = 10^2$ two steady solutions mainly consisting of a single-roll structure, one with and the other without an azimuthal torsion. The same situation occurs at $Ra = 2 \cdot 10^6$ and $Pr = 10$. Checks performed using several grids and different initial conditions confirm these results.

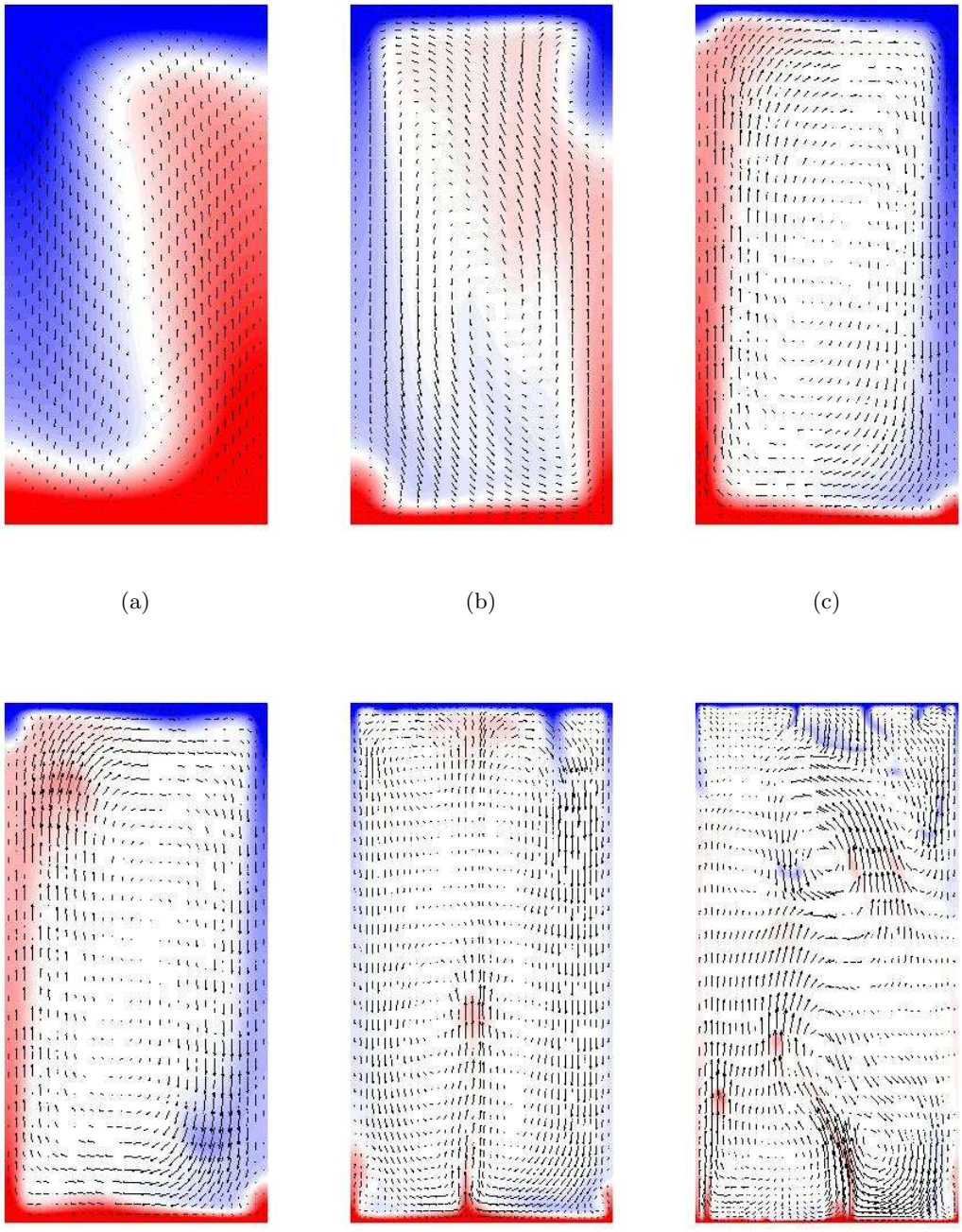

(a) (b) (c)

(d) (e) (f)

Figure 5.2: Flow structures at $Pr = 10^3$. (a) $Ra = 10^5$; (b) $Ra = 2 \cdot 10^6$; (c) $Ra = 7 \cdot 10^6$; (d) $Ra = 8 \cdot 10^6$; (e) $Ra = 10^8$; (e) $Ra = 10^9$. The color map represents the temperature field and saturates at higher and lower temperature: $0 \leq \Theta \leq 0.2$ blue; $0.8 \leq \Theta \leq 1$ red; $\Theta = 0.5$ white; $0.2 < \Theta < 0.8$ linear blue-white-red scale. The arrows show the velocity vectors tangent to the vertical section.

different from single-roll structures. In particular, at $Pr < 100$, the solutions mainly show toroidal ring structures attached to the horizontal plates (see next section). At $Pr \geq 100$ the simulations generally show structures mainly developing in the vertical direction. The instantaneous solutions are, however, strongly unsteady and characterized by plume emissions[4] (figs. 5.2(e) and 5.2(f)).

After the single-roll structure, at $Pr = 10^3$ and $Ra = 10^8$ we found a stationary two-cell structure, which splits in a three-cell and then four-cell structure as a long-term variation (fig. 5.3; see also sec. 3.4). The two-cell and three-cell structures (figs. 5.3(a) and 5.3(b)) were found as steady solutions in experiments performed with water in a cylindrical cell of aspect ratio $\Gamma = 4$ [37]. However, in our case, the structures are quite complex and strongly three-dimensional. We have called the flow structures in base on the number of sectors visible close to the bottom plate (figs. 5.3(a), 5.3(b) and 5.3(c)), but these sectors do not really represent cell structures. Indeed, close to the top plate, the flow generally does not show the same structure as at the top plate (figs. 5.3(d), 5.3(e) and 5.3(f)). The flow structure at the plates is determined by the number and position of hot-rising and cold-falling jets which are present in the flow. Figures 5.3(g), 5.3(h) and 5.3(i) show the vertical velocity iso-lines at the mid-plane, corresponding to the above mentioned structures, when they are averaged over long time interval. The vertical jets are organized in well defined structures.

The jets are formed by plumes emitted close to the plates and along the sidewall, which cluster together. The hot fluid is pushed, from the bottom plate along the sidewall, by cold jets arriving from above. In the central region, the cold fluid, arriving from different directions, lifts up thin layers of hot fluid, forming sheet-like structures. Portions of fluid detaching from them generate hot rising plumes. These plumes tend to cluster towards nodal points (which generally are the points where the inner and sidewall sheet structures cross each others), forming rising jets. When the hot jets arrive to the top plate, they generate similar cold sheet structures (second row of figure 5.3), from which plumes detach and cluster forming sinking cold jets, and so on.

It is worth noting that the number and direction of the hot and cold jets depends on the number and position of the nodal points. The result is a rotation or a different composition of the sheet-like structures between top and bottom plates. The corresponding flow is in general strongly three-dimensional. However, in the case of two-cell structure (figs. 5.3(a) and 5.3(d)) we schematize it in two opposite vertical rolls (see next section).

The number jets is quite stable in all the three-cell structures. Their position and the

[4]A description of unsteady flow structures is also provided in the next section.

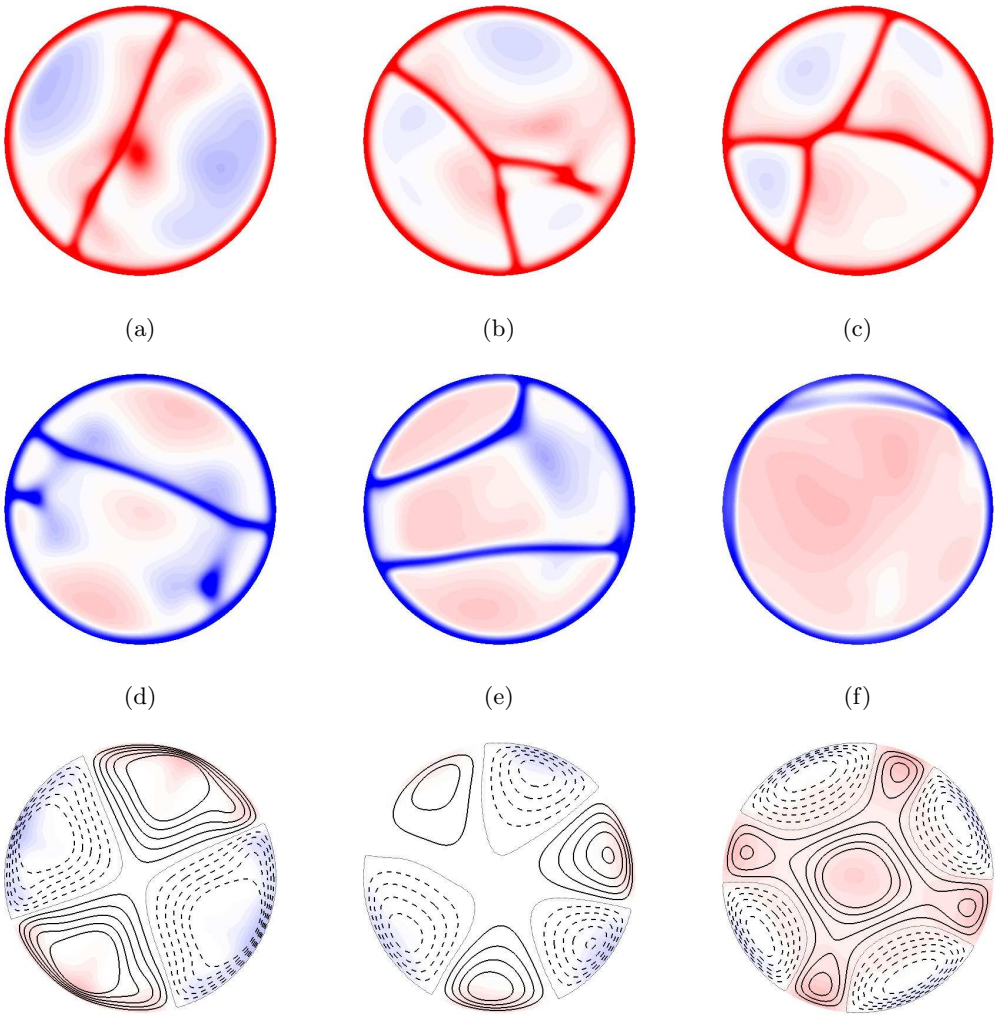

Figure 5.3: Multiple flow structures at $Pr = 10^3$ and $Ra = 10^8$. First row: instantaneous structures close to the bottom plate; second row: corresponding instantaneous structures close to the top plate; third row: mean-flow structures at the mid-plane; (a), (d) and (g) two-cell structure; (b), (e) and (h) three-cell structure; (c), (f) and (i) four-cell structure. Color map: temperature field (notation as fig. 5.2). Lines: vertical velocity w. Solid lines: $w > 0$; dashed lines: $w < 0$; thin dotted lines: $w = 0$.

corresponding sheet structures are almost stationary in the two-cell and four-cell structure (see sec. 3.4).

The solution at $Pr = 10^3$ and $Ra = 10^9$ is still characterized by sheet-like structures, which, however, are more complex and less stationary. The prevailing structure in this case is a three-cell structure (figs. 5.8(e) and 5.8(f)), corresponding to three ascending and three descending jets.

Going back to the transition from steady to unsteady flow we found that at $Pr = 10^3$ the threshold value (Ra_U) is approximatively equal[5] to $Ra_U \approx 7.5 \cdot 10^6$ ($7 \cdot 10^6 < Ra_U < 8 \cdot 10^6$).

A rough estimate of Ra_U was also obtained at lower Pr: $2 \cdot 10^6 < Ra_U < 3 \cdot 10^6$ at $Pr = 10$, and $5 \cdot 10^6 < Ra_U < 6 \cdot 10^6$ at $Pr = 10^2$. Using the results of previous simulations performed by Oresta *et al.* [53] at lower Pr, it was possible to derive an estimate of Ra_U on a wide range of Pr numbers (red dashed line in fig. 5.1).

It is possible to note that, in contrast to Ra_C for onset of motion, Ra_U for transition from steady to unsteady flow strongly depends on Pr number, before of reaching a saturation value at $Pr \gtrsim 10^2$.

The simulations performed at $Pr \geq 10$ show that the unsteady state appears as a local periodic motion (see above). This agrees with previous results obtained at lower Pr ([53], [76]). We distinguish between steady and periodic solutions by checking if signals of local quantities are steady or periodic when the volume-averaged temperature reaches a steady state (see fig. 5.4). Indeed, we have found that the volume-averaged temperature signal[6] results to be steady not only when the flow is steady, but even when the flow is periodic.

The identification of Ra_U is, however, only approximate since the closer Ra is to Ra_U, the longer the relaxation time of the system. This implies that very long simulations must be carried out in order to distinguish the slowly damped from sustained oscillations. No simulation was sufficiently long to obtain a steady volume-averaged temperature signal very close Ra_U.

With increasing Ra the picture becomes vague because the simulations are too sparse. Above periodic solutions we have simulations which still present some isolated peaks in the spectrum of the Nusselt number signal and simulations which have lose periodicity features (no distinguishable peaks in the Nu spectrum). Figure 5.5 shows the Nu signals and the corresponding spectra for unsteady solutions at $Pr = 10^3$. At $Ra = 10^7$ the periodic solution

[5]This value was derived from simulations performed in the range $7 \cdot 10^6 < Ra < 8 \cdot 10^6$. These simulations, however, were not sufficiently long to be sure that the damping or sustained oscillations characterizing their solutions really approach steady or periodic solutions. Convergence was only obtained at $Ra = 7 \cdot 10^6$ and $Ra = 8 \cdot 10^6$ (see later).

[6]The volume-averaged temperature signal behaves as an indicator of the long-term phenomena of the system. See also section 3.4.

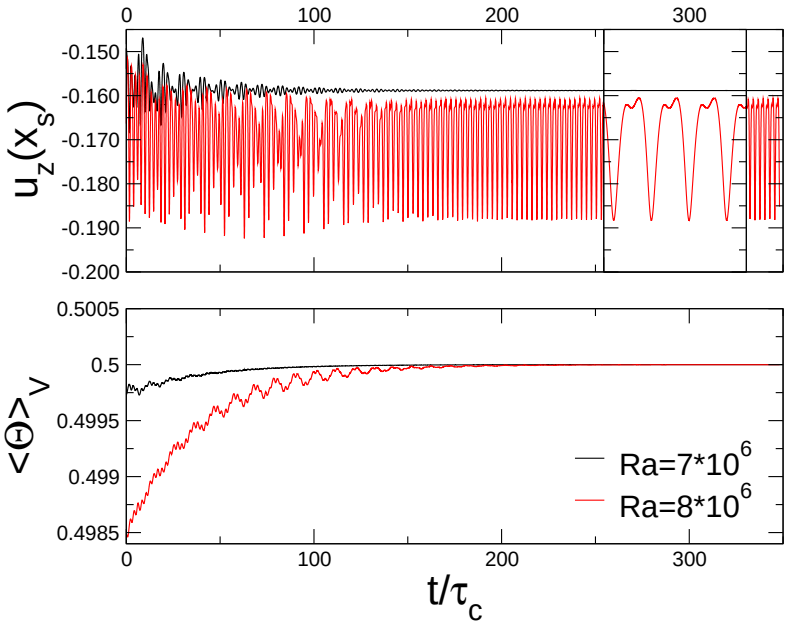

Figure 5.4: Time signals before and after transition from steady to unsteady flow at $Pr = 10^3$. Top: vertical velocity signal measured in an inner point x_s of the cell ($x_s = (\theta_s, r_s, z_s)$ with $\theta_s = 0$, $r_s = 0.2$ and $z = 0.1$). Bottom: volume-averaged temperature signal. All the shown quantities are made non-dimensional according to equations (4.1)

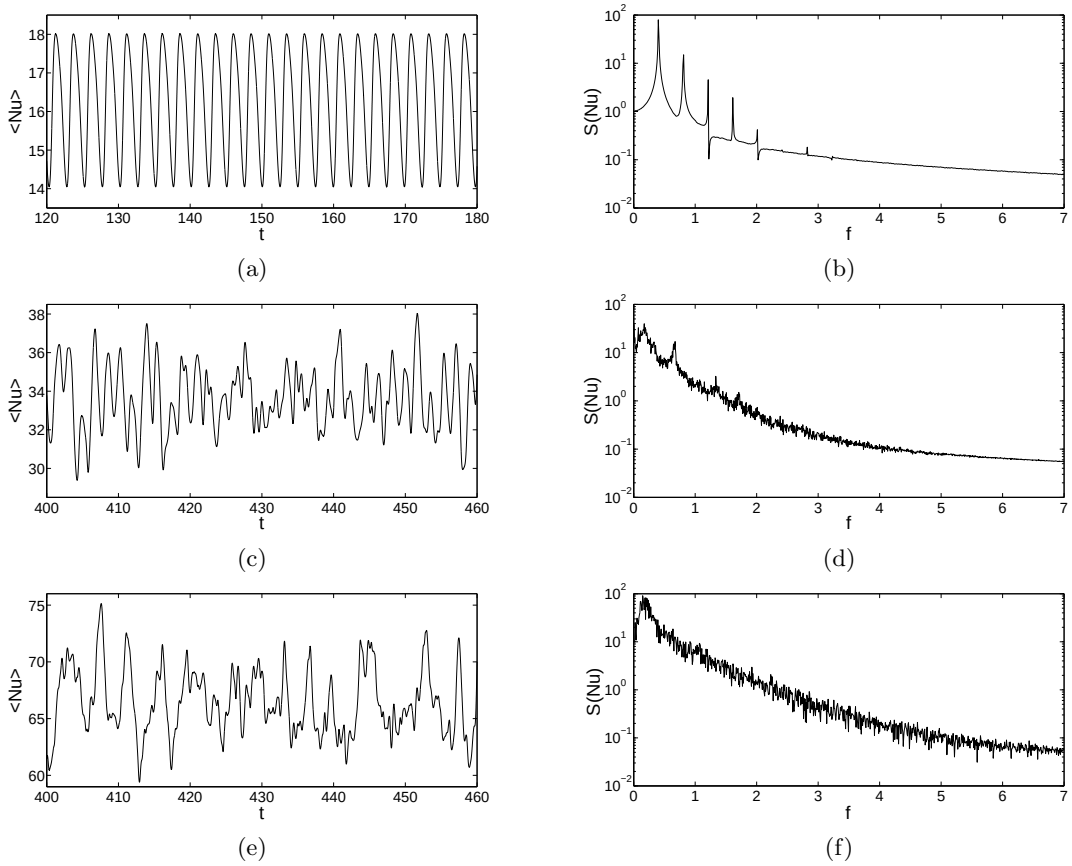

Figure 5.5: Bulk Nusselt number signal and corresponding spectrum. (a),(b) $Ra = 10^7$; (c),(d) $Ra = 10^8$; (e),(f) $Ra = 10^9$.

shows multiple frequencies (fig. 5.5(b)). At $Ra = 10^8$ the spectrum is almost continuous even if it is possible to recognize modest frequency peaks (fig. 5.5(d)). At $Ra = 10^9$ no isolated peak of frequency is present (fig. 5.5(f)). The spectra show a wider frequency interval as Ra increases. However, at such a high Pr and moderate Rayleigh numbers, the velocity fluctuations with respect to a mean flow circulation are quite limited in strength, thus the flow is not yet fully turbulent (see next section).

Figure 5.1 includes a qualitative indication of transition from periodic to a presumably chaotic regimes (yellow dot-dashed line) ([53], [76]), and of transition from chaotic to turbulent-like solutions (blue dotted line). This picture shows that, in order to obtain turbulent-like solutions at high Pr, simulations at Rayliegh numbers much higher than those at $Pr \sim 1$ have to be performed, strongly increasing the computational requirements.

5.3 Large scale structures

As already shown above, convective cells are characterized by a macroscopic fluid motion generally consisting in large scale circulations and plume emissions. Under the destabilizing effect of the temperature gradient applied to the cell, hot (cold) fluid portions tend to rise (fall) due to the buoyancy forces. As a consequence, other fluid portions must fall (rise) because of mass conservation. This mechanism generates a macroscopic motion of fluid, i.e. large eddies, more or less stationary[7], which sweep fluid along the plates, allowing the formation of thermal and viscous boundary layers.

Blobs of rising hot (falling cold) fluid can be organized in coherent structures called plumes. These plumes, generally represented as mushroom-shaped objects, can emerge randomly from top and bottom plates or can detach from stable positions along the plates, depending on the degree of turbulence present in the flow. The plumes generally tend to cluster, swept from large scale circulations, forming uprising hot jets and downward cold jets. These jets feed large scale circulations.

Large scale circulations and plumes, when averaged on time, compose the mean flow structure. The mean flow depends on the time-window considered for the averaging. In order to study short-term convective dynamics, we neglect long-term variations, applying a time-average on sub-intervals of time, when necessary (see sec. 3.4).

We refer to the large scale circulation as any kind of instantaneous, steady or stationary

[7]When the flow is very turbulent ($Ra > 10^{14}$ for $Pr \sim 1$) structured large scale circulations eventually disappear [70]. It is, however, conjectured that the strongly unsteady eddies allow the boundary layer formation.

large eddy having a size of the same order of the cell depth, and swirling mainly in vertical direction. When a large scale circulation shows steady or stationary features, it is also referred to as pattern or mean wind.

All these structures contribute to the heat transfer mechanism, interacting with each other in a non-linear way. In different regimes of Ra and Pr plumes and large scale circulations are different and behave differently. In spite of this, some other results can be unchanged. This is the case of the total heat transport, represented by the Nusselt number, which remains almost constant as Pr increases for $Pr \gtrsim 1.6$ (see chapter 6.1), even when the flow structures seem to present different features.

In order to contribute to the comprehension of this unexpected result, in the following part we describe the flow structure features with increasing Pr.

5.3.1 Large scale structures at increasing Pr

The flow structure analysis has been performed through a visual inspection of three dimensional (3D) temperature and velocity fields. This kind of analysis is important because in laboratory experiments the flow structures are mainly conjectured from indirect evidence, owing to great difficulty in obtaining images and velocity measurements inside the flow through experimental techniques.

A time-evolution analysis of flow structures is quite complex owing to the strong 3D features of the flow snapshots. Thus, in addition to 3D visualizations of instantaneous and mean fields, we have monitored the temperature map at the sidewall as a function of time in most of the simulations. In cells of small aspect ratio the flow circulations mainly develop close to the sidewall. Therefore the temperature map at the sidewall reflects the main features of the flow structures.

Looking at the movies of the temperature map at sidewall, it is immediately evident that the fluctuating activity decreases with increasing Pr. Indeed, as Pr increases the sidewall temperature map shows a less uniform temperature distribution and a more stationary flow.

Figure 5.6 shows a typical snapshot of temperature field at sidewall at different Pr and $Ra = 10^8$. At $Pr = 1$ the temperature maps show plume tracks that randomly appear in various azimuthal positions of top and bottom edges. Corresponding large scale circulations do not cluster in any recognizable form, the mean temperature strongly varying in time and along azimuthal and vertical directions (fig. 5.6(a)). Analyzing the flow interior, we found the scenario that is described in [78]: opposite eddies are attached to the horizontal plate edges, composing two counter-rotating toroidal rings. The flow is also swept by unstructured

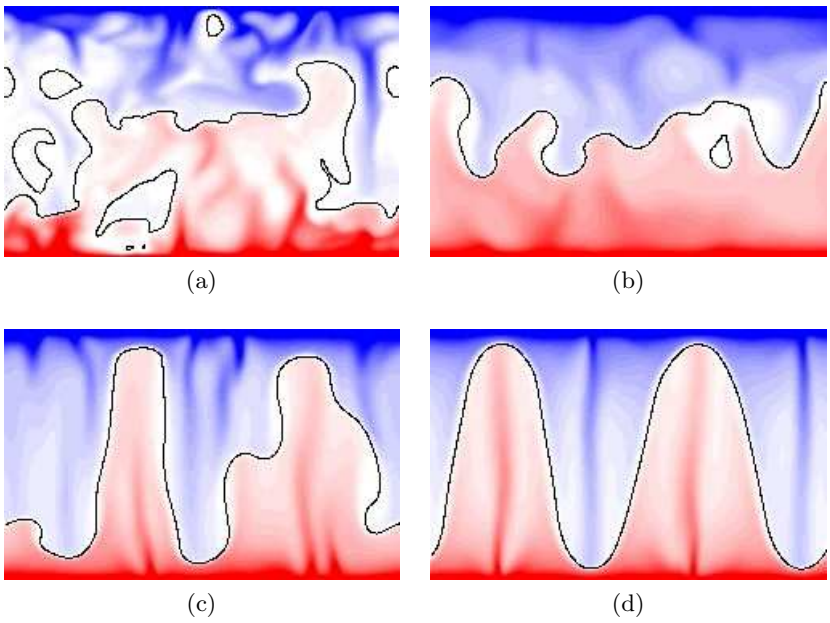

Figure 5.6: Sidewall map of temperature representing the typical instantaneous flow structures at $Ra = 10^8$. (a) $Pr = 1$; (b) $Pr = 10$; (c) $Pr = 10^2$; (d) $Pr = 10^3$. The color map saturates at higher and lower temperature: $0 \leq \Theta \leq 0.2$ blue; $0.8 \leq \Theta \leq 1$ red; $\Theta = 0.5$ white; $0.2 < \Theta < 0.8$ linear blue-white-red scale. Black solid line: $\Theta = 0.5$.

scale recirculations, which carry hot and cold fluid portion up to the corresponding opposite plates mainly along the sidewall.

The corresponding mean flow is axisymmetric, consisting in two toroidal structures, with the flow descending along the axis and ascending along the sidewall in the bottom half of the container, the opposite in the top half (first panel of fig. 5.7). When averaged the hot flow remains confined in the bottom half of the container and the cold flow in the top one.

On the contrary at $Pr = 10^3$, the sidewall temperature maps show plume tracks almost fixed. Only small oscillations are visible in the azimuthal direction. The corresponding large scale circulations consist in well-defined structures (fig. 3.3) which are stationary for a long time interval. The sidewall temperature map of fig. 5.6(d) corresponds to the two-cell structure, schematically consisting to two opposite vertical roll[8]. The flow basically consists in its mean component, which exactly reflects these structures (last panel of fig. 5.7), since the fluctuating activity is reduced to the plume emission along an almost fixed position (see more details in sec. 5.2). Even when the flow is averaged, portions of hot fluid are present close to the top cold plate, and vice-versa.

[8]The usual single-roll structure shows a similar map, but with only one hot "finger" ascending and one cold "finger" descending.

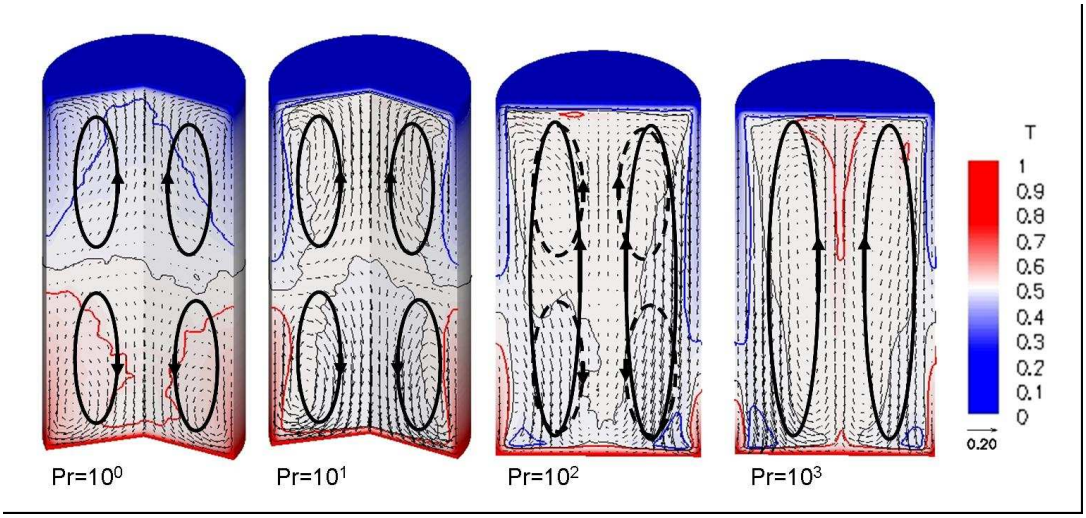

Figure 5.7: Mean flows at $Ra = 10^8$ and increasing Pr. Black line: $\Theta = 0.5$; red line: $\Theta = 0.515$; blue line: $\Theta = 0.485$. The red and blue lines correspond to a temperature drop of 97%.

At $Pr = 10^2$ the temperature map shows a behavior similar to that at $Pr = 10^3$, but with a stronger movement of plumes in the azimuthal direction, and with a consequent higher variability in the large scale circulations (fig. 5.6(c)). The corresponding mean flow is more complex than the previous case, but still mainly consisting in ascending hot fluid in the center and descending cold fluid along the sidewall (third panel of fig. 5.7).

At $Pr = 10$ plume tracks appear randomly for at $Pr = 1$, but with hot and cold fluids more poorly mixed. The plumes show a lower capability to penetrate in the vertical direction than that of plumes at higher Pr values. As a consequence the large scale circulation is mainly separated in two axisymmetric structures each of which is confined to the bottom and top halves of the container (fig. 5.6(b)). However, when the hot front rises along the sidewall and meets the descending cold front and the flow deviated towards the cell interior, portions of hot fluid are dragged up by the upper side recirculations; and the opposite is true for cold fluid. The mean flow consists in the two toroidal structures as at $Pr = 1$, but in this case portions of hot fluid are present in the upper side of the cell, and cold fluid in the bottom side (second plot of fig. 5.7).

The flow shows a clear tendency to develop on the average circulations more extensive in the vertical direction as Pr increases. At higher Pr these circulations are driven by vertical jets fed by plumes detaching from sheet-like structures and clustering in some nodal points (see sec. 5.2). The plumes show a higher penetrating capability in the bulk region as Pr increases. The average effect is a mean flow which presents at higher Pr portions of the

hottest (coldest) fluid close to opposite cold top (hot bottom) plate.

The presence hot fluid close to the top cold plate (and vice-versa) is due to the fact that the small fluctuations with respect to the mean flow (low Re) do not allow an effective mixing. Therefore, a fluid portion, detaching from the plates, owns a greater tendency to be buoyant, since its temperature remains different with respect to the local environment for longer time. Consequently, hot (cold) fluid portions are able to reach the top (bottom) without significantly losing heat and therefore change of temperature. The result is that large parts of cold fluid are directly in contact to large parts of hot fluid also close to the plates[9].

It is important to note that this phenomenon is relevant only in averaged flows. Indeed, in instantaneous flows hot fluid reaches the top plate even at low Pr (fig. 5.8).

In summary, all the unsteady simulations at $Pr < 100$ which are not periodic shows a axisymmetric mean flow mainly consisting in two opposite toroidal structures. At $Pr \geq 100$ the mean flow circulations are more extended in the vertical direction, since they seem to be mainly driven by highly penetrating plumes. The variety of these structures at increasing Ra do not allow one to obtain data trends that are clear with respect to Ra.

[9]The local inversions of temperature profiles shown in section 7.2 are a manifestation of this phenomenon.

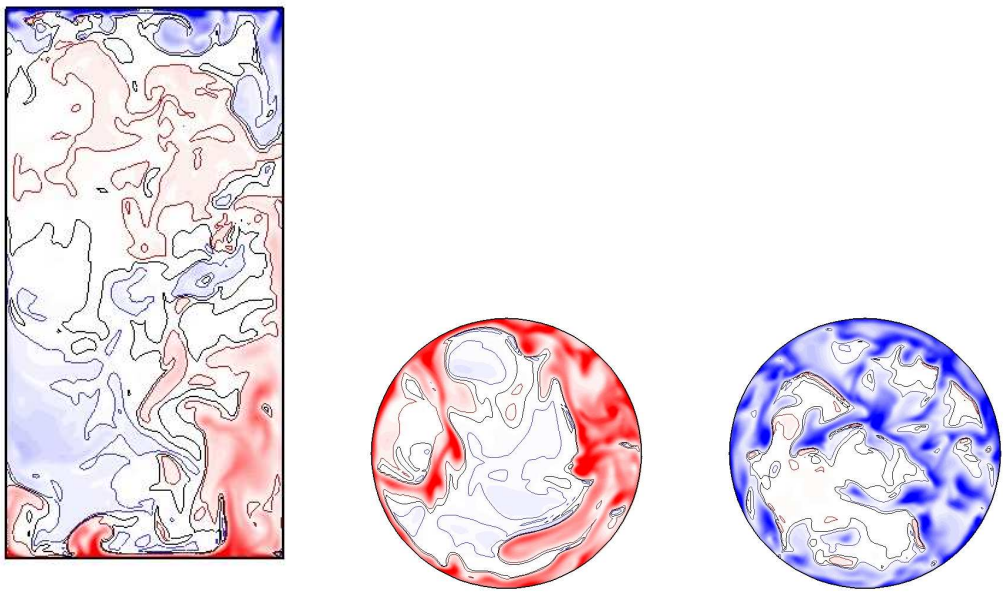

(a) (b) (c)

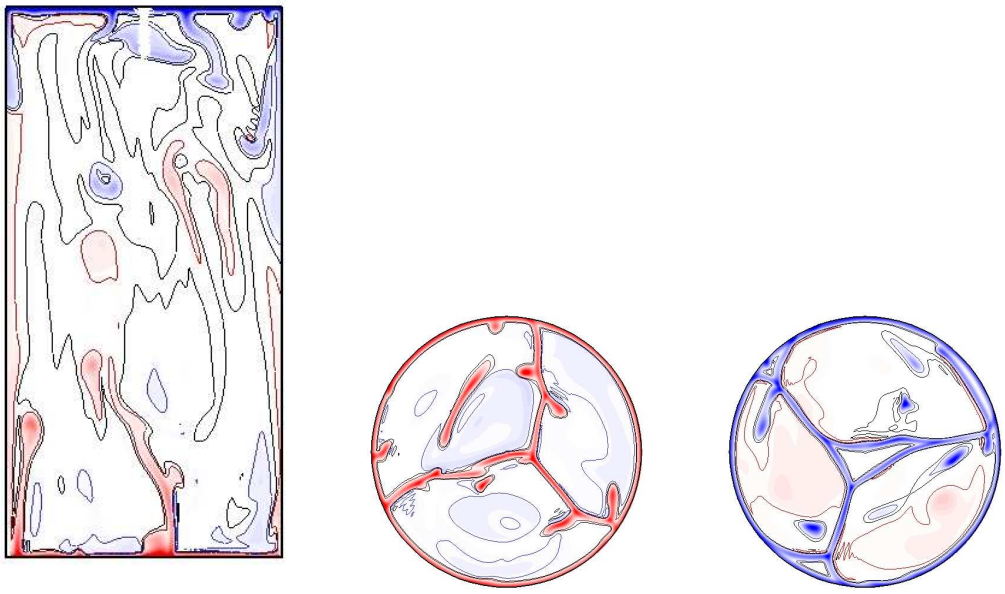

(d) (e) (f)

Figure 5.8: Flow structures at $Ra = 10^9$ and $Pr = 1$ (top), and $Pr = 10^3$ (bottom). (a),(d) A vertical section; (b), (e) horizontal sections close to the bottom plate; (c), (f) horizontal sections close to the top plate. Notation as in fig. 5.7.

Chapter 6

Nusselt number

6.1 Introduction

The Nusselt number (Nu) is the non-dimensional measure of the actual heat flux through the cell. It represents the response of the system to the temperature difference applied between the top and bottom plates. It is therefore considered the one of most important quantities in thermal convection problems.

In particular, the Nusselt number is the ratio by which the heat flux is enhanced with respect to the conductive value. Thus, it measures the effectiveness in the heat transfer of the convective system with respect to the same system at rest.

A principal aim in the studies on thermal convection is to determine the relation $Nu = f(Ra, Pr)$. This relation is as fundamental as the skin friction relation with respect to the Reynolds number for the classical pressure-driven flows.

After the onset of motion, the heat flux crossing the cell increases so fast with increasing Ra that a power-law behavior of Nu with respect to Ra is suggested:

$$Nu = ARa^{\alpha}. \tag{6.1}$$

However, this power law cannot be assumed as universal, because of the dependence of the coefficients A and α on the non-dimensional parameters Pr and Γ, and on Ra itself.

The prediction of a correct scaling-law for Nu (if indeed there is one) is a problem extensively studied from a theoretical point of view. A class of arguments refers to the mixing layer theory (see [68] for a review). In this theory the assumption of a single temperature and velocity scale as a function of the distance to the nearest boundary is used to balance

the momentum and energy equations.

By applying the mixing layer theory, Kraichnan [44] derived $Nu \sim Ra^{1/3}$ (high Pr) and $Nu \sim (PrRa)^{1/3}$ (low Pr) in a low-Ra zone. For high Ra, instead, he predicted $Nu \sim \left[PrRa/(lnRa)^3\right]^{1/2}$ (low Pr), and the same times $Pr^{-3/4}$ for high Pr. This relation at fixed Pr eventually becomes $Nu \sim Ra^{1/2}$ for Ra increasing to infinity (the so-called *ultimate regime*).

A variant of the mixing layer theory, motivated by experimental results [36], presumes an intermediate zone, or mixing zone, between the thermal boundary layer and the bulk zone. From this model it follows that $Nu \sim Ra^{2/7}$ [18]. Considering also the Pr dependence, it was derived $Nu \sim (PrRa)^{2/7}$ (low Pr) [23], and $Nu \sim Ra^{2/7}Pr^{-1/7}$ (high Pr) [82].

The last prediction was previously obtained by Shraiman and Siggia [67], who introduced the large-scale circulation in a model for high Pr flows. In this model the thermal boundary layer was assumed contained in the viscous sub-layer of a turbulent boundary layer, which is induced by the large-scale flow. In this sub-layer a linear velocity profile was assumed.

Another model essentially based on the presence of a large scale roll, which forces Prandtl-Blasius-like boundary layers, is that of Grossmann and Lohse ([32], [33]). They identify four main regimes in the $Ra - Pr$ space, depending on whether the boundary layer or the bulk dominates the thermal and kinetic energy dissipation rates. Using these arguments they derived different behaviors of Nu with respect to Ra and Pr in different Ra and Pr intervals.

These different theories seem to meet experimental and numerical data only in limited intervals of Ra and Pr, and for specific Γ. Besides, they generally present inconsistencies when checked in details. However, all these models predict some dependence on Pr for high-Pr regimes, but this dependence is different for different models. With respect to Ra and for moderate Rayleigh numbers, an important prediction is[1] predictions are $Nu \sim Ra^{2/7}$ at lower Pr and $Nu \sim Ra^{1/3}$ at higher Pr. Our results show consistencies with these expectations.

In the following parts we report the detailed behavior of Nusselt number with respect to Ra and Pr, in the Ra and Pr ranges explored by our simulations ($10^5 \leq Ra \leq 10^9$ and $10^{-1} \leq Pr \leq 10^4$). The results are compared to recent numerical and experimental work.

[1]The exponent 2/7 was found at $Pr \sim 1$ in experiments ([36], [21], [23]), and numerical simulations ([40], [77], [78]). The exponent 1/3 is consistent with upper bounds analytically derived for Pr approaching to infinity. In particular, in the infinite Prandtl number limit, a recent result is $Nu \leq 0.644 \times Ra^{1/3}(lnRa)^{1/3}$ as $Ra \to \infty$ [26]. For large but finite Pr it was found $Nu \leq Ra^{1/3}(lnRa)^{2/3}$ under the condition $Pr > cRa$, where c is a constant of order unity [80].

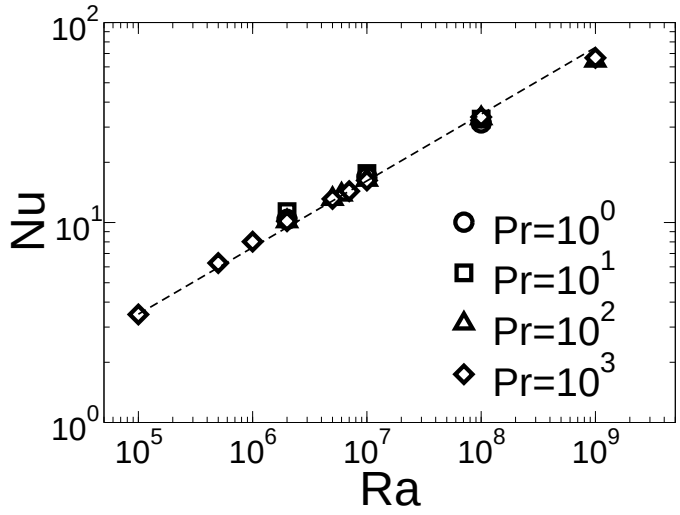

Figure 6.1: Nusselt number versus Rayleigh number. The dashed line represents a fit exponent of 0.309.

6.2 Nusselt number versus Ra and Pr

Experimental results of Niemela *et al.* [50] in a cell of aspect ratio $\Gamma = 1/2$, at $Pr \simeq 0.7$, and for Ra spanning over 11 decades, show a power-law exponent of 0.309. Our data seem to be consistent with these results (fig. 6.1), even if discrepancies arise when the Nusselt number is plotted in a compensated form (fig. 6.2). These discrepancies are not surprising, since in the range of Ra and Pr considered the flow passes through several transitional phases (see sec. 5.2), and a single power law is expected to be inadequate to describe the Nu scaling in different regimes [32].

The higher deviations have been found at $Pr = 1000$ (fig. 6.2(a)), and at $Pr = 1$ (fig. 6.2(d)). In the first case, for Ra before the transition from steady to unsteady flow ($Ra < 10^7$), the data are more consistent with a power law having exponent 1/3. This result agrees with previous data concerning the steady flow regime [36]. Instead, for $Ra \geq 10^7$, the better correspondence is with the exponent 0.309 mentioned above. As expected from a previous numerical work of Verzicco and Camussi [78], in the case of $Pr = 1$, the data show a power-law exponent closer to 2/7 for $Ra \leq 10^8$, which tends to a higher value for $Ra > 10^8$, perhaps close to 0.309. In [78] the scaling exponent for $Ra > 10^8$ was found to be closer to 1/3. In our case the two available values seem to be more consistent with the exponent 0.309 (fig. 6.2(d)), but they clearly are not enough to be significant.

The data are not sufficient to obtain precise values of the $Nu - Ra$ exponent in the differ-

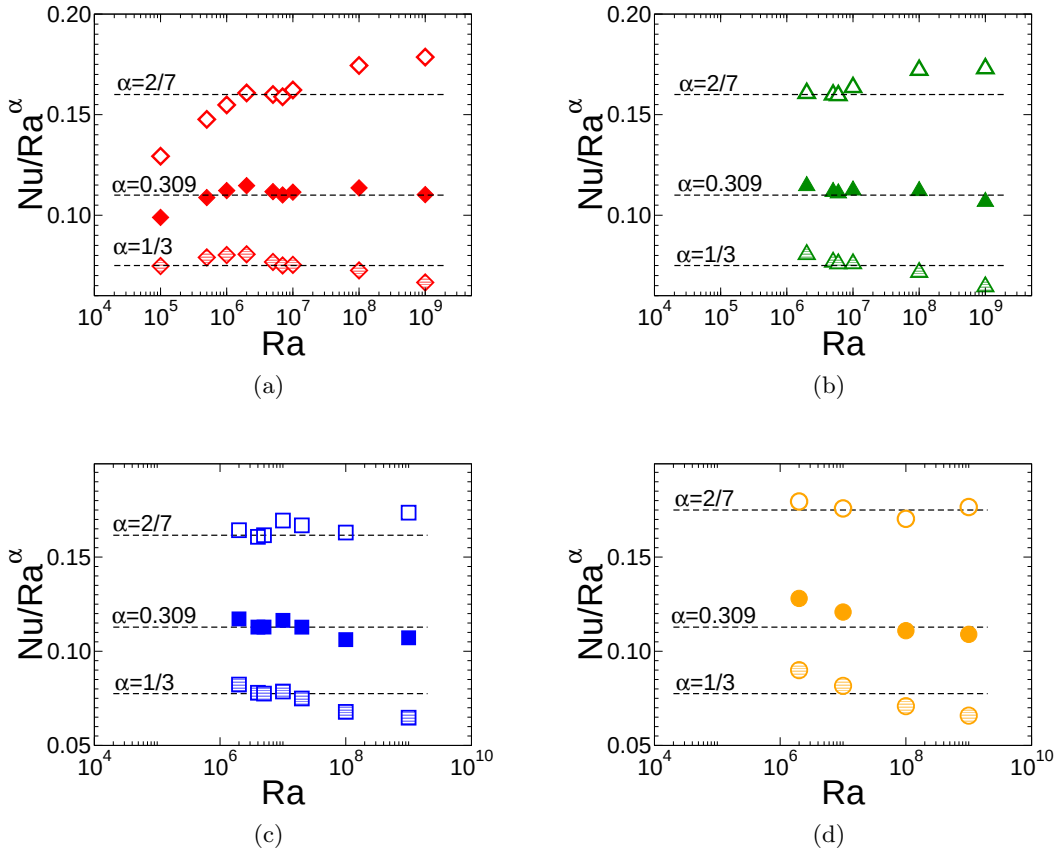

Figure 6.2: Nusselt number. (a) $Pr = 1000$, (b) $Pr = 100$, (c) $Pr = 10$ and (d) $Pr = 1$. The error-bars evaluated in sec. 3.2 are hidden by symbols.

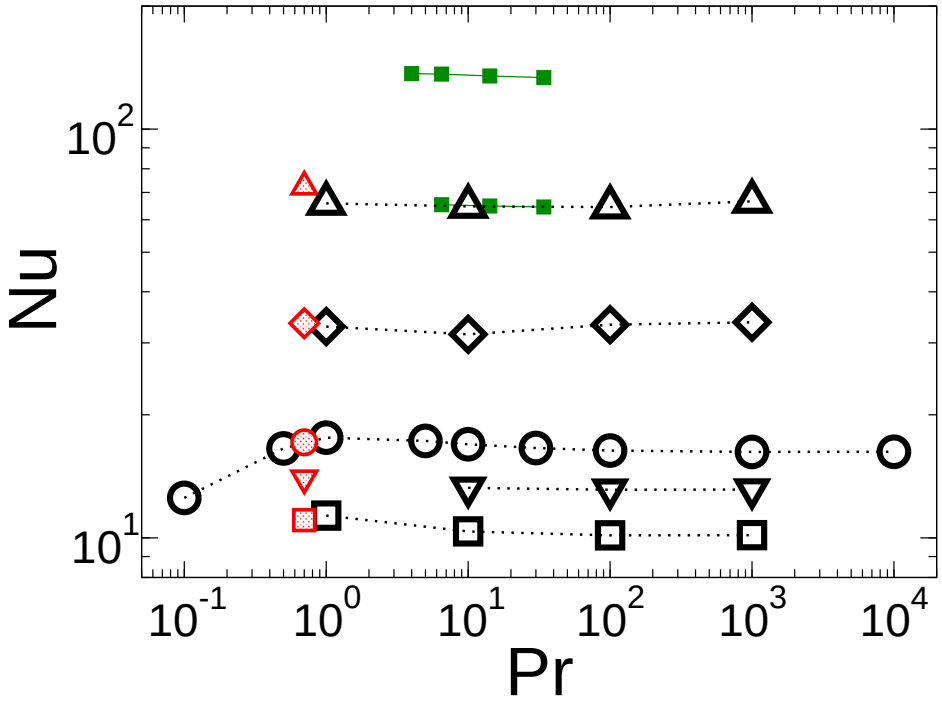

Figure 6.3: Nusselt number. Upright triangles: $Ra = 10^9$, diamonds: $Ra = 10^8$, circles: $Ra = 10^7$, inverted triangles: 5×10^6 and squares: 2×10^6. Red symbols extrapolated from [78]. Green symbols from [2]. The error-bars evaluated in sec. 3.2 are hidden by symbols.

ent regimes. However the approximate value of 0.31 evaluated for the unsteady simulation at higher Pr is also consistent with previous experimental results performed in similar Ra and Pr ranges ([81], [2]).

In the case of the dependence of Nu on Pr, fig. 6.3 shows the trends of the data at fixed values of Ra. The Nusselt number for $Pr \gtrsim 1$ is essentially independent of Pr. At $Ra = 10^9$ the deviations from a constant value are less than 3.5%, comparable to the error-bars (see sec. 3.2). These results agree with the experimental data of Ahlers and Xu [2] (green squares in fig. 6.3). For lower Ra the deviations increase as one approaches $Pr = 1$. However, they do not exceed 10%. At $Ra = 10^7$, the $Nu - Pr$ trend shows a small overshoot, while passing from low to high Pr regimes. A similar finding is shown in [33]. The slope at $Pr < 1$ is consistent with the exponent 0.14 found in [77].

The independence of Nu with respect to Pr found in our simulations at $Ra = 10^9$ does not agree with the experimental results of Xia *et al.* [81], obtained in a cell of aspect ratio $\Gamma = 1$ at similar Ra and Pr regimes. These results show a slightly decrease of Nu with increasing Pr, in agreement with the Grossmann and Lohse predictions [33]. However, a slightly different behavior of Nusselt number in the cell of $\Gamma = 1$ with respect to the cell of $\Gamma = 1/2$ was already found in the dependence of Nu versus Ra [52].

Chapter 7

Boundary layers and vertical profiles

7.1 Introduction

The interaction of the flow with the boundaries generates viscous boundary layers on all the walls of the convective cell and a thermal boundary layer occurs on top and bottom plates. The boundary layers are characterized by time-averaged profiles in the direction perpendicular to the boundaries. In particular, profiles of velocity field characterize the viscous boundary layer, and temperature profiles describe the thermal boundary layer.

In thermal convection, temperature and velocity fields are coupled, the temperature being an active scalar. In these conditions, a comprehensive boundary layer theory does not exist. Nevertheless, almost all the proposed models concerning the Rayleigh-Bénard convection are essentially based on boundary layer theories ([44], [18], [67], [32]). In the case of laminar flows, some similarity solution for temperature-velocity coupled boundary layers has been proposed [63], but usually Prandtl-Blasius-like solutions are expected [32]. A direct study of boundary layers is therefore essential to investigate their features [1].

Boundary layer analysis is extremely complex due to the presence of plume detachments and various large scale circulations leading to different mean flow structures at different regimes of Ra and Pr (see sec. 5.3.1). The boundary layer thicknesses as well as the profiles of mean quantities and fluctuations are strongly dependent on the position along the plates, not only relative to the walls, but also relative to the mean flow motion. As a consequence, the local boundary layers generally differ also between top and bottom plate.

The evaluation of boundary layer thickness at a fixed position on the bottom plate, as done often in laboratory experiments, cannot produce significant results in general. To partially overcome this issue (especially in order to compare the results at different Ra and Pr regimes), area-averaged profiles can be considered instead of locally time-averaged quantities. From a theoretical point of view, the horizontal area-averaged profiles are of main interest, because they are strongly characterized by symmetry, and show exact analytical relationships that are generally used in the models[1].

On the other hand, for a cell of small aspect ratio, the area-averaged profiles are expected to significantly differ from the local profiles, with consequently different scaling of local and global boundary layer thicknesses[2]. However, the more homogeneous the flow, the more similar the global and local profiles.

An investigation on global-local features of velocity profiles and viscous boundary layer thicknesses is presented in the next section together with similar features of temperature profiles. Section 7.3 discusses the scaling behavior of profiles and boundary layers with respect to Ra and Pr and with respect to Re and Pe.

In the following sections the quantities are made non-dimensional according to form (4.1). In particular, the thicknesses are measured in terms of cell height h, and the velocities in terms of characteristic velocity $V = \sqrt{\alpha g \Delta T h / Pr}$ (for detail see chapter 4).

7.2 Local versus global features of vertical profiles

The time-averaged profiles and the corresponding boundary layers are features of the mean flow structure - that is, the time-average of the flow fields. In presence of different mean flow structures and flow separations inside the boundary layers it is not easy to compare local profiles and to evaluate local boundary layer thicknesses. For this reason, area-averaged profiles, uniquely defined, are preferred in data analysis. The issue is to understand if the global profiles can represent local features. In the range of Pr and Ra numbers explored in this work, different kinds of mean flow structures have been found (see section 5.3.1 for details). In particular, at lower Pr ($Pr < 100$) the mean flow generally consists of two axisymmetric, opposite, toroidal structures, with the flow moving from the central axis towards the sidewall along the horizontal plates (see figs. 7.1 (top) and 5.7). For higher

[1] See for example the relations (3.2) and (3.2) which link the Nusselt number to the thermal boundary layer thickness based on the tangent to the global temperature profile.

[2] Note that the global boundary layer thickness δ based on the area-averaged profiles is generally not equal to the area-average of the boundary layer thicknesses $\lambda(\theta, r)$ calculated on corresponding local profiles: $\delta \neq \langle \lambda(\theta, r) \rangle_A$.

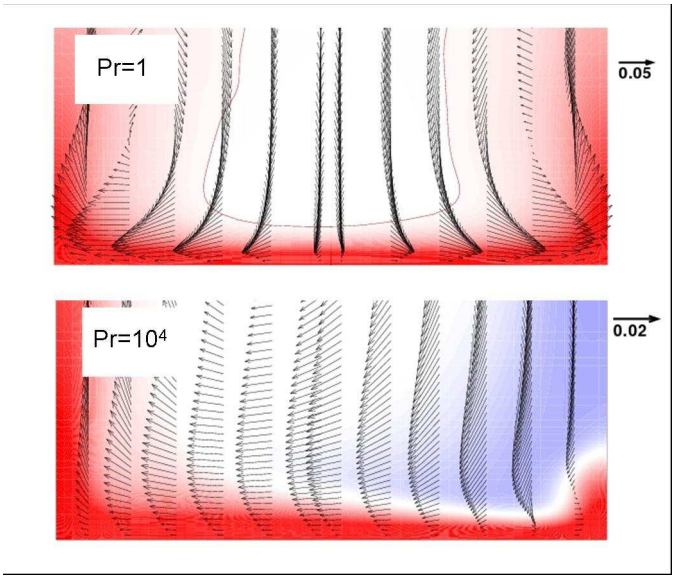

Figure 7.1: Examples of velocity vectors close to the bottom plate. Top: axisymmetric mean flow structure at $Ra = 10^7$ and $Pr = 1$. Bottom: single-roll mean flow structure at $Ra = 10^7$ and $Pr = 10^4$. The arrows represent the velocity vectors tangent to the section. Their reference strength is represented by a fraction of the convective velocity $U_c = U/\sqrt{Pr}$, where U is the free-fall velocity.

Pr ($Pr \geq 100$) the resulting mean flow breaks the axisymmetry. At $Ra < 10^8$ the flow is mainly characterized by a single-roll structure (fig. 4.1), which splits in two-rolls or more complex structures at $Ra \geq 10^8$. Considering the single-roll structure in a vertical section relative to the maximum circulation developed, the flow moves, close to the bottom plate, from one sidewall edge to another, and in the opposite direction close to the top plate (fig. 7.1 (bottom)). In the case of the two-roll structure, instead, the flow mainly moves from the sidewall to the center at the bottom and from the center to the sidewall at the top (fig. 5.7).

Figure 7.2 shows local horizontal velocity profiles (time-average only) belonging to the vertical section relative to maximum circulation development at various radial positions, in comparison to the area-averaged profile (black solid line). In particular, the first row graphs (figs. 7.2(a) and 7.2(b)) correspond to the axisymmetric toroidal structure at $Ra = 10^8$ and $Pr = 1$. The second row (figs. 7.2(c) and 7.2(d)) corresponds to the two-roll structure ($Ra = 10^8$ and $Pr = 10^3$). And the last row (figs. 7.2(e) and 7.2(f)) corresponds to the single-roll structure at $Ra = 10^7$ and $Pr = 10^3$. Figure 7.3 shows the relative rms profiles.

From these plots it is evident that only for the axisymmetric structure the area-averaged velocity profiles well represent the corresponding typical local profiles. In these cases as well, reasonable similarity has been found in the profiles inside the boundary layers (figs. 7.2(b) and 7.3(c)).

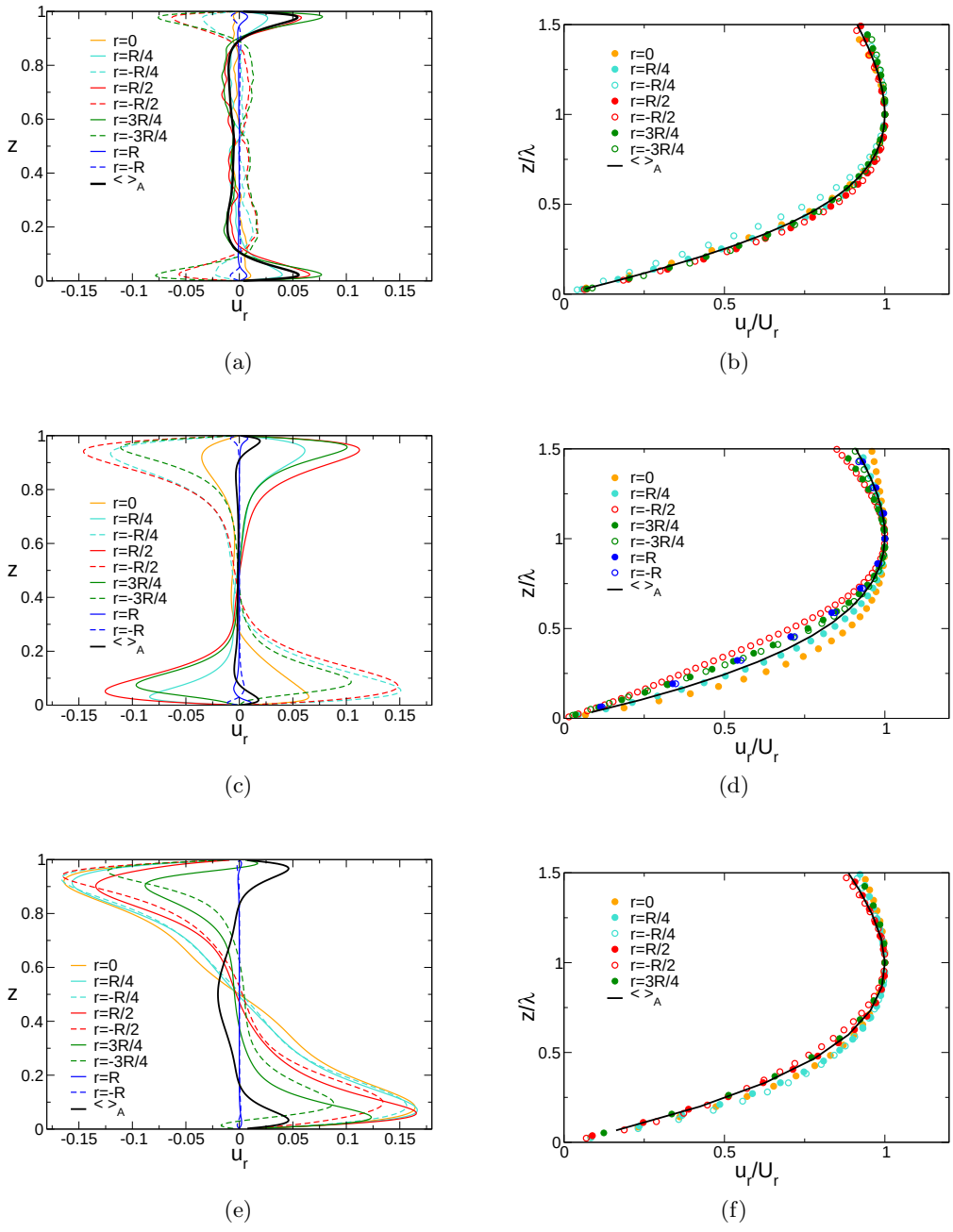

Figure 7.2: Local horizontal velocity profiles compared to the global one. (a) and (b) are for $Ra = 10^8$ and $Pr = 1$; (c) and (d) for $Ra = 10^8$ and $Pr = 10^3$; (e) and (f) for $Ra = 10^7$ and $Pr = 10^3$. In (b), (d) and (f) the profiles are normalized with respect to their maximum velocity and the corresponding height. In the legends $r = R$ means $r \simeq \pm R$ (at $r = \pm R$ the velocity profiles are zero).

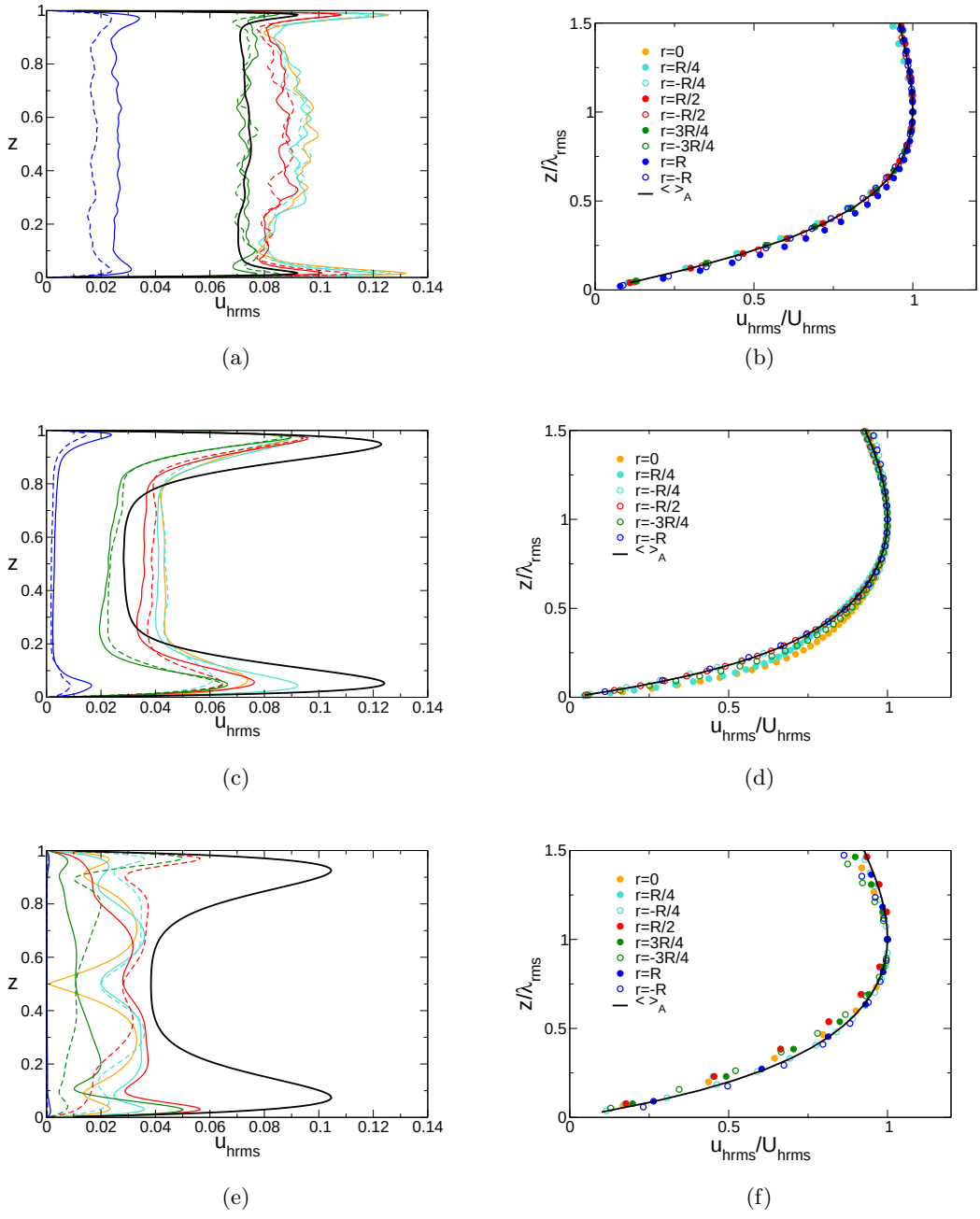

Figure 7.3: Local rms profiles of horizontal velocity compared to the global one. Notations are the same as in fig. 7.2.

The somewhat poorer correspondence between local and global profiles in other simulations is mainly due to two adverse factors. One is that the Reynolds number is low (high Pr). Consequently, the boundary layers are not well-developed and the flow is strongly affected by boundary effects. The situation is worse when multi-cell structures are present. In these cases generally no similarity has been found in boundary layer profiles (figs. 7.2(d) and7.2(f)). In spite of this, the global profiles close to the plates have been found quite similar (in shape) to the typical local profiles (i.e., profiles far to boundaries and flow inversions). A similar correspondence has been also found for rms profiles, where the local and global quantities are not linearly related[3].

The other negative factor is that, when the flow shows opposite circulations, averages in the horizontal plane are diminished by cancellation. In this case the area-averaged velocity profile tends to disappear. However, it can be substituted by the corresponding rms profile, which better represents the local velocity profiles especially for higher Pr, for which the fluctuating velocities are negligible with respect to the mean flow.

As a consequence, in order to define a viscous boundary layer thickness based on a global velocity profile and valid for all the simulations, the rms of the area-averaged horizontal velocity has to be taken into account. The question is how this thickness is related to different definitions of the local thickness.

Figure 7.4 shows thickness distributions corresponding to the maximum of local horizontal velocity profiles ($\lambda(r, \pm\theta_0)$: black circles) and of the local rms horizontal velocity profiles ($\lambda_{rms}(r, \pm\theta_0)$: red squares) close to the bottom plate, for the same simulations and in the same vertical sections of figs. 7.2 and 7.3. These distributions are compared to the λ averaged value[4] ($\langle\lambda\rangle_r$: black dashed line) and to the global boundary layer thicknesses δ and δ_{rms}, respectively based on the maximum of the area-averaged horizontal velocity profile (black solid line), and of the area-averaged horizontal velocity rms profile (red dashed line).

Figure 7.4(a) shows for the simulation with toroidal structure ($Ra = 10^8$ and $Pr = 1$) that λ diverges close to the axis, while λ_{rms} is more stable. Their average values are basically the same as the corresponding global boundary layer thicknesses: $\langle\lambda\rangle_r \simeq \delta$ and $\langle\lambda_{rms}\rangle_r \simeq \delta_{rms}$. At higher Pr the picture is more complex, since the local thicknesses strongly vary along the plate, and the area-averaged horizontal velocity profiles almost vanish (see figs. 7.2(c) and 7.2(e)). However there is generally a satisfactory correspondence between

[3]The rms of a general quantity x is defined as: $rms\,\langle x\rangle = \sqrt{\langle x^2\rangle - \langle x\rangle^2}$. Therefore, the rms calculated averaging only in time is different from that including a horizontal average ($rms\,\langle x\rangle_t \neq rms\,\langle x\rangle_{t,A}$).

[4]On averaging the local thicknesses, the anomalous values found close to the sidewall and in the presence of strong inversions have been excluded.

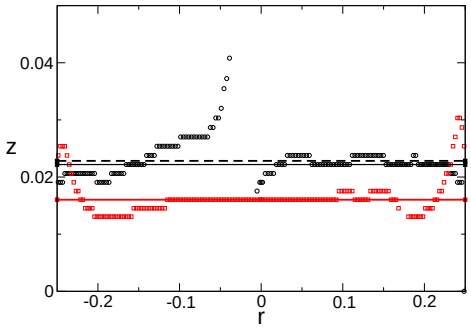

(a)

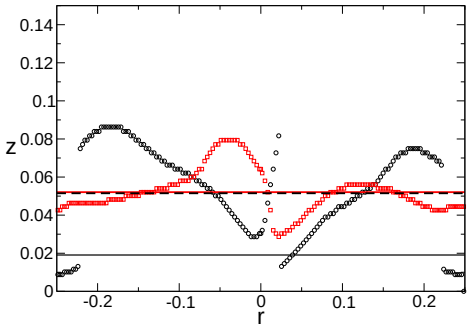

(b)

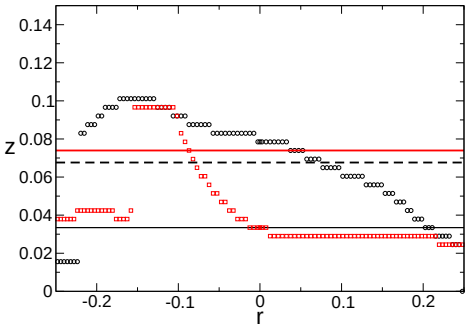

(c)

Figure 7.4: Viscous boundary layer thicknesses distribution along the bottom plate. Black circles: $\lambda(r, \pm\theta_0)$; red squares: $\lambda_{rms}(r, \pm\theta_0)$; $\pm\theta_0$ represents the vertical section corresponding to the maximum development of the mean flow circulation. Black dashed line: $\langle\lambda\rangle_r$; black solid line: δ; red dashed line δ_{rms}. (a) $Ra = 10^8$ and $Pr = 1$; (b) $Ra = 10^8$ and $Pr = 10^3$; (c) $Ra = 10^7$ and $Pr = 10^3$.

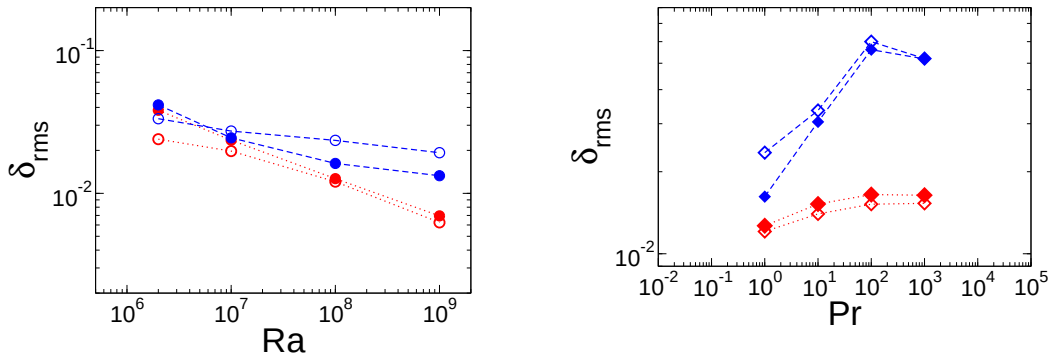

(a) (b)

Figure 7.5: Global boundary layer thicknesses (filled symbols) compared to the local ones (open symbols). Filled blue symbols: δ_{rms}; open blue symbols: $\langle\lambda\rangle_r$; Filled red symbols: δ_{Trms}; open red symbols: $\langle\lambda_{Trms}\rangle_r$. (a) Fixed $Pr = 1$; (b) fixed $Ra = 10^8$.

the global rms thickness and the mean value of the local maximum-velocity thickness: $\langle\lambda\rangle_r \simeq \delta_{rms}$.

Figure 7.5 shows the averaged local thickness $\langle\lambda\rangle_r$ (blue open symbols) compared to the global rms thickness δ_{rms} (blue filled symbols), at fixed $Pr = 1$ and varied Ra (fig. 7.5(a)), and at fixed $Ra = 10^8$ and varied Pr (fig. 7.5(b)). In the first case the two viscous boundary layer thicknesses generally differ in width (discrepancies around 8%). However, at higher Ra, when the velocity fluctuations become quite strong, they are close to each other, at least up to $Ra = 10^9$. At higher Pr no significant discrepancies have been found between the Ra-trends of the two definitions. In particular, in the simulations at $Pr = 10^3$, we found that δ_{rms} differs from $\langle\lambda\rangle_r$ by less than 3%. At fixed Ra and increasing Pr the trends are also qualitatively the same (see fig. 7.5(b)).

From this analysis, we conclude that, at higher Pr, the global thickness δ_{rms} well represents the local viscous boundary layer thickness λ based on the maximum horizontal velocity profiles. At $Pr \sim 1$, δ_{rms} over-estimates λ, but the two thicknesses follow the same trend at sufficiently high Ra. Given the higher reliability in the practical calculation, in following analyses we will consider the height (δ_{rms}) to represent the viscous boundary layer thickness.

Similar analysis has been performed for the thermal boundary layer thicknesses. In particular, we compared the local thermal boundary layer thicknesses based on the maximum of the local temperature rms profiles (λ_{Trms}) to the corresponding global one (δ_{Trms}). In this case we generally found a satisfactory agreement between the two thicknesses, since the Pe numbers generally are sufficiently high (typically $Pe > 10^3$) and, consequently, the thermal

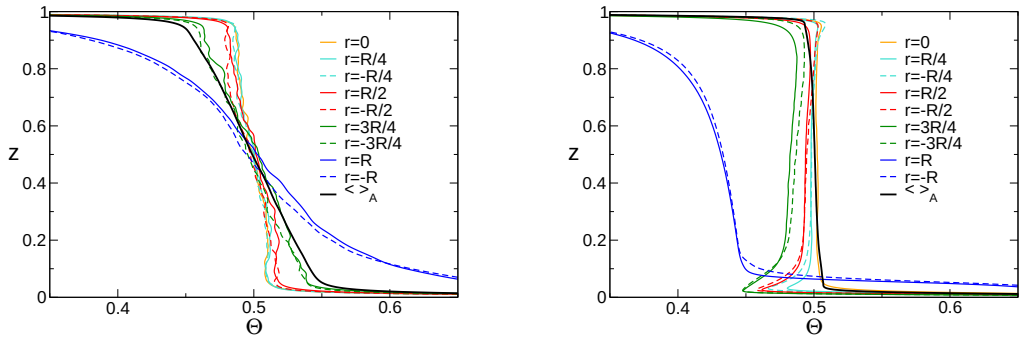

(a) (b)

Figure 7.6: Local temperature profiles compared to the global one. (a) $Ra = 10^8$ and $Pr = 1$; (b) $Ra = 10^8$ and $Pr = 10^3$.

boundary layers are well-developed. Indeed we generally found λ_{Trms} to be quite uniform along the plate, except for a narrow region close to the sidewall. The higher discrepancies are at $Pr = 1$ and lower Ra, when the Pe numbers are the smallest[5] (see fig. 7.5).

For the same reason as above, we will consider the global value δ_{Trms} the temperature boundary layer thickness, instead of the local thickness.

With respect to temperature, an important feature of the local profiles is the presence of inversions in their slope at high Pr numbers. This feature generally is not visible in corresponding global profiles (see fig. 7.6). Inversions close to the plates indicate that, as Pr increases, larger parts of hot (cold) fluid are able to reach the cold top (hot bottom) plate, without a significant cooling (heating) effect. The explanation of this important phenomenon has been already given in section 5.3.1. In this context, we simply underline that the global temperature profiles generally are not able to capture this feature.

7.3 Vertical profiles and boundary layers as functions of Ra and Pr

The global (time and horizontal-area average) profiles of velocity and temperature fields are not sufficient to describe all the details of the convective system. They are, however, able to capture its fundamental features. In particular, the temperature and horizontal velocity rms profiles, together with the vertical velocity rms profiles, indicate the strength of flow fluctuations along the vertical direction. Besides, they give a measure of thermal and

[5]The behaviors of Peclet and Reynolds numbers are discussed in section 4.4

viscous boundary layer thickness, as shown before. As a consequence they indirectly reveal the presence of these boundary layers and therefore of large scale circulations.

Significant indications derive from the global temperature profile, which, by mean of its slope while approaching top and bottom plates, shows immediately the higher heat transfer efficiency of a convective system with respect to the same system at rest[6]. The temperature profiles show that the system organizes itself in such a way that the most effective temperature gradients remain confined in thin regions near the top and bottom plates. These regions are the thermal boundary layers, in which the diffusive dynamics prevail over (or are comparable to) the advective ones. This implies that the presence of thermal boundary layers represents a fundamental feature of a convective mechanism.

Less fundamental seems the role of the viscous boundary layers. Indeed, even imposing free-slip conditions to all the walls, convective phenomena still occur without significantly changing their characteristics[7] [75]. However, a viscous boundary layer develops when there are no-slip conditions on the plates. Its main effect is a reduction in the heat transfer efficiency (see fig. 2 in [75]). This implies that the viscous boundary layer influences the slope of temperature profile at wall, and therefore the thermal boundary layer behavior.

In the following part (sec. 7.3.2) we examine the relationship between viscous and thermal boundary layers by comparing their thickness for varied Ra and Pr. Before doing this, we show the global behavior of the velocity and temperature profiles.

7.3.1 Global profiles

Figure 7.7 shows the global rms profiles of the horizontal velocity at fixed $Pr = 1$ and increasing Ra (figs. 7.7(a) and 7.7(c)), and at fixed $Ra = 10^9$ and increasing Pr (figs. 7.7(b) and 7.7(d)). These profiles vary from one flow regime to another, depending on the mean flow structures, and on Ra and Pr. In agreement with expectations, they generally tend to peak much closer to the plates as Ra increases and Pr decreases (that is, Re increases). However, they do not show a constant shape close to the plates, either in terms of Pr (fig. 7.7(d)), or in terms of Ra (fig. 7.7(b)). In the latter case no similarity has been found even at $Pr = 1$, when the mean flows show similar large scale structures and the local profile shapes are similar to each other [8] (fig. 7.3(b)). This is in contrast to experimental results shown

[6]This efficiency is measured by the Nusselt number (Nu). We recall that the slope of the global temperature profile at top (bottom) plate is equal to Nu (see eq. (3.1))

[7]Strong gradients in the horizontal velocity fluctuations seem to be fundamental for an efficient heat transfer. These gradients are also present with free-slip conditions [75].

[8]We have found the same results for mean velocity profiles instead of velocity rms profiles. Even comparing the local horizontal velocity profiles at a fixed position ($r = R/2$ and $\theta = \theta_0$) no Rayleigh number similarity has been found at fixed $Pr = 1$.

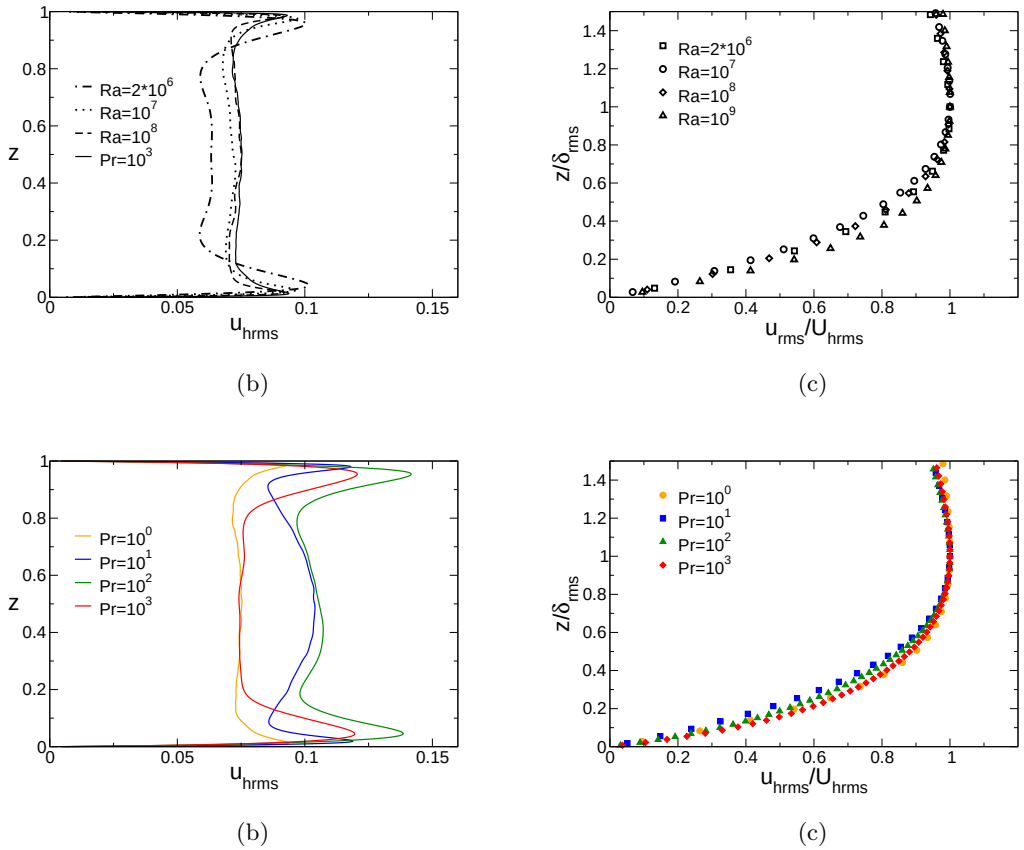

Figure 7.7: Global rms profiles of horizontal velocity. (a) and (b): fixed $Pr = 1$; (c) and (d): fixed $Ra = 10^9$.

in [46], concerning a cylindrical cell of aspect ratio one. In spite of the higher regularity of temperature rms profiles (fig. 7.8), no similarity has been found even there.

Figure 7.9 shows the global temperature profiles at $Pr = 10^3$ and increasing Ra (top), and at $Ra = 10^9$ and increasing Pr (bottom). The profiles in the central part become steeper as Ra or Pr increases. The bulk region happens to be essentially isothermal on the average, especially at the highest Ra and Pr (slope almost zero at the profile centerline at $Ra = 10^9$ and $Pr = 10^3$). It seems that an inversion of the slope at the centerline appears at higher values of Ra and Pr (see top right inset in plots of fig. 7.9). However, in the range of Ra and Pr considered, a negligible inversion of the global temperature slope has been found only closer to the plates at $Ra = 10^9$ and $Pr = 10^3$. Different is the case of local temperature profiles, as already shown in the previous section.

An evident difference between the temperature profiles at increasing Ra and those at increasing Pr concerns the temperature profile slopes near the top and bottom plates. In-

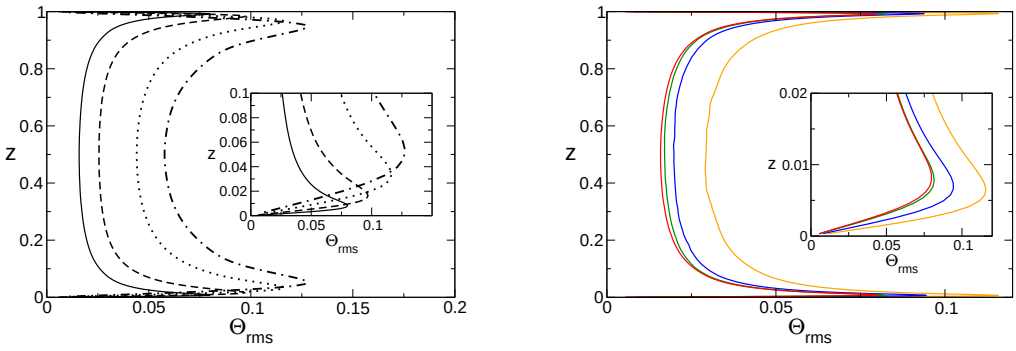

Figure 7.8: Global rms profiles of temperature at $Pr = 10^3$ and increasing Ra (a), and at $Ra = 10^9$ and increasing Pr (b).

deed, when Ra increases the slope of temperature profiles at the plates decreases (fig. 7.9(a) bottom inset), implying that the temperature gradients are more effective with increasing Ra (i.e. Nu increases with Ra). On the contrary, when Pr increases the slope is practically unchanged (fig. 7.9(b) bottom inset), implying that the temperature gradients and consequently the heat transport[9] are almost the same at different Pr.

Finally, figure 7.10 shows the typical behavior of the global rms profiles of the vertical velocity. It is worth noting that the global profiles of the vertical velocity fluctuations are directly linked to the corresponding temperature and pressure profiles through the following equation:

$$\frac{\partial}{\partial z}\left\langle w^2\right\rangle_A = -\frac{\partial}{\partial z}\left\langle p\right\rangle_A + \left\langle \Theta\right\rangle_A + \frac{1}{\sqrt{Ra}}\oint_{\partial A}\nabla w \cdot d\vec{l}, \tag{7.1}$$

where the last term represents the friction in the vertical direction integrated along the sidewall contour of the horizontal section A. However, this term is generally negligible, and it disappears in case of periodic conditions at the sidewall or for fluid layer infinitely extended in the horizontal direction.

Eq. (7.1) has been derived by averaging on the horizontal area eqs. (4.1). It shows that the profile of the vertical velocity fluctuations is arranged in such a way to balance, on the average, the pressure difference between the bottom plate and the generic section A, and to balance also the integral of the temperature profile (representing the buoyancy forces acting, on the average, in the volume below section A).

Eq. (7.1) is valid at each instant of time, since $\langle w\rangle_A$ is zero at each time because of mass conservation. This means that the relation among the profiles of vertical velocity

[9] A general view of the Nusselt number behavior in the range of Ra and Pr simulated will be given in chapter 6.1

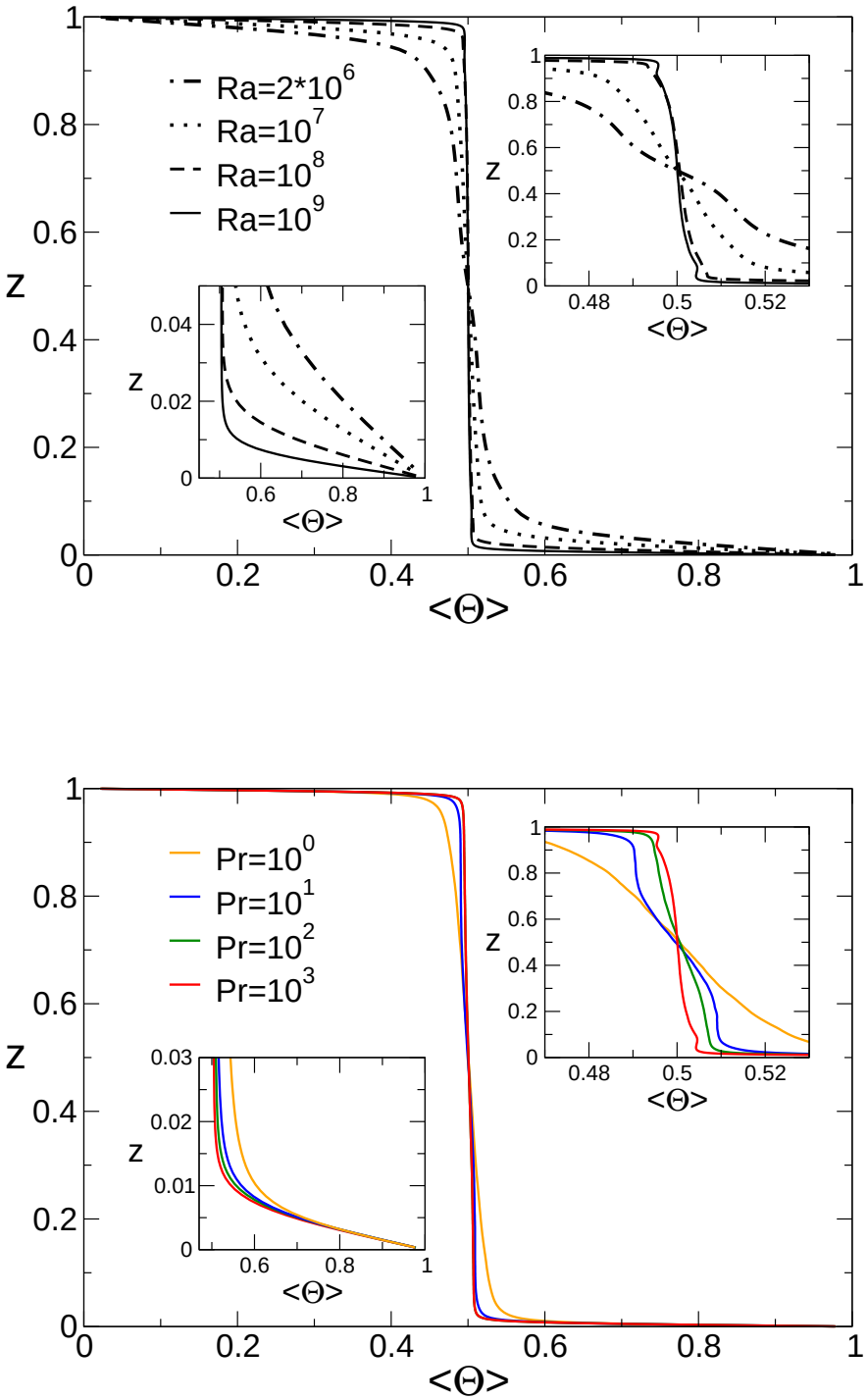

Figure 7.9: Global temperature profiles at $Pr = 10^3$ and increasing Ra (top), and at $Ra = 10^9$ and increasing Pr (bottom).

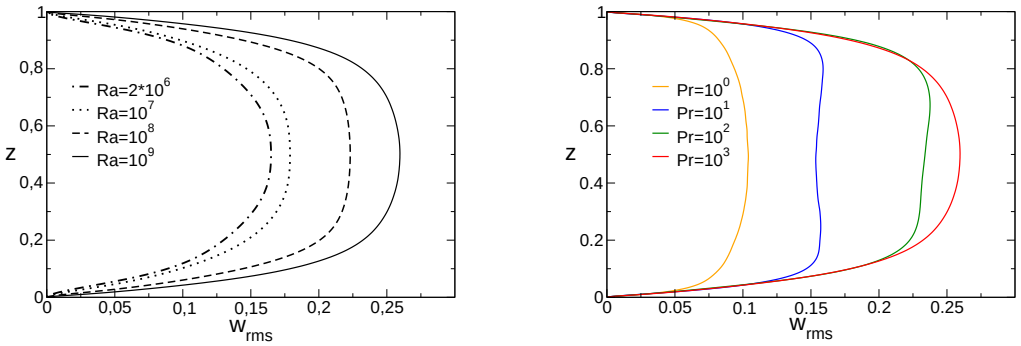

Figure 7.10: Global rms profiles of vertical velocity at $Pr = 10^3$ and increasing Ra (a), and at $Ra = 10^9$ and increasing Pr (b).

fluctuations, pressure and temperature evolves in time only implicitly.

7.3.2 Boundary layer thicknesses

Low sensitivity to the Prandtl number has been found in the thermal boundary layer thicknesses for $Pr > 1$, as shown in figure 7.11 (red symbols). In particular, they slightly increase, approaching a constant value as Pr increases. This behavior disagrees with the common expectation that the thermal boundary layer thickness should decrease as Pr increases. The commonly expected behavior is that the thermal boundary layer thickness is inversely related to the Pe number, and the Pe number is expected to increase as Pr increases. In our simulations we found that the Pe number at most slightly increases with Pr (figs. 4.8(b) and 4.8(d)).

The increasing behavior of the thermal boundary layer thickness with Pr (for $Pr > 1$) could be due to uncertainties in the definition of Pe and of thermal boundary layer thickness. However, checks on thermal boundary layer thicknesses based on other definitions show the same increasing trends with Pr.

A probable explanation of this result is that the thermal boundary layer is dragged up by the viscous boundary layer, as it becomes thicker than the thermal boundary[10] (see fig. 7.11(b) for the strong discontinuity in the thermal boundary layer thickness trend just when the viscous boundary layer becomes thicker than the thermal one).

The viscous boundary layer thickness increases with Pr, in agreement with a fast decrease of Re with Pr (we found Re almost linearly depending on the inverse of Pr, see sec. 4.4).

[10]The idea that the viscous boundary layer, when thicker, governs the thermal one has been used widely ([44], [67], [32]).

At a given Pr, the viscous boundary layer thickness crosses[11] the thermal one, and, with increasing Pr, reaches a saturation value.

The saturation of the viscous boundary layer thickness is due to the fact that the viscous thickness cannot indefinitely grow as Re decreases (Pr increases), at least because the cell has a finite size [33]. Figure 7.13(a) shows the viscous boundary layer thickness as a function of Re. At lower Re, the scatter in the thicknesses around a saturation value (nearly 1/10 of the cell height) is mainly related to the presence of different mean flow structures found at different Ra and high Pr.

One would expect that the viscous thickness, when it saturates, reaches half of the cell per side. A saturation at 1/10 instead of 1/2 of cell height basically derives from the definition. The presence of a large scale circulation, even at very high Pr number, implies at least two peaks in the global horizontal velocity rms profiles, and thus a thickness[12] smaller than 1/2.

If the thermal boundary layer is driven by the viscous one, then its thickness should saturate as well, as it actually does. The Pe independence of Pr at sufficiently high Pr is consistent with the corresponding saturation of the thermal boundary layer thickness (and vice-versa).

It thus seems that the saturation of the viscous boundary layer, owing to a finite cell, induces a saturation on the thermal boundary layer thickness. This reflects the behavior of the Peclet number, which turns out to be independent of Pr. Consequently $Re \sim 1/Pr$. Thus Re strongly decreases with Pr, which implies a fast saturation[13] of the viscous boundary layer with increasing Pr.

At lower Pr, before saturation, the Peclet number increases slightly[14] with Pr (fig. 4.8(b)), therefore the thermal boundary layer thickness should tend to decrease with Pr, instead of increasing. On the other hand, there is an effect of the viscous boundary layer, which strongly increases with Pr and drags up the thermal boundary layer. Then, there are two opposite effects acting on the thermal boundary layer thickness: the Peclet number influence, which tends to drag it down, and the viscous boundary layer influence, which tends to drag it up. One of these two effects can prevail or they can balance each other.

[11] The crossing point tends to be at lower Pr for increasing Ra. This means that the Pr interval, in which the viscous boundary layer would influence the thermal one, increases with Ra.

[12] From one point of view the saturation of the thicknesses corresponding to peaks in horizontal velocity rms profiles indicates a saturation in the viscous boundary layer thicknesses. On the other hand it can be interpreted as a saturation in the vertical large scale circulation size. At higher Pr the large scale circulations tend to develop mainly in vertical direction, because of the higher buoyancy of the high-Pr fluid (see sec. 5.3.1). This means that the circulations tend to occupy all the available space in vertical direction. The saturation implies that they cannot reduce their vertical size below around 8/10 of the cell height.

[13] This implies a fast approach to the infinite Pr limit.

[14] The increase of Pe with Pr is not so fast, as one can expect away from saturation, because of a smooth approach to saturation related to the smoothness of the low Re dynamics.

In the Ra range simulated here, the viscous boundary layer effect slightly prevails over the Pe effect when the thermal boundary layer thickness is calculated using the temperature rms profile peaks. When the thermal boundary layer thickness is calculated using the tangent to the temperature profile (eq. (3.2)), the two effects mostly balance each other and the thermal boundary layer thickness becomes almost constant with Pr (fig. 7.14), even at $Ra = 10^9$ and $Pr \sim 1$ (far from saturation). As a consequence, the Nusselt number reflects the same trend (see chapter 6.1 for details on Nu).

At fixed Pr and increasing Ra, Re and Pe increase at the same rate by definition, and the viscous and thermal boundary layer thicknesses are generally expected to follow the same trend (if the Prandtl-Blasius theory [63] is considered). Figure 7.12 shows the viscous and thermal boundary layer thicknesses as a function of Ra. The high viscous thickness scatter at varied Ra and high Pr (figs. 7.12(a) and 7.12(b)) is due to the different mean flow structures, as already explained before[15]. The deviation of viscous thicknesses from thermal ones at high Pr is still due to the viscous thickness saturation with respect to Re (fig. 7.13(a)). However, in agreement with previous results ([78], [7]), we have found a difference between thermal and viscous thickness trends also at lower Pr (figs. 7.12(d) and 7.5(a)). This deviation at $Pr = 1$ seems to be a temporary effect, due to a difference in the mean flow structures, tending to disappear at $Ra > 10^{10}$ [78].

The exponent of a power law fitting the thermal boundary layer thicknesses versus Ra is approximatively equal to 0.3, if we consider the data at $Ra \geq 10^7$ for each fixed Pr.

Finally, figure 7.13(b) shows the behavior of thermal boundary layer thickness with respect to Pe at fixed $Pr = 10^3$. The two data trends inside the plot are evaluated using different typical velocities for Pe calculation.

[15]The large variety of mean flow structures found at different Ra generally does not allow one to obtain clear trends at fixed Pr and varying Ra. Instead, at fixed Ra and varying Pr, the data trends are generally smoother.

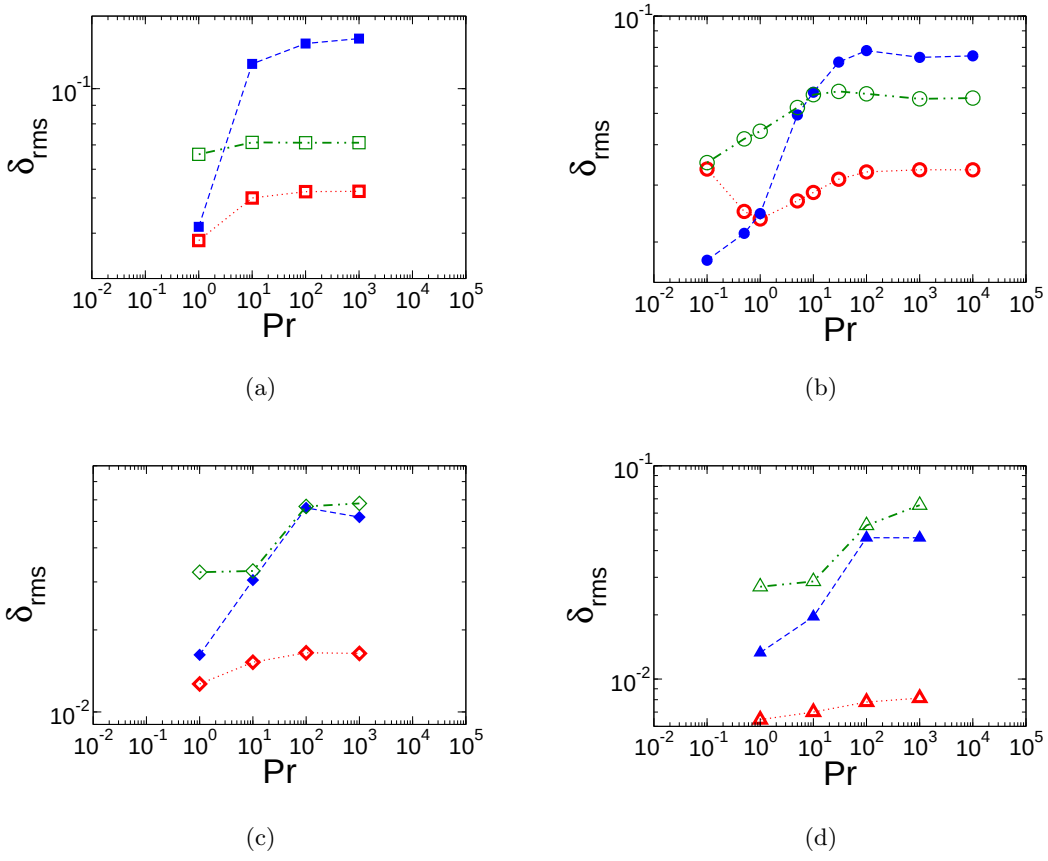

Figure 7.11: Boundary layer thicknesses based on rms profiles. (a) $Ra = 2{\cdot}10^6$, (b) $Ra = 10^7$, (c) $Ra = 10^8$ and (d) $Ra = 10^9$. Bold open symbol-dotted line: thermal boundary layer; filled symbol-dashed line: viscous boundary layer; thin open symbol-dot dashed line: viscous boundary layer on the sidewall.

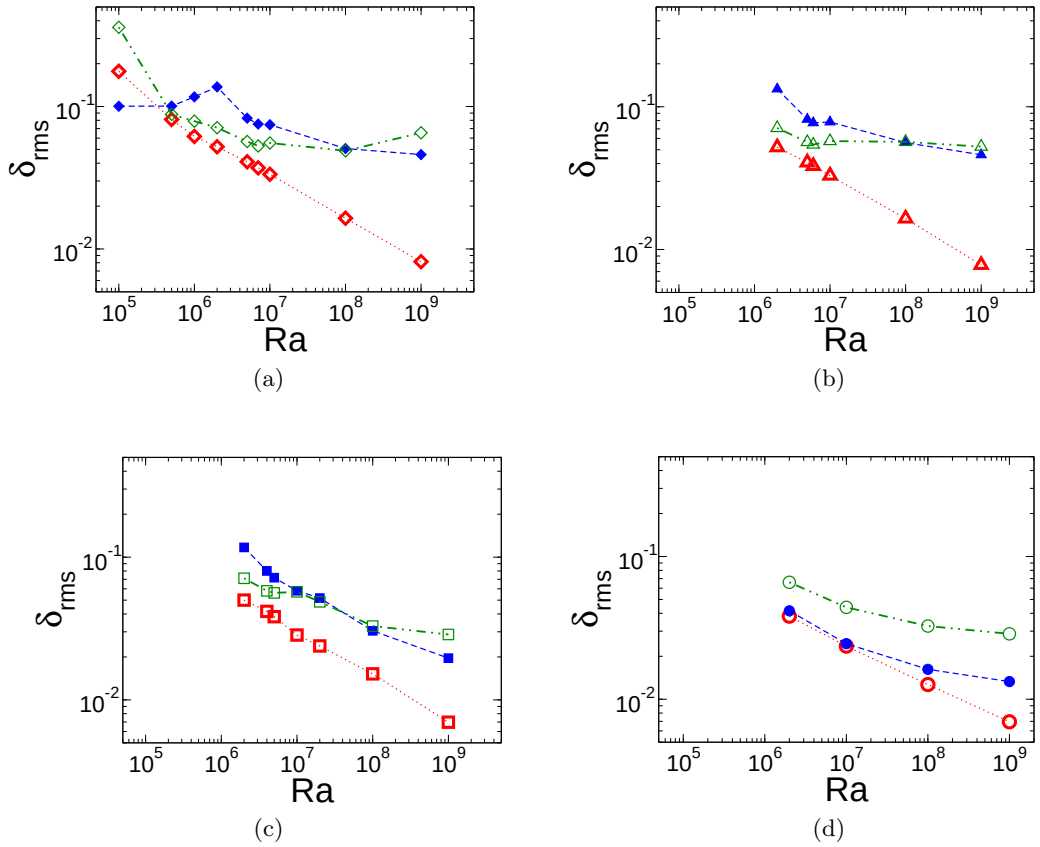

Figure 7.12: Boundary layer thicknesses based on rms profiles. (a) $Pr = 1000$, (b) $Pr = 100$, (c) $Pr = 10$ and (d) $Pr = 1$. Notation as fig. 7.11.

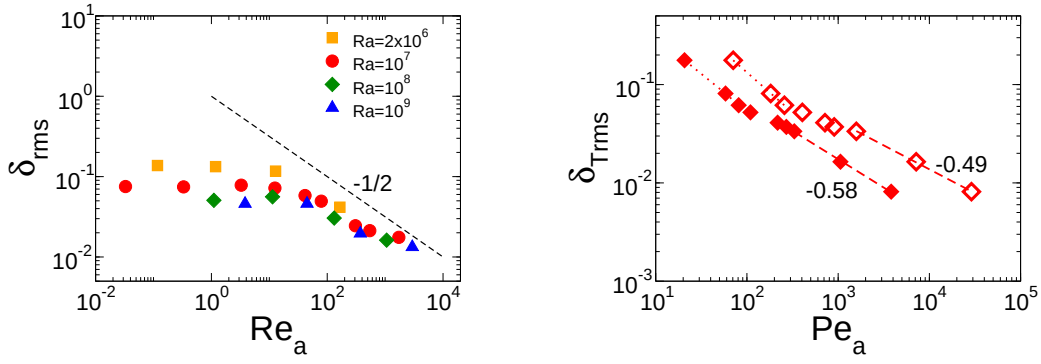

Figure 7.13: (a) Viscous boundary layer thickness with respect to the Reynolds number Re_a, which is calculated using the maximum values of the horizontal velocity rms profiles. (b) Thermal boundary layer thickness with respect to Peclet number Pe_a at $Pr = 10^3$. Filled symbols: Pe_a calculated using the maximum values of the horizontal velocity rms profiles; open symbols: Pe_a calculated using the time-average peak-vertical velocity.

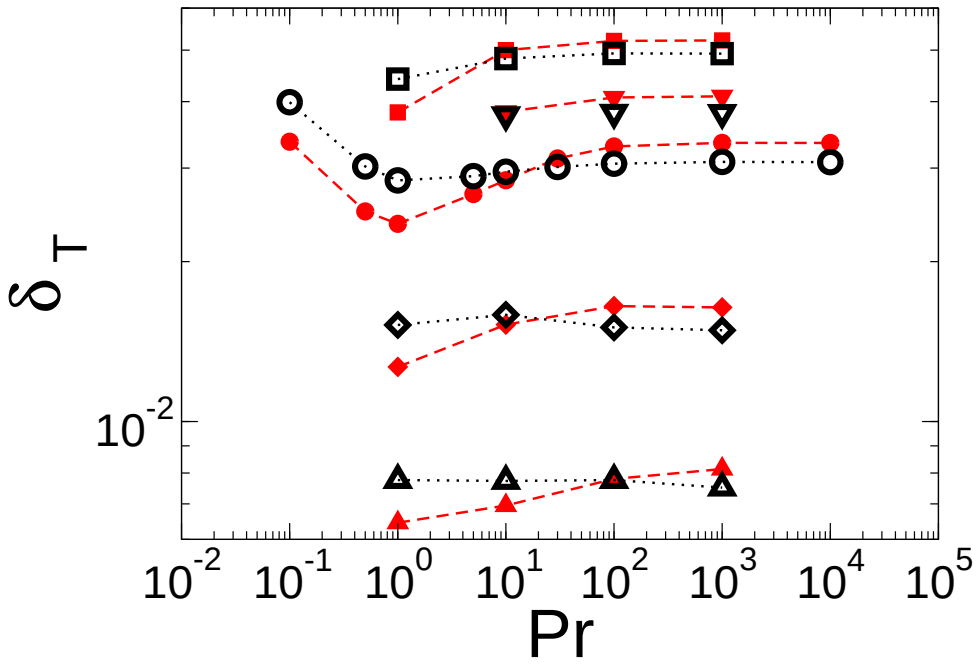

Figure 7.14: Comparison between thermal boundary layer thickness calculated using the temperature rms profile peaks (red filled symbols) and that calculated using the tangent to the temperature profile (black open symbols). Squares: $Ra = 2 \cdot 10^6$; inverted triangles: $Ra = 5 \cdot 10^6$; circles: $Ra = 10^7$; diamonds: $Ra = 10^8$; upright triangles: $Ra = 10^9$.

Chapter 8

Conclusions

In this study we have investigated the main features of the thermal convection at high Pr and moderate Ra. By direct numerical simulations of the Boussinesq equations in a cylindrical domain of aspect ratio 1/2, we have replicated the set-up of several experimental and numerical work. In particular, by simulating the convective flow at quite high Pr ($Pr \sim O(10^3)$), we have explored a $Ra - Pr$ range until now approachable only through laboratory experiments or simplified numerical models.

The high-Pr flows are generally characterized by high Peclet numbers and low Reynolds numbers. This implies that the temperature field is mainly governed by advective dynamics, and the velocity field mainly by diffusive phenomena. The combination of these opposite features generates the convection dynamics at high-Pr.

Since the beginning of this work, we found that the combination of these different dynamics is reflected in the typical large-scale velocities and in the corresponding typical times. The free-fall velocity $U = \sqrt{g\alpha\Delta T h}$, arising from the balance between the inertial term and the buoyancy term of the momentum equation, was inadequate for representing the typical velocities at high Pr, which are much smaller. On the other hand, the usual alternative velocities, characteristic of the diffusive dynamics, obtained by balancing the buoyancy and viscous term of the momentum equation, or by comparing the advective and diffusive terms of the temperature equation, were inadequate as well (this time because of their dependence on Ra). By scaling the results from several simulations we found that the suitable characteristic velocity of the large-scale convective dynamics is $V = U/\sqrt{Pr}$ (note that V and U coincide for $Pr \sim O(1)$). This velocity represents a synthesis between the diffusive characteristic velocities and the free-fall velocity, maintaining the dependence of diffusive

velocities on Pr, and the dependence of the free-fall velocity on Ra.

Using this new characteristic velocity, we derived the suitable non-dimensional form of the Boussinesq equations for high-Pr flows, and a rough estimate of the Re and Pe as functions of Ra and Pr, obtaining $Re = \sqrt{Ra}/Pr$, and, consequently, $Pe = \sqrt{Ra}$ independent of Pr. From the comparison of these estimates with the actual Re and Pe trends, it was clear that they represent only a first order approximation of the Re and Pe behavior, since a single scaling was not sufficient to match all the data in the range of Ra and Pr simulated. Moreover, a power-law relation did not appear to be always appropriate to fit exactly the data, which seem to require logarithmic corrections to the main power-law trend. Further uncertainties derive from the velocity that one defines as typical of the large-scale dynamics. Nevertheless, the Re and Pe estimates (mentioned above) are able to capture the main trends, especially with respect to Pr, when Pr is sufficiently high and a saturation regime is approaching.

The saturation regime is a main feature of the confined flows with increasing Pr. It is due to the fact that the viscous boundary layer, induced by the large-scale recirculations, cannot indefinitely grow as Re decreases (Pr increases), at least because the cell has a finite size. We found that, in a cell of aspect ratio 1/2, the saturation of the viscous boundary layer thickness starts approximatively at $Re_s \simeq 40$ (with Re calculated using the time-averaged peak vertical velocity). The saturation of the viscous boundary layer induces a saturation in the thermal boundary layer thickness (which is apparently dragged by the viscous boundary layer when the latter is thicker than the former). The Peclet number independence of Pr reflects the saturation of the thermal boundary layer. Consequently $Re \sim 1/Pr$, which implies a fast saturation of the viscous boundary layer with increasing Pr.

The thermal boundary layer is strongly related to the Nusselt number, since the latter is determined by the temperature drop which occurs close to the horizontal plates. Our simulation data show Nu independent of Pr, for $Pr \gtrsim 1$. This result, even characterizing the highest Ra simulated ($Ra = 10^9$), can be justified by saturation arguments only when the saturation occurs - that is, for Pr sufficiently high ($Pr \gtrsim 100$). At lower Pr, the independence of Nu on Pr is due to the balancing of two opposite effects that we assume to be acting on the thermal boundary: the Peclet number influence, which tends to drag it down, since Pe slightly increases with increasing Pr before the saturation is reached (we suppose the thermal boundary layer thickness inversely related to Pe); and the viscous boundary layer influence, which tends to drag it up, since the viscous boundary layer grows with increasing Pr, and, at a given Pr, becomes thicker than the thermal boundary layer.

By using previous results at lower Pr and comparing them to our data, we confirm the presence of a lower Pr regime, where approximately $Re \sim Pr^{-0.7}$, and a saturation regime at high-Pr, where $Re \sim Pr^{-1}$. The beginning of the saturation regime depends on a critical Reynolds number (Re_s), beyond which the viscous boundary layer, or, inversely, the large-scale circulation, saturates to a constant size (roughly 2/10 of the cell depth occupied by the boundary layers and 8/10 by large-scale circulations, when the viscous boundary layer thickness is based on the rms profile of the horizontal velocity). However, the approach to saturation seems to be smooth, and the saturation regime seems to affect (or to be affected by) the previous Pr-interval, until the hierarchy between thermal and viscous boundary layers changes.

The presence of the viscous boundary layer, however, does not seem to be a necessary condition for the observation of a saturation regime. Indeed, a qualitatively similar $Re - Pr$ scaling was obtained also in simulations carried out under free-slip boundary condition [12]. In this case it is possible to hypothesize a saturation of the large-scale circulations instead of the viscous boundary layer, but the other arguments on the interaction between viscous and thermal boundary layers seem to be no longer valid. However, even without viscous boundary layers, the large-scale motion generates strong velocity gradients close to the walls, which can substitute the viscous boundary layer arguments in the explanation of the thermal boundary layer behavior at high-Pr regimes.

In spite of its unclear role, the viscous boundary layer is the base of many models for scaling predictions of thermal convection. The usual assumption is to consider the Prandtl-Blasius theory [32], which regards the temperature field as a passive scalar and implies similarity solutions. In the $Ra - Pr$ range considered here, inside the boundary layers we did not find similarities with respect to Ra and Pr neither in velocity profiles nor in temperature profiles.

In the $Ra - Pr$ interval simulated we found different transitional phases (steady, periodic and chaotic solutions), and the wide variety of large-scale structures characterizing the flow. We have performed a qualitative analysis of these solutions, sketching a general picture of the transitional phases in a wide range of Prandtl numbers. We also derived a rough estimate of threshold for the onset of unsteady motion. We analyzed the flow structures through the transitional phases by direct visualizations of the temperature and velocity fields. We found multiple solutions as a long-term phenomenon at $Ra = 10^8$ and $Pr = 10^3$. In particular, we found one of these solutions (four-cell structure) to be stable for a long time interval, even if it shows a break in the mid-plane symmetry of the temperature profile. The strength of

this phenomenon on the temperature profile is comparable to some non-Boussinesq effects. However, the presence of multiple solutions does not affect the Nusselt number significantly.

As a consequence of the several structures found at increasing Ra, the data trends with respect to Ra are generally less clear. However, for the unsteady simulations, we found consistence in the $Nu - Ra$ scaling with the previous experimental results of Niemela and Sreenivasan ([52], [50]), and numerical results of Verzicco and Camussi [78].

We also described the behavior of the flow structures for increasing Pr. The flow passes from large recirculations which are strongly unsteady, interacting with seemingly random plumes, and forming on average axisymmetric and opposite toroidal structures, at $Pr = 1$; to a quite stationary large-scale circulation, mostly extended in the vertical direction, with plumes emitted from almost stationary sheet-structures, forming close to the top and bottom plates as extensions of the thermal boundary layers, at $Pr = 10^3$. It was worth noting that the smooth flow at higher Pr has the same effectiveness in the heat transport (the same Nu) as the turbulent flow at lower Pr, indicating that the turbulent motion, in contrast to common expectations, is not necessarily the most efficient way to transport heat.

Appendix A

Numerical instabilities

The von Neuman stability analysis of the first version of time scheme (2.18) shows that a necessary condition to obtain stable solutions is [3]

$$CFL = \Delta t \left(\frac{|u_z|}{\Delta z} + \frac{|u_r|}{\Delta r} + \frac{|u_\theta|}{r\Delta\theta} \right) \leq \sqrt{3}, \tag{A.1}$$

where CFL is referred as the Courant-Friedrichs-Lewy condition. It arises from the explicit nonlinear terms of the equations. Later on, the nonlinear terms in the azimuthal direction have been computed implicitly ([76]) because the θ term inside (A.1) is excessively constraining due to its dependence on the radius. Indeed, near $r = 0$ this term grows very quickly ([3]). For this reason the present version of the code has a CFL condition not including the azimuthal term (see eq. (2.33)).

In order to maximize the size of time step, it is usually set dynamically with the CFL condition:

$$\Delta t = K \frac{\sqrt{3}}{\left(\frac{|u_z|}{\Delta z} + \frac{|u_r|}{\Delta r} \right)}, \tag{A.2}$$

where K is a safety coefficient slightly smaller than one. However for simplicity in the following discussion $K = 1$ is assured.

Unfortunately, the simulations characterized by low Reynolds numbers and performed using the criterion (A.2) become unstable. The causes of these numerical instabilities can be many. The CFL condition (A.1) was derived for the simplest canonical case with Cartesian coordinates, non-slip condition everywhere on the boundary and without any coupling with the energy equation. The code in the present case is more complex. In particular, the equations in cylindrical coordinates introduce spurious terms which increase the complexity

of both viscous and advective terms of the equations (see eqs. (2.6) and (2.7)). These spurious terms, affecting also the boundary conditions, make the matrices resulting from the discretization of the equations different from the standard used in stability studies. Moreover, the advective azimuthal terms, in contrast to the advective terms in the other directions, are treated implicitly, leading to the elimination of the azimuthal term in the condition (A.1), but also altering the elements of the discretization matrices. Besides, the implicit part of the scheme needs at every step the indirect inversion of a matrix preliminarily factorized to improve the computational efficiency (see eqs. (2.12) and (2.13)) and this is another non-standard implementation. The most probable source of instabilities can be however the spurious viscous terms that are accounted together with the explicit advective terms, instead of being implicitly treated. Another one can be the very high stiffness of the problem because of the combination of low Reynolds number with very small grid size close to the central axis of the cell. The last case is supported by examples found in literature of numerical instabilities arising from implicit schemes when the problem is very stiff ([30], [29]).

Given the difficulty to approach analytically a stability analysis of such a complex code, an empirical way has been preferred, analyzing the numerical instabilities directly by the simulations results.

With this purpose, a sample of six simulations has been considered. They are characterized by different grids, with Ra which varies from 10^5 to 10^8 and Pr equal to 100 or 1000. Four of them have a steady state solution, while two of them have unsteady solution. As shown in table A.1, they are tagged by a number from one to six and by a letter s (steady) or u (unsteady). These tags will identify them in the other tables.

Table A.1 shows also the actual maximum size of time step Δt_a to obtain stable solutions and the size of time step Δt_h which is obtained from (A.2) for those simulations. The time step Δt_a is calculated directly performing simulations. Note that the size of time step evaluated from (A.2) is a function of velocity fields and then it is generally not a constant. However, for simulations having steady solutions it is constant in any case. Instead, for the two simulations which have unsteady solutions the corresponding variable quantities are reported in tables considering the typical values.

Table A.2 shows for the same simulations the single terms of the CFL condition (A.1) calculated using the actual maximum allowed size of time step Δt_a :

$$clf_1 = \Delta t_a \left[\frac{|u_\theta|}{r\Delta\theta}\right]_{max} , \quad cfl_2 = \Delta t_a \left[\frac{|u_r|}{\Delta r}\right]_{max} , \quad clf_3 = \Delta t_a \left[\frac{|u_z|}{\Delta z}\right]_{max} \tag{A.3}$$

Tag	Ra	Pr	n_θ	n_r	n_z	Δt_a	Δt_h	Δt_e
$1s$	$1 \cdot 10^5$	10^3	161	26	101	$2.9 \cdot 10^{-3}$	$2.4 \cdot 10^{0}$	$1.9 \cdot 10^{-7}$
$2s$	$2 \cdot 10^6$	10^3	101	25	101	$1.4 \cdot 10^{-2}$	$1.6 \cdot 10^{0}$	$2.4 \cdot 10^{-6}$
$3s$	$2 \cdot 10^6$	10^3	121	45	201	$4.3 \cdot 10^{-3}$	$9.0 \cdot 10^{-1}$	$5.0 \cdot 10^{-7}$
$4u$	$1 \cdot 10^7$	10^3	217	55	217	$6.3 \cdot 10^{-3}$	$3.8 \cdot 10^{-1}$	$2.3 \cdot 10^{-7}$
$5s$	$2 \cdot 10^6$	10^2	101	25	101	$4.4 \cdot 10^{-2}$	$5.6 \cdot 10^{-1}$	$7.6 \cdot 10^{-6}$
$6u$	$1 \cdot 10^8$	10^3	217	75	301	$1.0 \cdot 10^{-2}$	$1.9 \cdot 10^{-1}$	$3.8 \cdot 10^{-7}$

Table A.1: This table shows the actual maximum size of time size Δt_a to obtain stable solutions, the hypothetical maximum size of time step Δt_h which should be from (A.2) and the maximum size of time step Δt_e which comes out from (A.5) for some typical simulations performed by the numerical code described in the previous section.

Tag	cfl_1	cfl_2	cfl_3	cfl_{es}
$1s$	$5.25 \cdot 10^{-2}$	$1.07 \cdot 10^{-3}$	$2.03 \cdot 10^{-3}$	$2.10 \cdot 10^{-3}$
$2s$	$1.57 \cdot 10^{-1}$	$5.69 \cdot 10^{-3}$	$1.08 \cdot 10^{-2}$	$1.56 \cdot 10^{-2}$
$3s$	$1.06 \cdot 10^{-1}$	$3.74 \cdot 10^{-3}$	$8.01 \cdot 10^{-3}$	$8.32 \cdot 10^{-3}$
$4u$	$4.96 \cdot 10^{-1}$	$8.68 \cdot 10^{-3}$	$2.69 \cdot 10^{-2}$	$2.85 \cdot 10^{-2}$
$5s$	$1.73 \cdot 10^{0}$	$7.09 \cdot 10^{-2}$	$1.15 \cdot 10^{-1}$	$1.37 \cdot 10^{-1}$
$6s$	$1.08 \cdot 10^{0}$	$2.16 \cdot 10^{-2}$	$8.18 \cdot 10^{-2}$	$9.27 \cdot 10^{-2}$

Table A.2: This table shows the values of the single terms of the CFL condition defined by (A.3) and the actual CFL condition defined by (A.4). Tag numbers identify the same simulations of table A.1.

and the CFL condition based on Δt_a and referred only to the explicit terms of the time scheme:

$$cfl_{es} = \Delta t_a \left[\frac{|u_r|}{\Delta r} + \frac{|u_z|}{\Delta z} \right]_{max} \tag{A.4}$$

From table A.2 it is evident that only if cfl_{es} is much smaller than the theoretical value of $\sqrt{3} \simeq 1.73$, is it possible to have stable simulations. Moreover, the values of cfl_{es} are very different for different simulations, that is cfl_{es} is far from being constant. This means that in our simulations the CFL condition is only a necessary condition, not suitable as a stability limit to evaluate the maximum time step size. Evidently it is not the most convincing stability criterion in the flow regimes that we are considering. Thus, a deeper analysis has to be carried out to find a more suitable stability limit, if it exists.

Tag	vl_1	vl_2	vl_3	sl_t
$1s$	$2.57 \cdot 10^{4}$	$1.57 \cdot 10^{1}$	$1.19 \cdot 10^{1}$	$2.57 \cdot 10^{4}$
$2s$	$9.99 \cdot 10^{3}$	$1.56 \cdot 10^{1}$	$3.99 \cdot 10^{1}$	$1.00 \cdot 10^{4}$
$3s$	$1.48 \cdot 10^{4}$	$1.63 \cdot 10^{1}$	$1.67 \cdot 10^{1}$	$1.49 \cdot 10^{4}$
$4u$	$4.75 \cdot 10^{4}$	$1.61 \cdot 10^{1}$	$1.28 \cdot 10^{1}$	$4.75 \cdot 10^{4}$
$5s$	$9.93 \cdot 10^{3}$	$1.55 \cdot 10^{1}$	$3.97 \cdot 10^{1}$	$9.98 \cdot 10^{3}$
$6u$	$4.48 \cdot 10^{4}$	$1.52 \cdot 10^{1}$	$1.93 \cdot 10^{1}$	$4.48 \cdot 10^{4}$

Table A.3: This table shows the values of the viscous single terms of the SL condition defined by (A.6) and the actual SL condition defined by (A.7) for explicit time scheme. Tag numbers identify the same simulations of table A.1 and A.2.

The implicit part of the time scheme, which mainly consists of viscous terms, should be unconditionally stable. However, the Crank-Nicolson scheme, although stable, can produce oscillatory solutions when the Reynolds number is small ([30], [29]) because the problem becomes very stiff.

If all terms are treated explicitly, then the stability limit SL in non-dimensional form becomes [3]:

$$SL = \Delta t \left[\frac{|u_z|}{\Delta z} + \frac{|u_r|}{\Delta r} + \frac{|u_\theta|}{r\Delta\theta} + \frac{4}{Re\Delta z^2} + \frac{4}{Re\Delta r^2} + \frac{4}{Re(r\Delta\theta)^2} \right] \leq \sqrt{3}. \tag{A.5}$$

Using the criterion (A.5), the size of time step, called Δt_e, results much smaller than the actual maximum size of time step Δt_a. Thus, comparing the actual maximum time step to those which came from the stability criteria (A.2) and (A.5) (see table A.1), it is evident that both of these criteria are not suitable in our case. (A.2) is not enough constraining, (A.5) is too constraining.

The very small values of Δt_e are mainly due to the last viscous term which appears in (A.5) and this because of the smallness of the grid size in θ direction close to the axis. Indeed, considering $\Delta r \sim \Delta z$ and $r\Delta\theta \sim \Delta z$ close to the sidewall, then around the axis $r = 0$ it results $r\Delta\theta \sim 10\Delta z^2$. This means that the last term in (A.5) is several orders of magnitude larger than the other terms. This estimation is confirmed from data of tables A.2 and A.3. Indeed, table A.3 shows the single viscous terms of (A.5) evaluated using the actual maximum time step Δt_a:

$$vl_1 = \frac{\Delta t_a}{Re} \left[\frac{4}{(r\Delta\theta)^2} \right]_{max}, \quad vl_2 = \frac{\Delta t_a}{Re} \left[\frac{4}{(\Delta r)^2} \right]_{max}, \quad vl_3 = \frac{\Delta t_a}{Re} \left[\frac{4}{(\Delta z)^2} \right]_{max} \tag{A.6}$$

and the total stability limit (A.5) based on Δt_a:

$$sl_t = \Delta t_a \left[\frac{|u_z|}{\Delta z} + \frac{|u_r|}{\Delta r} + \frac{|u_\theta|}{r\Delta\theta} + \frac{4}{Re\Delta z^2} + \frac{4}{Re\Delta r^2} + \frac{4}{Re(r\Delta\theta)^2} \right]_{max}. \tag{A.7}$$

Tables A.2 and A.3 show the values of all the single terms of the stability limit (A.5). Comparing all these values, one obtains, in the simulations considered, that the CFL terms are smaller than the viscous terms, and the viscous term for θ direction (vl_1) is the largest one. It is the main constrain to the size of time step in the explicit time scheme, given that all the other terms are negligible with respect to it. Because of this, it was reasonable to expect that this term is the one creating problems in the semi-implicit time scheme that we are considering.

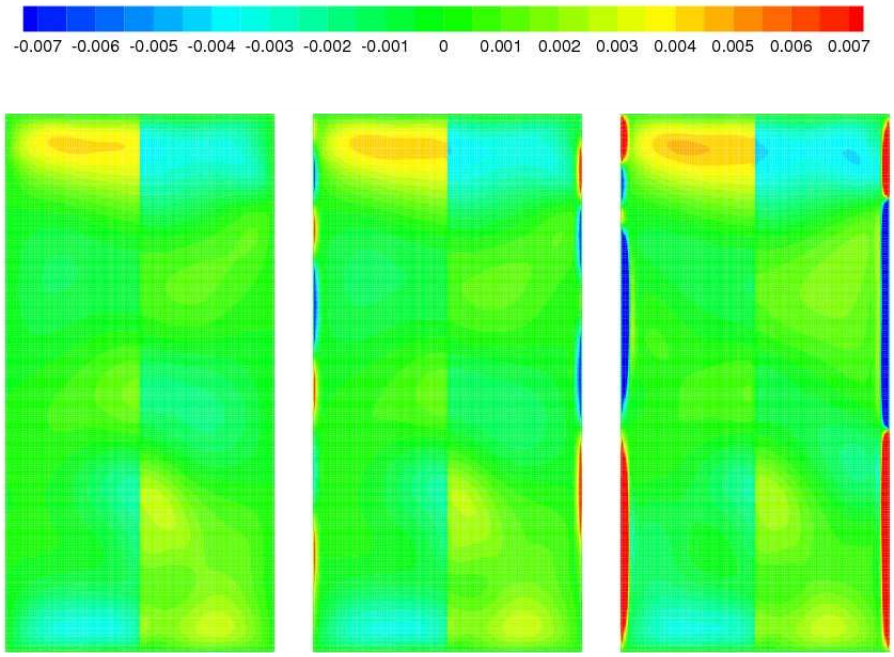

Figure A.1: This figure shows subsequent snapshots of the azimuthal velocity field of the simulation tagged $6u$ in table A.1. This simulation has been performed by the code described in the previous section with an unstable size of time step equal to $\Delta t = 0.011$.

Unfortunately, analyzing the values of vl_1 in table A.3, nothing seems to confirm this hypothesis. Indeed the values of vl_1 are different for different simulations and they do not seem to follow any common criterion.

On the contrary, the value of vl_2, which is the viscous stability term in radial direction (see (A.6)), is quite the same for all the simulations shown in table A.3. Considering the approximation errors which characterize this kind of study, it is certainly possible to consider vl_2 as a constant. This unexpected result could lead to the stability criterion that we are looking for and then it has to be better understood.

The next step is to analyze the flow fields, to understand where exactly the instabilities appear. In figure A.1 subsequent snapshots of the simulation tagged $6u$ in table A.1 are shown. This simulation has been performed with a size of time step slightly bigger than the stable one ($\Delta t = 0.011$ instead of $\Delta t = 0.010$). The snapshots represent the azimuthal velocity field in a vertical section of the cell. They are spaced of one non-dimensional time unit and from them it is possible to see that the instabilities appear close to the sidewall and grow very fast in time.

The fact that the numerical instabilities appear close to the sidewall confirms that they

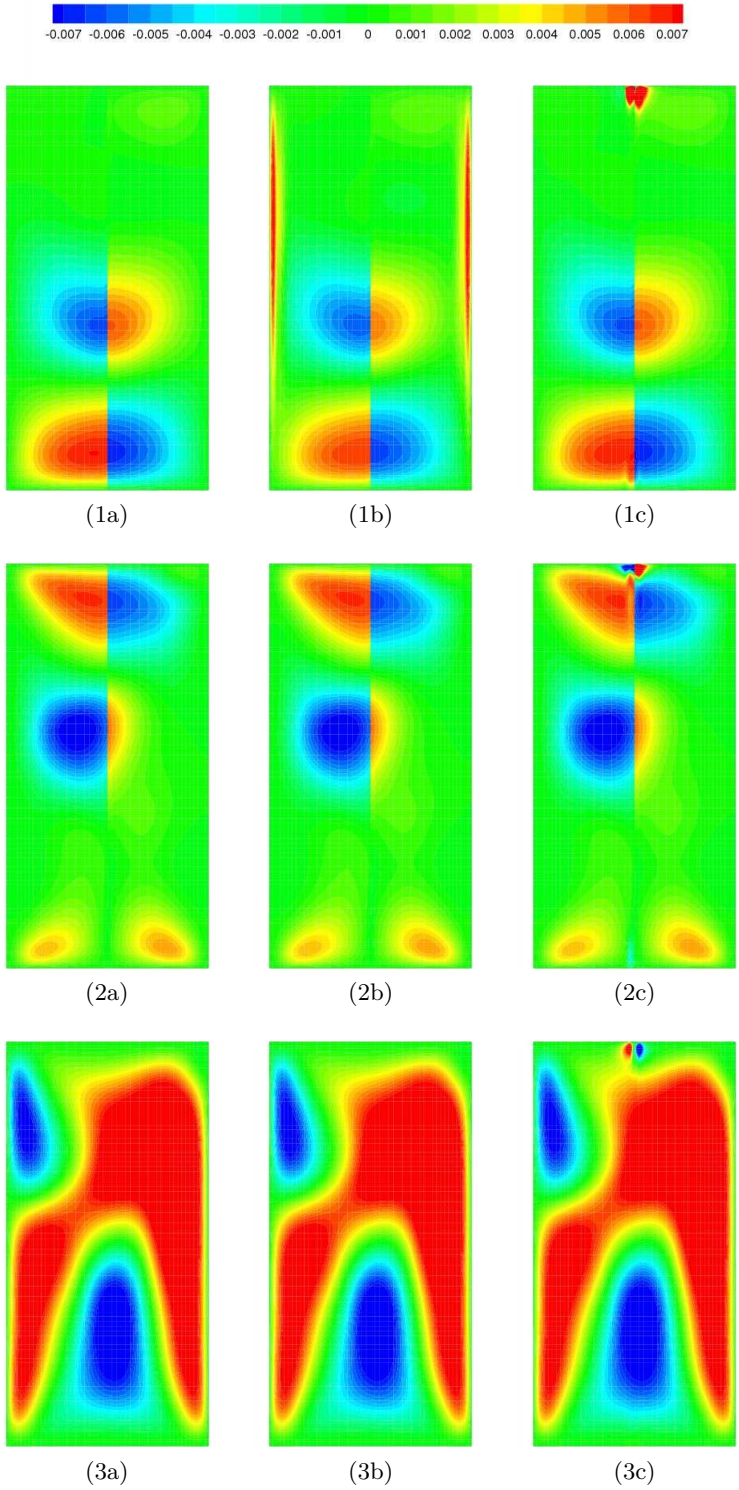

Figure A.2: This figure shows snapshots of the simulation tagged $5s$ in table A.1. Row 1 represents the azimuthal velocity, row 2 the radial velocity and row 3 the vertical velocity. Column a represents the stable steady state solution. Column b represents the unstable solution obtained from the semi-implicit time scheme of the previous section with $\Delta t = 0.045$. Column c represents the unstable solution obtained from the totally explicit corresponding time scheme with $\Delta t = 0.00001$

Tag	Ra	Pr	n_θ	n_r	n_z	Re	Δt_a	cfl_{es}	vl_2
$5s$	$2 \cdot 10^6$	10^2	101	25	101	141	$4.4 \cdot 10^{-2}$	$7.09 \cdot 10^{-2}$	$1.55 \cdot 10^1$
$5sx$	$2 \cdot 10^6$	10^2	121	25	121	141	$4.4 \cdot 10^{-2}$	$6.08 \cdot 10^{-2}$	$1.55 \cdot 10^1$
$5sy$	$2 \cdot 10^6$	10^2	101	35	101	141	$2.2 \cdot 10^{-2}$	$3.78 \cdot 10^{-2}$	$1.57 \cdot 10^1$

Table A.4: This table shows some more significant stability values of the simulation tagged $5s$ in table A.1 with those of two new simulations performed changing only the grid point number. The code from the previous section was used.

could be due to the viscous stability term in radial direction, even if the viscous stability term in azimuthal direction is much larger. Figure A.2 shows snapshots of the simulation tagged $5s$ in table A.1. This simulation has been performed both with the original semi-implicit time scheme and with the totally explicit version of the same scheme, with a size of time step larger than the correspondent stable one. Then, in figure A.2, the three components of the velocity field are compared in the case of stable solution, in the case of unstable solution obtained by the semi-implicit scheme and in the case of unstable solution obtained by the explicit scheme. From this example we can see that the numerical instabilities again appear close to the sidewall for the original scheme, while they appear near the axis in the case of explicit scheme, as expected. It can be noted that the instabilities start in the azimuthal velocity field in the case of the semi-implicit scheme. This behavior is common to all the simulations of table A.1.

To be sure that the numerical instabilities depend only on the radial grid size, a further check has been done. Starting from the simulation tagged $5s$ in table A.1, two new simulations have been performed changing only the grid point number. In one case the grid point number was increased only in the vertical and azimuthal direction, while in the other case it was increased only in the radial direction. Table A.4 shows the results. As expected, the allowed maximum size of time step to avoid instabilities is unchanged with respect to the reference simulation $5s$ in the first case ($5sx$) and is smaller in the second case ($5sx$). Note also that vl_2 has values similar to those of the other simulations of table A.3.

At this point, safely keeping the value of vl_2 equal to 15, it is possible to derive a suitable criterion to determine the maximum size of time step which allows to avoid instabilities, which is:

$$\Delta t \leq \frac{15}{4} Re \left[(\Delta r)^2 \right]_{min} \tag{A.8}$$

Note that this stability condition predicts a fixed size of time step instead of a varying size of time step as the CFL limit (A.2). Analyzing the results of further simulations, it has been found that the empirical stability limit (A.8) is valid until the CFL limit (A.2) does not prevail, without interacting to each other. Then, to evaluate the maximum allowed size

of time step, the more constraining condition between (A.2) and (A.8) has to be considered.

The stability criterion (A.8) is derived only from data evidence, without any theoretical consideration. As a consequence, it is difficult to understand the causes at the base of this kind of instability. The stability limit (A.8) involves viscous dynamics and the viscous terms of the equations are mainly included in the implicit part of the time scheme, which theoretically should be unconditionally stable.

In the code that we are considering, the implicit part of the time scheme is implemented by the Crank-Nicolson method (see section 2.3). A well known drawback with Crank-Nicolson is that the error propagation could be weakly damped ([54]). Indeed, when the eigenvalues of L in the time scheme (2.18) are large in magnitude, their eigenvectors are damped by a ratio approaching -1 at each full step. Then, a way to reduce the instability issues could be to change the Crank-Nicolson scheme with a more suitable implicit scheme by changing the coefficients α_l and β_l inside (2.18). For example, the coefficients (A.9) and (A.10), suggested in [69], lead to a new implicit time scheme in which their eigenvectors are damped by a ratio approaching $87/185 \simeq 0.47$ at each full step.

$$\alpha_1 = \frac{29}{96}, \qquad \alpha_2 = -\frac{3}{40}, \qquad \alpha_3 = \frac{1}{6}, \tag{A.9}$$

$$\beta_1 = \frac{37}{160}, \qquad \beta_2 = \frac{5}{24}, \qquad \beta_3 = \frac{1}{6}, \tag{A.10}$$

In fact, using coefficients (A.9) and (A.10) instead of coefficients (2.32), better results in term of maximum size of time step have been found.

The success of this strategy devises for the implicit part of the time scheme seems in contradiction with the hypothesis of numerical instabilities due to the viscous spurious terms treated explicitly instead of implicitly. However, the coefficients of the implicit and explicit parts of the time scheme are linked each other and this could allow an extension of the stability benefit to the whole code.

The change of the implicit part coefficients of the time scheme does not lead to any fundamental variation in the code results. Indeed, several steady state simulations have been carried out using both schemes and their solutions differ for an error in the order of machine precision. Moreover, the stability analysis previously performed is still qualitatively valid for the new time scheme. The quantitative differences are shown in table A.5.

Comparing table A.5 with A.3 shows that the values of the actual size of time step allowed from the new time scheme coefficients are higher with respect to the old coefficients. Moreover, the viscous stability term vl_2 is still constant, even if its value is larger, as ex-

Tag	Δt_a	cfl_{es}	vl_2
$1s$	$4.0 \cdot 10^{-3}$	$2.89 \cdot 10^{-3}$	$2.17 \cdot 10^{1}$
$2s$	$1.9 \cdot 10^{-2}$	$2.12 \cdot 10^{-2}$	$2.12 \cdot 10^{1}$
$3s$	$6.0 \cdot 10^{-3}$	$1.16 \cdot 10^{-2}$	$2.27 \cdot 10^{1}$
$4u$	$8.9 \cdot 10^{-3}$	$4.02 \cdot 10^{-2}$	$2.27 \cdot 10^{1}$
$5s$	$6.1 \cdot 10^{-2}$	$1.90 \cdot 10^{-1}$	$2.15 \cdot 10^{1}$
$6u$	$1.4 \cdot 10^{-2}$	$1.30 \cdot 10^{-1}$	$2.13 \cdot 10^{1}$

Table A.5: This table shows some more significant stability values of the same simulations in table A.1. The simulations, in this case, were performed with the new coefficients (A.9) and (A.10) of the time scheme.

pected. Then, considering safely the value of vl_2 equal to 21, the stability limit of the new time scheme results to be:

$$\Delta t \leq \frac{21}{4} Re \left[(\Delta r)^2 \right]_{min} \tag{A.11}$$

Also in this case, the size of time step for stability is the minimum among those coming from conditions (A.11) and (A.2). Comparing the conditions (A.11) and (A.8), for all the simulations in which the more constraining stability limit is the viscous one, the maximum allowed size of time step is $\frac{7}{5}$ larger if we use the new time scheme instead of the original time scheme. Then, implementing the new coefficients (A.9) and (A.10), the performance of the code resulted up to 40% faster.

As a conclusion, a stability criterion and an improvement of the code performances have been obtained, and in all the simulations performed in the present work these results have been applied. In particular a code implemented with the new coefficients (A.9) and (A.10) has been adopted in place of the old version and the stability criterion (A.11) has been used when is found more constraining than the CFL criterion.

Bibliography

[1] G. Ahlers, S. Grossmann, and D. Lohse. Large-scale dynamics in turbulent Rayleigh-Bénard convection. *Rev. Mod. Phys. (in press)*, 81, 2009.

[2] G. Ahlers and X. Xu. Prandtl-number dependence of heat transport in turbulent Rayleigh-Bénard convection. *Phys. Rev. Lett.*, 86:3320–3323, 2001.

[3] K. Akselvoll and P. Moin. An efficient method for temporal integration of the Navier-Stokes equations in confined axisymmetric geometries. *J. Comput. Phys.*, 125:454–463, 1996.

[4] G. Amati, K. Koal, F. Massaioli, K. R. Sreenivasan, and R. Verzicco. Turbulent thermal convection at high Rayleigh numbers for a Boussinesq fluid of constant Prandtl number. *Phys. Fluids*, 17, 2005.

[5] S. Ashkenazi and V. Steinberg. High Rayleigh number turbulent convection in a gas near the gas-liquid critical point. *Phys. Rev. Lett.*, 83:3641–3644, 1999.

[6] G. K. Batchelor. Small scale variation of convected quantities like temperature in turbulent fluid. *J. Fluid Mech.*, 5:113–133, 1959.

[7] A. Belmonte, A. Tilgner, and A. Libchaber. Boundary layer length scales in thermal turbulence. *Phys. Rev. Lett.*, 70:4067, 1993.

[8] H. Bénard. Les tourbillons cellulaires dans une nappe liquide. *Revue Gen. Sci. Pures Appl.*, 11:1261–1271, 1900.

[9] E. Bodenschatz, W. Pesch, and G. Ahlers. Recent developments in Rayleigh-Bénard convection. *Annu. Rev. Fluid Mech.*, 32:709–778, 2000.

[10] R. Bolgiano. Structure of turbulence in a stably stratified media. *J. Geoph. Res.*, 64:2226–2229, 1959.

[11] K. Boronska and L. S. Tuckerman. Standing and travelling waves in cylindrical Rayleigh-Bénard convection. *J. Fluid Mech.*, 559:279–298, 2006.

[12] M. Breuer, S. Wessling, J. Schmalzl, and U. Hansen. Effect of inertia in Rayleigh-Bénard convection. *Phys. Rev. E*, 69:026302, 2004.

[13] E. Brown and G. Ahlers. Temperature gradients, and research for non-boussinesq effects, in the interior of turbulent Rayleigh-Bénard convection. *EPL*, 80:14001, 2007.

[14] E. Brown, D. Funfschilling, and G. Ahlers. Anomalous Reynolds-number scaling in turbulent Rayleigh-Bénard convection. *J. Stat. Mech.*, 2007.

[15] Busse. *Fundamental of thermal convection. In Mantle Convection: Plate Tectonics and Global Dynamics*. Gordon and Breach, 1989.

[16] F. H. Busse. Non-linear properties of thermal convection. *Rep. Prog. Phys.*, 41:1929–1967, 1978.

[17] E. Calzavarini, D. Lohse, F. Toschi, and R. Tripiccione. Rayleigh and Prandtl number scaling in the bulk of Rayleigh-Bénard turbulence. *Phys. Fluids*, 17:055107, 2005.

[18] B. Castaing, G. Guranatne, F. Heslot, L. Kadanoff, A. Libchaber, and S. Thomae. Scaling of hard thermal turbulence in Rayleigh-Bénard convection. *J. Fluid Mech.*, 204:1–30, 1989.

[19] S. Chandrasekar. *Hydrodynamic and Hydromagnetic Stability*. Oxford Univ. Press, 1961.

[20] G. S. Charlson and R. L. Sani. Thermoconvective instability in a bounded cylindrical fluid layer. *Intl. J. Heat Mass Transfer*, 13:1479–1496, 1970.

[21] F. Chillá, S. Ciliberto, C. Innocenti, and E. Pampaloni. Boundary layer and scaling properties in turbulent convection. *Il Nuovo Cimento*, 15:1229–1249, 1993.

[22] A. J. Chorin. On the convergence of discrete approximations to the Navier-Stokes equations. *Math. Comput.*, 23:341, 1969.

[23] S. Cioni, S. Ciliberto, and J. Someria. Srongly turbulent Rayleigh-Bénard convection in mercury: comparison with results at moderate prandtl number. *J. Fluid Mech.*, 335:111–140, 1997.

[24] R. Clever and F. Busse. Transition to time-dependent convection. *J. Fluid Mech.*, 65:625–645, 1974.

[25] V. Croquette, P. Le Gal, and A. Pocheau. Spatial features of the transition to chaos in an extended system. *Phys. Scripta*, T13:135, 1986.

[26] C. R. Doreing, F. Otto, and M. G. Reznikoff. Bounds on vertical heat transport for infinite-Prandtl-number Rayleigh-Bénard convection. *J. Fluid Mech.*, 560:229–241, 2006.

[27] M. Duponcheel, P. Orlandi, and G. Winckelmans. Time-reversibility of Euler equations as a benchmark for energy conserving schemes. *Journal of Computational Physics*, 227:8736–8752, 2008.

[28] M. S. Emran and J. Schumacher. Fine-scale statistics of temperature and its derivatives in convective turbulence. *J. Fluid Mech.*, 611:13–34, 2008.

[29] J. H. Ferziger and M. Perić. *Computational Methods for Fluid Dynamics*. Springer, 2002.

[30] C. A. J. Fletcher. *Computational Techniques for Fluid Dynamics*. Springer-Verlag, 1988.

[31] A. V. Getling. *Rayleigh-Bénard Convection: Structures and Dynamics*. World Scientific, 1998.

[32] S. Grossmann and D. Lohse. Scaling in thermal convection: a unifying theory. *J. Fluid Mech.*, 407:27–56, 2000.

[33] S. Grossmann and D. Lohse. Thermal convection for large Prandtl numbers. *Phys. Rev. Lett.*, 86:3316–3319, 2001.

[34] U. Hansen, D. A. Yuen, and S. E. Kroening. Transition to hard turbulence in thermal convection at infinire Prandtl number. *Phys. Fluids A*, 2:2157–2163, 1990.

[35] G .R. Hardin and R. L. Sani. Weaky non-linear solutions. *Intl. J. Numer. Meth. Fluids*, 17:755, 1993.

[36] F. Heslot, B. Castaing, and A. Libchaber. Transitions to turbulence in helium gas. *Phys. Rev. A*, 36:5870–5873, 1987.

[37] B. Hof, G. J. Lucas, and T. Mullin. Flow state multiplicity in convection. *Phys. Fluids*, 11:2815–2817, 1999.

[38] L. Kadanoff. Turbulent heat flux: structures and scalig. *Phys. Today*, 54:34–39, 2001.

[39] L. Kellogg and S. King. The effect of temperature dependent viscosity on structure of new plumes in the mantle. *EPSL*, 148:13–26, 1997.

[40] R. Kerr. Rayleigh number scaling in numerical convection. *J. Fluid Mech.*, 310:139–179, 1996.

[41] R. M. Kerr and J. R. Herring. Prandtl number dependence of Nusselt number in direct numerical simulations. *J. Fluid Mech.*, 419:325–344, 2000.

[42] J. Kim and P. Moin. Application of a fractional-step method to incompressible Navier-Stokes equations. *J. Comput. Phys.*, 59:308–323, 1985.

[43] A. N. Kolmogorov. The local structure of turbulence in incompressible viscous fluid for a very large Reynolds numbers. *Proc. R. Soc. Lond. A*, 434:9–13, 1941.

[44] R. H. Kraichnan. Turbulent thermal convection at arbitrary Prandtl number. *Phys. Fluids*, 5(11):1374–1389, 1962.

[45] R. Krishnamurti and L. N. Howard. Large-scale flow generation in turbulent convection. *Proc. Natl. Acad. Sci.*, 78(4):1981–1985, 1981.

[46] S. Lam, X. Shang, S. Zhou, and K. Xia. Prandtl number dependence of the viscous boundary layer and the Reynolds numbers in Rayleigh-Bénard convection. *Phys. Rev. Lett. E*, 65, 2002.

[47] A. Malevsky. Patters of convective turbulence: an effect of prandtl number. *Phys. Earth and Plan. Int.*, 88:31–41, 1995.

[48] M. Manga and D. Weeraratne. Experimental study of non-Boussinesq Rayleigh-Bénard convection at high Rayleigh and Prandtl numbers. *Phys. Fluids*, 11:2969–2976, 1999.

[49] A. S. Monin and A. M. Yaglom. *Statistical Fluid Mechanics: mechanics of turbulence*, volume 2. The MIT press, 1975.

[50] J. J. Niemela, L. Skrbek, K. R. Sreenivasan, and R. J. Donnelly. Turbulent convection at very high Rayleigh numbers. *Nature*, 404:837–840, 2000.

[51] J. J. Niemela, L. Skrbek, K. R. Sreenivasan, and R. J. Donnelly. The wind in confined thermal convection. *J. Fluid Mech.*, 449:169–178, 2001.

[52] J. J. Niemela and K. R. Sreenivasan. Confined turbulent convection. *J. Fluid Mech.*, 481:355–384, 2003.

[53] P. Oresta, G. Stringano, and R. Verzicco. Transitional regimes and rotation effects in Rayleigh-Bénard convection in a slender cylindrical cell. *Eur. J. Mech. B/Fluids*, 2006.

[54] O. Osterby. Five ways of reducing the Crank-Nicolson oscillations. *Bit Num. Math.*, 43:811–822, 2003.

[55] W. R. Peltier. *In Mantle Convection: Plate Tectonics and Global Dynamics.* Gordon and Breach, 1989.

[56] N. A. Phillips. *The Atmosphere and Sea in Motion.* Rockefeller Inst. Press, 1959.

[57] Lord Rayleigh. On convective currents in horizontal layer of fluid when the higher temperature is on the under side. *Philos. Mag.*, 32:529–546, 1916.

[58] M. Reeuwijk, H. J. J. Jonker, and K. Hanjalić. Wind and boundary layers in Rayleigh-Bénard convection. i. analysis and modeling. *Phy. Rew. E*, 77:036311, 2008.

[59] P. E. Roche, B. Castaing, B. Chabaud, and B. Hébral. Prandtl and Rayleigh numbers dependencies in Rayleigh-Bénard convection. *Europhys. Lett.*, 58:693–698, 2002.

[60] S. Rudiger and F. Feudel. Patter formation in Rayleigh-Bénard convection in a cylindrical container. *Phys. Rev. E*, 62:4927–4931, 2000.

[61] A. Sameen, R. Verzicco, and K. R. Sreenivasan. Non-boussinesq convection at moderate rayleigh numbers in low temperature gaseous helium. *Phys. Scr.*, T132:014053, 2007.

[62] A. Sameen, R. Verzicco, and K. R. Sreenivasan. Specific roles of fluid properties in non-Boussinesq thermal convection at the Rayleigh number of $2 \cdot 10^8$. *Europhys. Lett.*, (to appear).

[63] H. Schlichting and K. Gersten. *Boundary-Layer Theory.* Springer, 8 edition, 2000.

[64] A. Schluter, D. Lortz, and F. Busse. On the stability of steady infinite amplitude convection. *J. Fluid Mech.*, 23:129–144, 1965.

[65] J. Schmalzl, M. Breuer, and U. Hansen. The influence of the Prandtl number on the style of vigorous thermal convection. *Goephys. Astrophys. Fluid Dynamics*, 96:381–403, 2002.

[66] J. Schumacher, K. R. Sreenivasan, and P. K. Yeung. Very fine structures in scalar mixing. *J. Fluid Mech.*, 531:113–122, 2005.

[67] B. I. Shraiman and E. D. Siggia. Heat transport in high-Rayleigh number convection. *Phys. Rev. A*, 42:3650–3653, 1990.

[68] E.D. Siggia. High Rayleigh number convection. *Annu. Rev. Fluid Mech.*, 26, 1994.

[69] P. R. Spalart and R. D. Moser. *J. Comput. Phys.*, 96:297, 1991.

[70] K. R. Sreenivasan, A. Bershadskii, and J. J. Niemela. Mean wind and its reversal in thermal convection. *Phys. Rev. E*, 65:056306, 2002.

[71] K. Sugiyama, E. Calzavarini, S. Grossmann, and D. Lohse. Non-Oberbeck-Bussinesq effects in 2d Rayleigh-Bénard convection in glycerol. *Submitted to Phys. Fluids*, –:–, 2007.

[72] H. Tennekes and J. L. Lumley. *A First Course in Turbulence*. The MIT Press, 1972.

[73] D. C. Threlfall. Free convection in low-temperature gaseous helium. *J. Fluid Mech.*, 67:17–28, 1975.

[74] D. J. Tritton. *Physical Fluid Dynamics*. Clarendon Press, 2 edition, 1988.

[75] R. Verzicco. Turbulent thermal convection in a closed domain: viscous boundary layer and mean flow effects. *Eur. Phys. J. B*, 35:133–141, 2003.

[76] R. Verzicco and R. Camussi. Transitional regimes of low-Prandtl thermal convection in a cylindrical cell. *Phys. Fluids*, 9:1287–1295, 1997.

[77] R. Verzicco and R. Camussi. Prandtl number effects in convective turbulence. *J. Fluid Mec.*, 383:55–73, 1999.

[78] R. Verzicco and R. Camussi. Numerical experiments on strongly turbulent thermal convection in a slender cylindrical cell. *J. Fluid Mec.*, 477:19–49, 2003.

[79] R. Verzicco and P. Orlandi. A finite-difference scheme for three-dimensional incompressible flows in cylindrical coordinates. *J. Comput. Phys.*, 123:402–414, 1996.

[80] X. Wang. Bound on vertical heat tranport at large Prandtl number. *Physica D*, 237:854 – 858, 2008.

[81] K. Xia, S. Liam, and S. Zhou. Heat-flux measurement in high-Prantdl-number turbulent Rayleigh-Bénard convection. *Phys. Rev. Lett.*, 88, 2002.

[82] S. Zaleski. *Geophysical and astrophysical convection.* Gordon and Breach Sience, 1998.